

Feature Article

An Overview of the Aerosol Deposition Method: Process Fundamentals and New Trends in Materials Applications

D. Hanft¹, J. Exner¹, M. Schubert¹, T. Stöcker¹, P. Fuierer² and R. Moos^{*1}

¹Department of Functional Materials, University of Bayreuth,
Universitätsstraße 30, 95440 Bayreuth, Germany

²Materials and Metallurgical Engineering Department, New Mexico
Institute of Mining and Technology, Socorro, 87801 New Mexico, USA

received May 2, 2015; received in revised form June 23, 2015; accepted July 14, 2015

Abstract

Ceramic materials typically have to be sintered at high temperatures, often above 1000 °C. This precludes the coating of lower-melting substrate materials, such as metals, glasses and polymers, with dense and robust thin or thick ceramic films. In addition, decomposition or uncontrolled volatilization of the ceramic components can occur at elevated temperatures. As an alternative, the Aerosol Deposition (AD) method is a spray coating process to produce dense and nanocrystalline ceramic films at room temperature directly from an initial bulk powder on almost any substrate material with no need for sintering. This great potential attracts the attention of a growing number of research groups as reflected by a rapidly growing number of publications.

The objective of this review is to give a holistic overview of the AD science and technology. It describes typical process equipment and parameters and starting powder and resulting film characteristics. Special attention is given to Al₂O₃, TiO₂, BaTiO₃ and Pb(Zr,Ti)O₃, as they represent a few of the most frequently used ceramics in AD. Aerosol Deposition of many other materials are also described to demonstrate the versatility of this new technology, its ability to realize novel combinations of materials and microstructures, and its suitability for future applications. Also discussed is the current state of understanding of aerosol deposition behavior and the experimental and modeling approaches used to explain the primary aerosol deposition mechanism(s).

Keywords: Dense ceramic films, room temperature impact consolidation (RTIC), vacuum cold spray (VCS), vacuum kinetic spraying (VKS), gas deposition.

I. Introduction

The fabrication of ceramic components or coatings often requires high sintering temperatures above 1000 °C. Joining of ceramic coatings with lower-melting materials such as metals, glasses, and polymers is difficult. Many functional and structural ceramics can be difficult to process into dense form without decomposition and/or undesirable grain growth, in some cases. It can be challenging to produce micro-electro-ceramic components based on thin or thick films. By utilizing the aerosol deposition method (in literature often abbreviated as ADM or more recently as AD), it is possible to produce highly dense (greater than 90 %, up to almost 100 %) ceramic coatings directly from an initial bulk powder without any high-temperature step on almost any substrate material. This opens up new fields for the application of ceramic coatings. Moreover, these dense films are usually nanocrystalline, which can lead to new or improved properties. A typical example of a bismuth vanadate film deposited on an alumina substrate is shown in Fig. 1. It serves as a motivation for this review.

AD film properties are strongly related to the mechanism of film formation. To date, much work has been done to investigate the mechanisms and critical material and process parameters for successful formation and adhesion of solid films by this technique. Deposition mechanisms have been postulated and supported with experiment, but the basic physical processes involved in the formation of the films have so far not been fully elucidated.

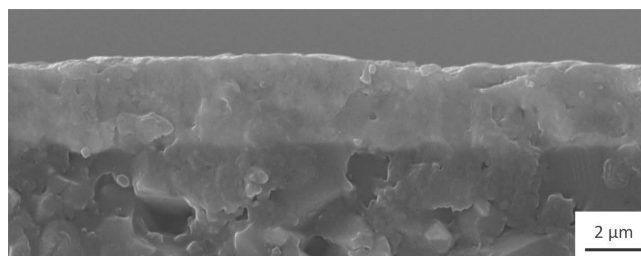


Fig. 1: SEM fracture cross-section of a ceramic film (bismuth vanadate) produced by means of aerosol deposition (AD). The AD film (less dark area on the top) is dense and exhibits excellent bonding to the alumina substrate. Reprinted from ¹ with permission from Elsevier.

* Corresponding author: functional.materials@uni-bayreuth.de

First attempts with a so-called gas deposition method (GDM) were already made in 1984². Using an evaporation system to deposit metals or an aerosol generation system to deposit ceramic ultrafine particles (UFP), films of both material classes could be produced with this spray coating technique. Akedo *et al.* picked up on this technology and modified the setup in the late 1990s³. The so-called jet molding system (JMS) worked under vacuum conditions, enabling deposition of various materials as planar films and also three-dimensional structures by masking^{3,4}. Later, the term “Aerosol Deposition Method” was used instead of “gas deposition” since the aerosol is usually not generated by vaporization of the material⁵. Many of the early investigations were conducted by Akedo and his group, evaluating opportunities for this new process and exploring underlying principles of this *room temperature impact consolidation* (RTIC). This work is highly lauded by the authors of this review.

Since its beginning at the *National Institute of Industrial Science and Technology* (AIST) in Japan, the investigation, development and application of the AD process has spread to different research groups around the world (Fig. 2 (a)). The charts show that most of the research work in the field of AD (about 90 %) has taken place in Japan and South Korea, countries with the largest number of research groups. Since the late 1990s, the publication rate in the field steadily increased to about 40 articles per year in scientific journals (Fig. 2 (b)). To date, at least 320 articles have been published in referenced, peer-reviewed journals. This review is based on many of these.

In 2008, Akedo *et al.* published the first review paper on the aerosol deposition method describing process fundamentals and a comparison and classification within spray technologies⁶. The paper also addresses the practicability of AD for fabrication of functional films, and the potential for integration of this technique into the process chain for electronic components. Since this first review, much research has been conducted with regard to mechanistic investigations, coating properties and new applications.

In this current review, we emphasize the new investigations, with connection to the previous work. In the first section, a typical AD setup is described. Next, we discuss approaches to explain the deposition mechanism(s) and important process and material parameters. In particular, we highlight similarities and differences to the cold spray (CS) process for metals as a basis towards a better understanding of significant materials properties for particle deposition and film formation in spray technology. In the main section, we cover recent work on the deposition behavior and properties of AD materials with regard to potential applications. Since this part is quite vast in treating very diverse fields, this section is split into parts, allowing selective access by the reader. Progress on the most frequently investigated materials, Al₂O₃, PZT, BaTiO₃, and TiO₂ will be discussed individually. Subsequent sections focus on special applications for AD films, such as surface protection and bio-component coatings, magnetic materials, sensors, fuel cells and batteries. Our objective is to give a holistic overview of the AD process as a new technology with emphasis on its potential for new applications and suitability as a new industrial coating process.

II. Process Principle and Setup of an AD Device

AD configurations reported in the literature show the basic components of an *aerosol generation unit*, a *deposition chamber*, and a one- or two-stage *vacuum pump* for high gas flow. Different groups use a few different names for the AD method like *Vacuum Cold Spray* (VCS)^{7,8} or *Vacuum Kinetic Spraying* (VKS)^{9,10}, but there appears to be no significant difference between the apparatus or process parameters. The original expression, “*Gas Deposition Method*” (GD)¹¹ can also be found, however, a different aerosol unit is used. The powder is loaded into a tube with connection to the deposition chamber and deposited shot-wise as a punctiform spot onto the substrate^{11,12}. More recently, the aerosol is usually generated by a fluidized bed.

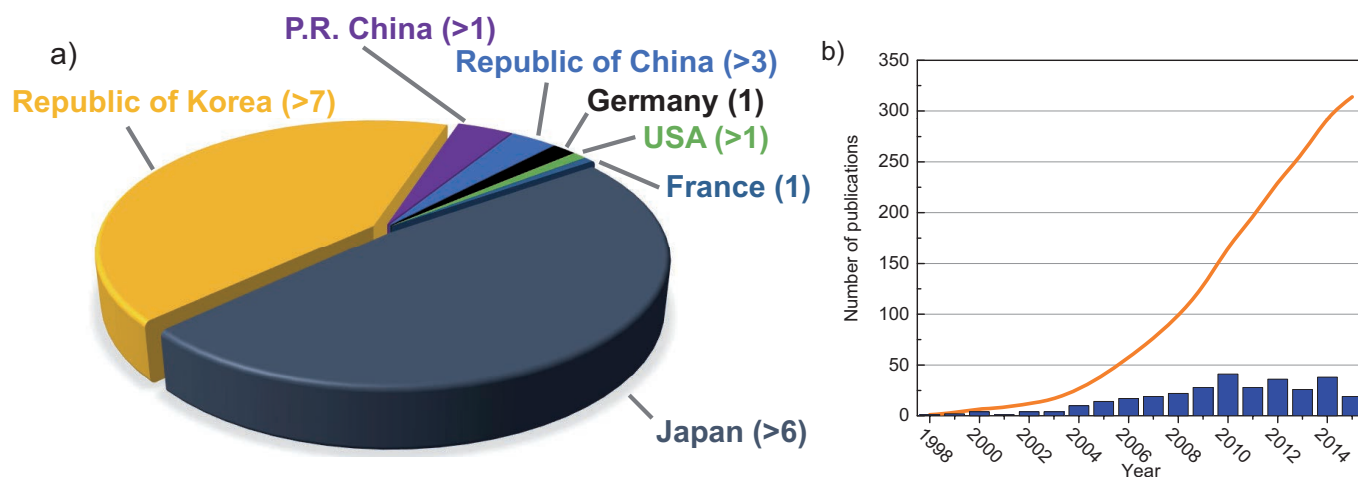


Fig. 2: (a) Distribution by country of publications related to aerosol deposition. The number of publishing research groups is given in brackets. (b) The number of AD papers published per year and cumulative.

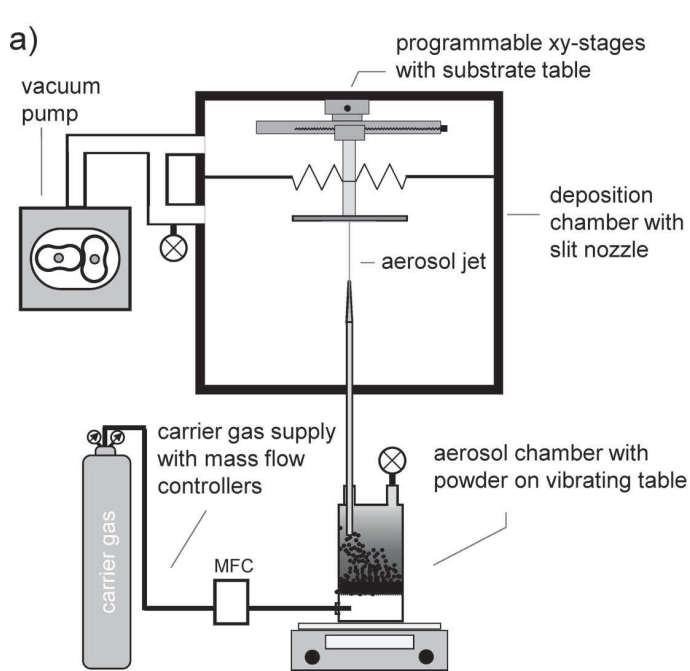


Fig. 3: (a) General schematic diagram of an AD setup (modified after ¹³) and (b) photo of an aerosol generation unit and AD chamber at the Department of Functional Materials at the University of Bayreuth.

A schematic and photo of a typical AD apparatus are shown in Fig. 3. For aerosol generation, a carrier gas is passed through loose powder contained in a vibrating chamber, thereby producing a fluidized bed. Driven by a pressure difference, the aerosolized particles are transported from the aerosol chamber through a nozzle to the evacuated deposition chamber. The aerosol is accelerated by the converging or converging-diverging (de Laval) type nozzle to velocities between 100 and 600 m/s, forming an aerosol jet at its outlet. The particles in the focused jet collide with the substrate at high speed, resulting in their breakup into nano-sized fragments that re-bond to form the ceramic film ¹.

Decisive parameters for successful deposition are usually found to be the carrier gas species, gas consumption, stand-off distance between nozzle and substrate, and the scan speed. Coating thickness and area are usually adjusted by the number and length of scans over the substrate. The calculated deposition rate is usually given in a thickness-per-time unit ($\mu\text{m}/\text{min}$), but because different nozzle geometries and deposition areas are used, values given in literature are difficult to compare. Instead, we suggest using a volume-per-time unit (mm^3/min or $\mu\text{m}\cdot\text{mm}^2/\text{min}$) with regard to usual film thickness range. Values derived from our own measurements with different powders were found to be up to $10 \text{ mm}^3/\text{min}$ ($10\,000 \mu\text{m}\cdot\text{mm}^2/\text{min}$). Table 1 summarizes deposition parameters which may affect the deposition behavior and typical values that are reported in the literature. The pressure in the deposition chamber is usually kept at a minimum of 0.2 to 20 mbar. For a setup with fixed pipe dimension and nozzle geometry, it is primarily the carrier gas (different speeds of sound) and its consumption that define the pressure in the aerosol chamber, and thus determine the pressure difference, kinetic energy and momentum of the particles in the aerosol jet ¹⁴. Commonly, simple converging slit nozzles of 2.5–25 mm in width are used for deposition, but nozzle geometry and

dimensions must also be considered as they also influence the velocity of particles in the aerosol jet.

Table 1: Typical parameters as reported for AD experiments in the literature.

Parameters	Reported data from ^{7,15–21}
Pressure in deposition chamber	0.2–20 mbar
Pressure in aerosol chamber	60–1066 mbar
Nozzle geometry	Slit nozzle 2.5 x 0.2 up to 25 x 0.8 mm ²
Carrier gas	Air, N ₂ , O ₂ , Ar, He
Gas flow rate	1 l/min - 30 l/min
Sweep speed	0.05–10 mm/s
Stand-off distance nozzle – target	0.5–50 mm

The aerosol generation is the first and very decisive step in the process. Particles of sub- μm to μm size are strongly affected by agglomeration through electrostatic surface charge and Van-der-Waals interaction. Due to their small size and high surface area, they rarely exist as individual particles but tend to form agglomerates. Agglomerates may reduce the deposition efficiency and coating quality ²². When using mechanical vibration systems for aerosol generation, this agglomeration can even be augmented. Therefore, Johnson *et al.* applied a commercial aerosol generator ¹⁷. Mihara *et al.* also used an improved design with a lifting gas separated from the carrier gas inlet. They claimed to obtain a more homogeneous film profile, but data on the constitution of the aerosol were not

shown²³. Unfortunately, re-agglomeration of particles is most likely to happen after the aerosolization due to high Brownian diffusion of small particle size²⁴.

Auxiliary equipment can and has been used as well. Ake-do *et al.* implemented a filter and a classifier in the device to produce a quality aerosol for good deposition⁶. Several studies tested de-Laval nozzles. As was found in simulations, converging-diverging de-Laval nozzles can maximize kinetic energy and improve flow characteristics and deposition behavior compared to conventional converging nozzles^{25,26}. In order to deposit large areas of 1000 cm², a slit nozzle with a 400 mm width has been reported^{19,27}. Hatono *et al.* used a multi-nozzle setup of slit nozzles (10 x 0.8 mm²) for large-area coatings on glass plates²⁸. Besides larger-area nozzles, another step towards industrial scale-up to large-area coatings is reel-to-reel processing, as mentioned in recent patent specifications²⁹.

Attempts have been made towards improvements of coating quality that go beyond aerosol generation improvements. At least as important as the equipment and process parameters are the powder properties. Criteria like particle size, size distribution, shape and crystallinity are usually considered to determine film quality. Detailed analysis and investigations are given in the next section.

III. AD Layer Microstructure and Deposition Mechanism

(1) Microstructure and morphology

No matter the type of ceramic, all successful, “standard” AD films tend to have similar appearance in SEM images. The microstructure can be described as dense and pore-free, consisting of non-distinct nanoscale grains. In cross-sectional views (Fig. 1, Fig. 4a), adherent films display intimate bonding to the substrate. In some cases involving softer ceramics, indications of plastic deformation of particles is evident in flow lines or waves parallel to the substrate^{6,30,31}.

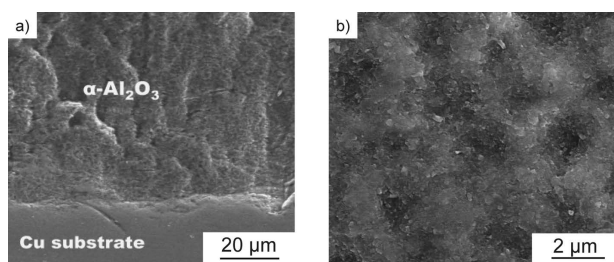


Fig. 4: SEM micrograph of an Al₂O₃ film deposited on Cu substrates using 0.5 μm particles. (a) Cross-sectional view and (b) planar view. Reprinted from³⁸ with permission from John Wiley and Sons.

One of the outstanding properties of AD films is their high density⁶, usually exceeding 95 % of the theoretical material density³². Any remaining pores in films are small, especially when compared to sintered bulk samples, with sizes between 15 and 100 nm^{30,33}. As a result of the high density, nanograined microstructure and small pore sizes, AD films are proven to be gas-tight²⁸ and show a high optical transmittance (shown for PZT and Al₂O₃)^{34,35}. According to Apetz and Bruggen³⁶, as well as Krell *et al.*³⁷, relative densities of at least 99.9 % with pore sizes below

100 nm are required to avoid light scattering and enable high transparency. Therefore, the optical appearance of films prepared by means of AD can predict their quality and integrity.

A common feature in the planar view of AD films is a surface relief with a cratering effect (Fig. 4b)³⁸. This relief is on the meso-scale, with diameter, depth, and spacing of these craters on the order of microns. It has been suggested that the craters are formed via impact of the largest particles or agglomerates in the aerosol distribution³⁸. It is also possible that they result from the preferential deposition upon large initial anchoring particles. High points may have an amplification effect due to increased deposition due to decreased stand-off distance at the peak and reduced deposition on neighboring slopes^{6,39}.

In publications by the AD community, two types of roughness values, R_a and R_q , have been used to describe the film surface. The average roughness R_a is calculated as the arithmetic mean of absolute values (vertical deviations of the roughness profile from the center line average, CLA). R_q or R_{rms} utilizes the root mean squared values instead⁴⁰. As a result of the different calculation methods, R_q is typically about 10 % larger compared to the corresponding R_a .

Lee *et al.*³⁸ reported a decreased roughness R_q with increasing number of scans from 1 to 20 for alumina films. But this set of experiments used a very low aerosol concentration in an attempt to demonstrate a “hammering” effect on previously deposited particles and their size reduction. The deposition rate and absolute thickness of these particular films were not reported. The substrate was copper, and the surface roughness was measured with a line scan of just 4 μm. A subsequent paper described the dependence of deposition rate and roughness on the substrate material⁴⁰. Measurement details were not given (a 4-μm line scan might be presumed from earlier work), but it was reported that harder substrates (polycrystalline alumina and sapphire) resulted in higher R_q roughness values than softer substrates (Cu, glass). Micrographs suggest that the cratering effect is more pronounced on copper, the softest substrate.

On the other hand, using “normal” deposition conditions (i.e. relatively high aerosol concentration and deposition rates), the same group (Lee *et al.*³¹) found an increased roughness with increasing number of scans and film thickness for polished copper substrates (see Fig. 5). In these experiments, R_q was measured by means of AFM imaging over scan areas (40 μm x 40 μm) which included at least a few surface special wavelengths (SSW) produced by the cratering. Roughness values were therefore somewhat higher than reported in the case described in the previous paragraph. In a similar way, AD alumina films on glass and alumina substrates show increased roughness with large number of scans. The curves for alumina and glass substrates in Fig. 5 were derived from our own experiments with films deposited at the University of Bayreuth, and averages of five 10 x 10 micron AFM images acquired at the New Mexico Tech. Altogether, these results suggest a trend toward higher film roughness with increased substrate hardness and roughness.

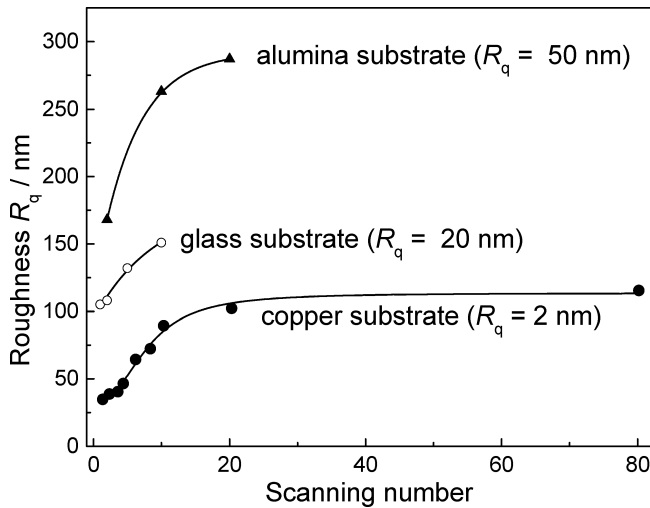


Fig. 5: Roughness of AD Al_2O_3 films as a function of number of deposition scans and substrate material. Data for alumina and glass substrates are from unpublished work from the authors' group, modified after ³¹.

Recent publications by Piechowiak *et al.* ¹⁵ and Henon *et al.* ³⁰, also show a cratering effect with MAX phase Ti_3SiC_2 (Fig. 6a and Fig. 6b), and similar behavior where the roughness increases with film thickness (Fig. 6c). Though absolute crater size increased, the relative crater depth decreased with thickness. The plot shown in Fig. 6c

also illustrates a transition from the first stage anchor layer formation, where bonded crystallites near the substrate are observed to be 20 nm in size, to second stage film buildup, where grain sizes of up to 200 nm with wave-like patterns are observed. The authors suggest a corresponding mechanism that changes from brittle fragmentation to more plastic deformation. Softer ceramics may or may not exhibit the cratering, but in any case give relatively rough films as deposited. In some cases, such as $BaTiO_3$ ⁴¹, roughness has been reduced through annealing, while in other cases, such as copper and titanium substituted bismuth vanadate films ($BiCuTiVO_x$), roughness increases with annealing when significant grain growth occurs ¹.

AD coatings should not be generally classified as "conformal". The topography of the AD layer surface does not necessarily correlate to the initial underlying surface topography. Resulting coating roughness depends on the deposition mechanism of the anchor layer (which depends on the nature of the substrate), as well as on the nature of the aerosolized particles, their distribution and impact velocities during the growth stage. At small length scales, roughness values may be small due to nanoscale particles, but at larger length scales, topography may be dominated by self-inflicted damage from the impact of larger particles in the distribution, which gives surface undulations or cratering with large SSW.

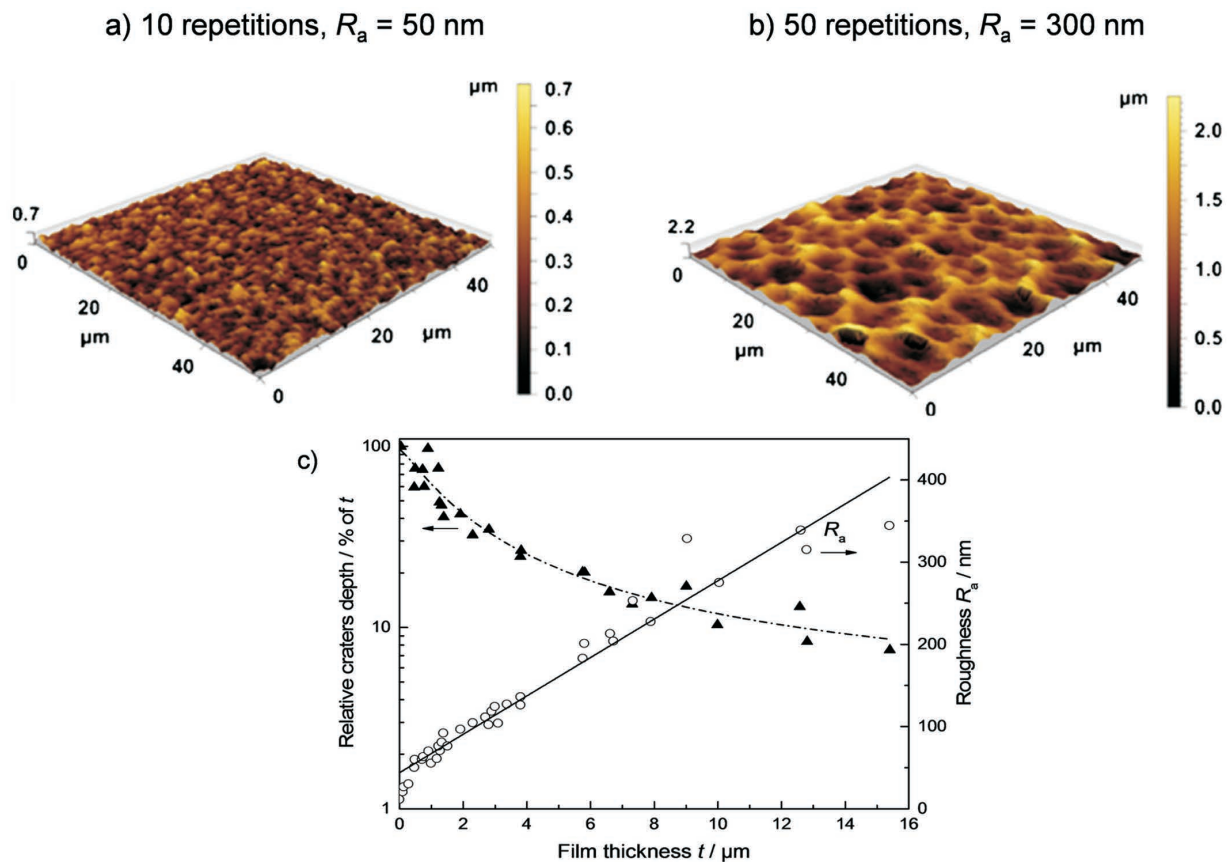


Fig. 6: AFM analysis of AD Ti_3SiC_2 films on glass substrate. (a) 10 repetitions, thickness $t = 1.2$ μm , $R_a = 50$ nm (b) 50 repetitions, thickness $t = 10$ μm , $R_a = 300$ nm. (Both scans are 50 x 50 μm . Z-height scale is different for each according to peak-to-valley height.) Reprinted from ¹⁵ with permission from Elsevier. c) Roughness and relative crater depth as a function of film thickness, modified after ³⁰.

Beside the unusual but characteristic film microstructure, the crystalline phase composition can be affected by aerosol deposition. In most cases, the crystalline phases found in the powder are retained in the sprayed film, so no major phase transformations takes place during deposition^{1, 42, 43}. However, a few materials may tend to undergo a phase change during AD⁴⁴. For example, Iwata *et al.* observed a hexagonal to cubic crystal structure transformation in aluminum nitride^{45, 46}. Ryu *et al.* used electron beam diffraction to detect a highly disordered, amorphous TiO₂-phase within a nanocrystallite anatase AD film⁴⁷. This is perhaps an extreme case of the typical decrease in XRD crystallinity accompanying the *in situ* grain size reduction.

(2) Mechanisms

AD is in some ways analogous to cold spraying (CS), where a dilute-metals-particle-laden pressurized gas is accelerated to supersonic velocities in the range of 500–1000 m/s using a converging-diverging nozzle⁴⁸. Experimental and numerical studies^{49–51} have focused on parameters influencing the particle velocity, temperature and pressure of the primary gas, the cross-sectional area of the nozzle throat, and the nozzle-substrate stand-off distance. CS relies on plastic deformation, adiabatic shear instability and the creation of a metallic jet to allow metallic bonding to take place at substrate-particle and

particle-particle interfaces⁵². The criterion for effective bonding in CS has been explained based on the adiabatic shear instability (ASI) of the particle⁵³. According to Schmidt *et al.*^{52, 54}, the most important criterion for deposition is that the impact velocity exceeds a material-dependent critical velocity (Fig. 7). There is another critical velocity at which a transition from particle deposition to substrate erosion takes place^{52, 55}.

Attempts to deposit a ceramic (TiO₂) using CS apparatus at the Helmut-Schmidt-University in Hamburg met with limited success⁵⁶. While single layer films were possible using a ductile, metallic substrate, buildup of thick films appeared to be difficult given typical CS process parameters. The authors suggest that bonding of ceramics using CS depends on shear instabilities in the substrate. In most cases, brittle ceramics erode the substrate.

An AD apparatus uses different process parameters than CS. Lower absolute pressures, no gas preheating, and smaller starting particle size lead to lower particle speeds and lower temperatures upon impact⁶. Critical velocities are believed to exist for AD as well^{14, 55}. For AD ceramics, these velocities and deposition efficiencies appear to be lower than in CS (Fig. 7), although they have not been precisely quantified and are material (particle and substrate) dependent. Akedo has suggested a critical velocity of about 150 m/s for AD Al₂O₃ and PZT¹⁴.

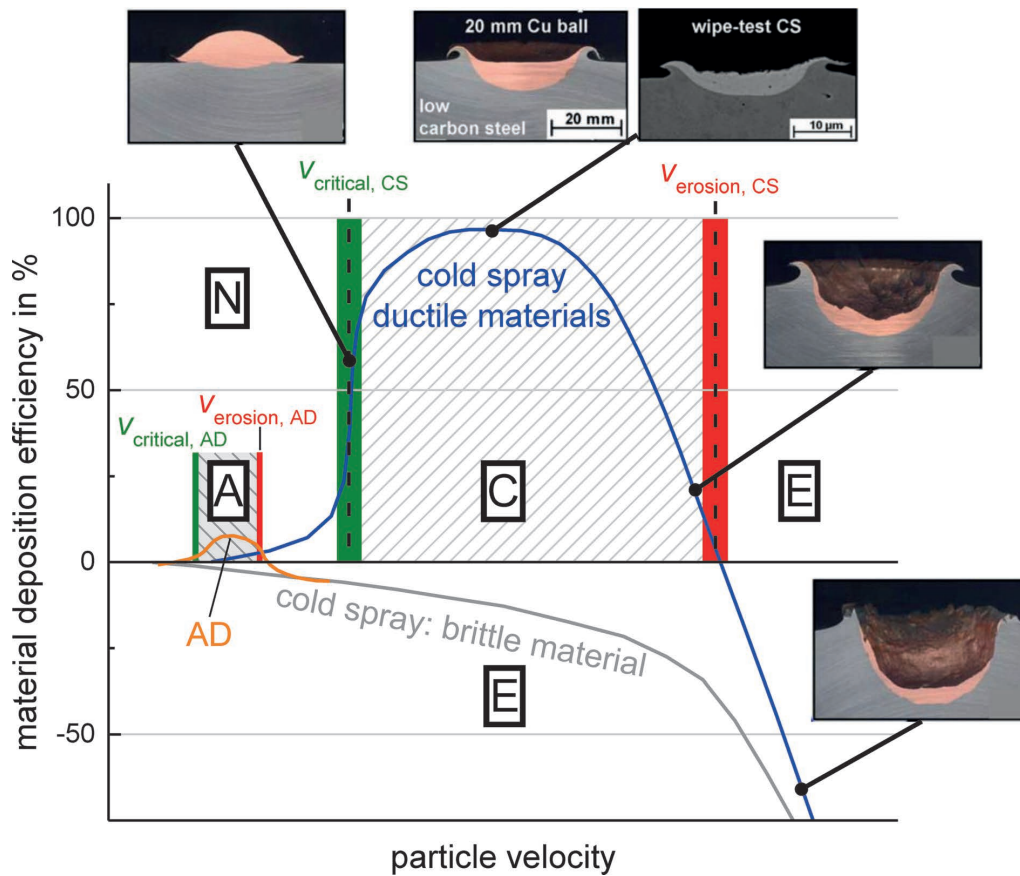


Fig. 7: A possible “Deposition Window” (deposition efficiency vs particle velocity during impact) for AD (area A) compared to that for cold spray of ductile metal (area C). Erosion takes places for very high particle velocities and during cold spray of brittle materials (area E). For particle velocities below $v_{critical}$, no deposition occurs (area N) (modified from⁵²).

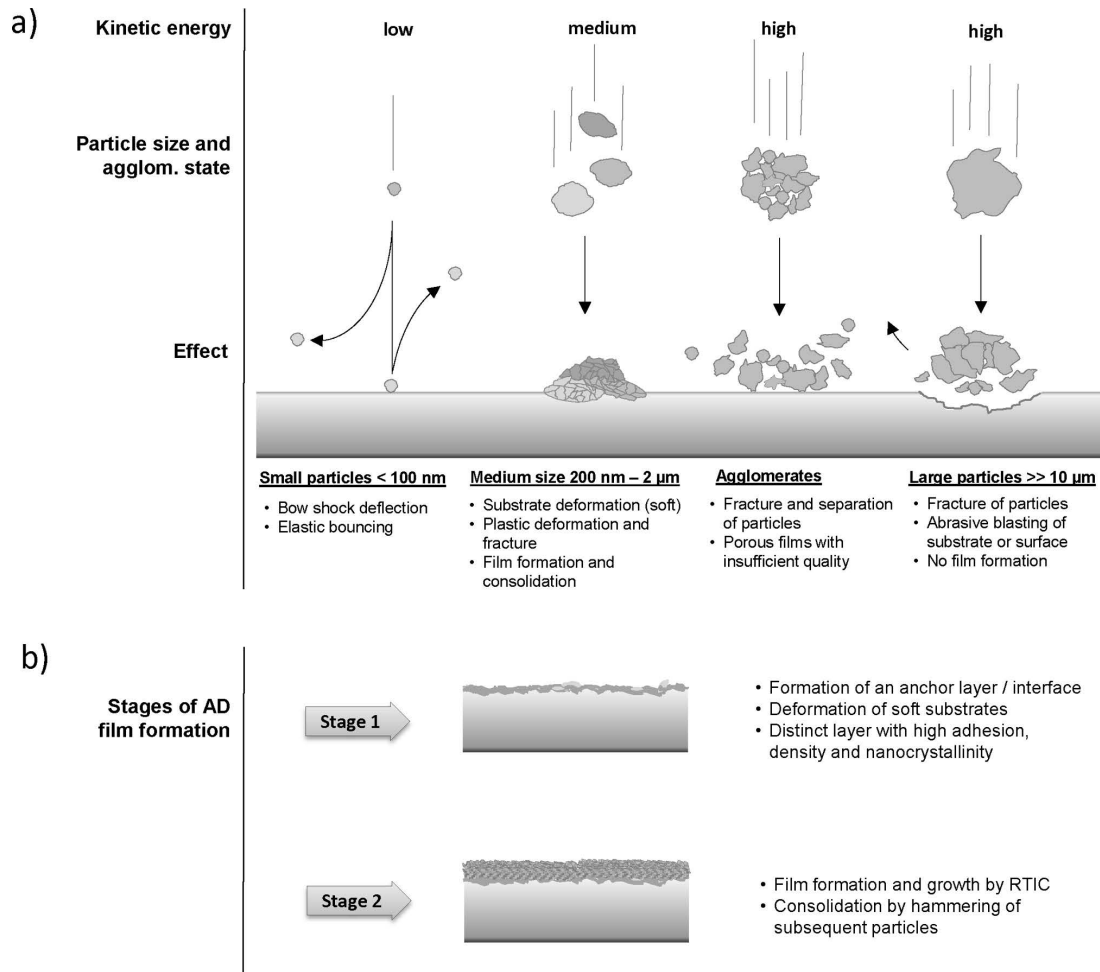


Fig. 8: a) Illustration of possible particle-substrate interactions based on the speed and kinetic energy of the ceramic particles. Anchor layer formation can take place at intermediate energies. b) The room temperature impact consolidation (RTIC) process, with distinction between stage 1 (anchor layer formation) and stage 2 (film buildup), during which particle hammering and fracturing takes place. Modified after ¹³.

The bonding mechanism for brittle particles is likely different than for CS metals. During particle collision with the substrate, a portion of the kinetic energy is converted into a bonding energy. According to Akedo ^{6,14}, dense structures result due to the reduction of crystallite size by fracture and/or plastic deformation rather than by local melting. This statement is supported by experimental observation of crystallite size, along with simple simulations ¹⁴. Lee *et al.* ³⁸ studied AD of Al₂O₃ using careful sequential SEM and AFM experiments with increasing number of scans and concluded that the initial anchor layer is formed by plastic deformation of Al₂O₃ particles, even on a compliant copper substrate. They proposed that particle deformation and cracking due to a hammering effect of subsequent bombarding particles is the main deposition mechanism. Thus, the AD process is appropriately also called room temperature impact consolidation (RTIC).

Fig. 8 shows a schematic of the process. Depending on the particle size and state of agglomeration, different processes can take place during the impact, as described in Fig. 8a. Very small particles (<< 100 nm) with low kinetic energy are significantly slowed down by bow shocks and the stagnation point of the flow, and therefore get deflected before they reach the substrate or bounce elastically. Sufficiently sized particles (200 nm – 5 μm) undergo the described RTIC mechanism during impact by fracturing and plas-

tic deformation and therefore adhere to the substrate or the already deposited film. The reported empirical particle ranges are convenient for most materials, but still are dependent on material properties like hardness, fracture toughness and density. Larger particles (>> 10 μm) obtain kinetic energies that are too high, leading to an abrasive blasting of the substrate/film (similar to sand-blasting). These particles are likely to fracture too, but without plastic deformation. Even if a powder contains appropriately-sized particles, agglomeration can still disturb the deposition. Agglomerates absorb a part of the kinetic energy and affect the momentum transfer between particle and surface while impacting, and by that, impede the RTIC process. Films then tend to be porous, with decreased strength and adhesion.

The AD process can be separated into two stages (Fig. 8b), the creation of an anchor layer (1), and subsequent film buildup (2). Stage (1) includes an initial plastic deformation of the substrate surface by first impacting particles, associated with an increase of the roughness (especially for softer substrate materials like metal and glass). Mechanical entanglement might also play a more important role in the buildup stage ⁵⁶. Film growth in stage (2) takes place by RTIC of subsequent particles.

Very recent work at Sandia National Labs⁵⁷ has provided direct evidence for the plastic deformation of submicron Al_2O_3 using *in situ* compression experiments on a single particle. While $3\ \mu\text{m}$ particles, which were highly defective single crystals, fractured into many pieces in a brittle manner under load, the defect-free $0.3\ \mu\text{m}$ particles deformed plastically with relatively large accumulated strain before fracturing and becoming polycrystalline. During deformation, dislocation activity was observed within these small particles. Yoshida *et al.* used a comparable compression test system to investigate the strength of submicron Al_2O_3 particles⁵⁸. In this case, ductile deformation was not witnessed, either due to the particle size or the imaging limitations of the experiment. Brittle fracture was assumed, and a mean strength of 2.9 GPa was determined by means of Weibull analysis for particles with average size of $0.7\ \mu\text{m}$ diameter. This measured strength is on the order of the impact pressure calculated from modeling experiments (see next section). Though these experiments are static rather than the dynamic, high rate impacts during AD, it is a first step in understanding the mechanisms⁵⁷.

Akedo⁶ suggested that the following questions about AD remain unanswered: *Does the creation of clean and active particle surfaces make bonding possible at low temperature? Is there a chemical reaction during impact?* Nao *et al.* have recently published one of the few papers with direct evidence of chemical bonding between anchoring Al_2O_3 particles and the copper substrate, as electron energy-loss spectra (EELS) from the interface suggested the presence of ionic and covalent bonding between Cu (substrate) and $\text{O}^{2-}(\text{Al}_2\text{O}_3)$ ⁵⁹.

There is much evidence that the anchor layer is critical to film adhesion and stability⁶⁰. Substrate properties, of course, influence the deposition and determine the dominant bonding mechanism, especially in the first stage. It has been demonstrated how substrate hardness affects AD film properties⁴⁰. Ductile and/or low-melting substrates can be expected to give strong film anchoring by local interface deformation and perhaps melting. High hardness substrates can be expected to lead to efficient particle size reduction and dense consolidation as the film grows in thickness, but might require higher velocity particles to

form an adherent anchor layer initially. Very recent work by Kim *et al.*⁶¹ demonstrated that the unique properties of bulk metallic glasses provided for both excellent adhesion and effective consolidation of an Y_2O_3 layer. The initial substrate roughness plays an important role. Kim *et al.* investigated the influence of an Al_2O_3 interlayer on metallic aluminum produced by plasma electrolytic oxidation with differing roughness, R_a . Increasing R_a from 0.4 to $0.9\ \mu\text{m}$ decreased the deposition rate, and R_a above $1.5\ \mu\text{m}$ completely inhibited the formation of an AD layer. It is believed that an increased surface roughness prevents the deposition of particles, especially when the depth of the surface valleys is greater than the particle size⁶². Maki *et al.* showed a strong reduction of the deposition rate above a deposition angle of 30° (angle between the aerosol jet axis and the substrate normal.)⁶³. This can help to explain the negative effects of substrate roughness, and the non-conformal nature of AD coatings.

(3) Modeling

Finite element modeling (FEM) simulations of a single particle impact with a substrate were conducted using the AUTODYN software with the Johnson-Holmquist-2 material model (JH-2)^{64,65} to estimate local temperature and shock pressures as shown in Fig. 9¹⁴, which appear to be sufficient to overcome the fracture toughness of $\alpha\text{-Al}_2\text{O}_3$ and fracture the particles⁵⁸. Molecular Dynamics (MD) simulations were first conducted by Ogawa^{66–68} for single particle impacts. ZrO_2 was selected as the ceramic, with known interatomic potentials. Particles were $10\ \text{nm}$ in diameter, with 60 000 atoms being considered for calculation. With a threshold speed of $500\ \text{m/s}$, slip planes inside the particle were activated upon collision with the substrate, and the particle was subdivided into a few grains. The mechanism is enhanced at higher speeds, until a speed at which the crystal structure is destroyed and a disordered (amorphous) phase can appear. It is unknown whether ceramic particles in AD reach these velocities. Variation of the incident angles was also shown to affect the manner of deposition, leading to particle rolling, a tail structure, and activation of different slip planes in the substrate⁶⁷.

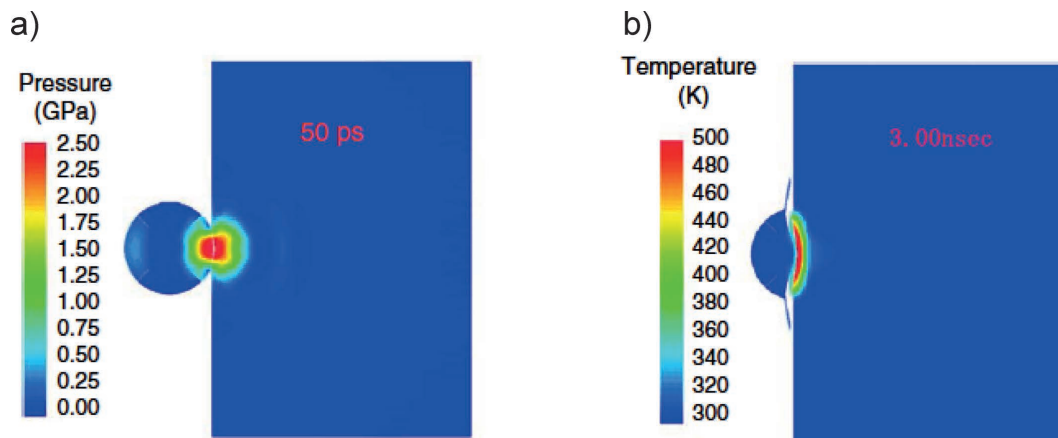


Fig. 9: FEM simulation of the local rise in temperature and shock pressure during impact of particle with the substrate for AD deposition. Impact particle velocity was $300\ \text{m/s}$. Reprinted from¹⁴ with permission from John Wiley and Sons.

Recently, Daneshian and Assadi⁶⁹ furthered the work by Ogawa by increasing the particle size to 50 nm, and utilizing a Lennard-Jones potential together with a cut-off radius, $r_c < r/\sigma$, to select a level of brittleness, where r is the atomic separation, and σ is the characteristic length parameter in the Lennard-Jones model. Simulations were done for different particle size and velocity, showing that particles do begin to deform without breaking as the particle falls below a critical size, and that deformation can be accompanied by polycrystallization and bonding to the substrate. The results were summarized in a parameter selection map showing conditions for successful deposition of brittle materials (see Fig. 10). While this affords a good qualitative description of the process, it is unclear how well it matches AD experiments quantitatively. The Sandia National Labs group conducted atomistic simulations of nanoparticles in compression, which showed that the dislocation slip during plastic deformation only occurs in perfect crystallites. Simulations of same-size submicron particles with pre-existing flaws showed signs of brittle fracture like the larger particles. This corroborated their experimental observations, described earlier in the previous section⁵⁷.

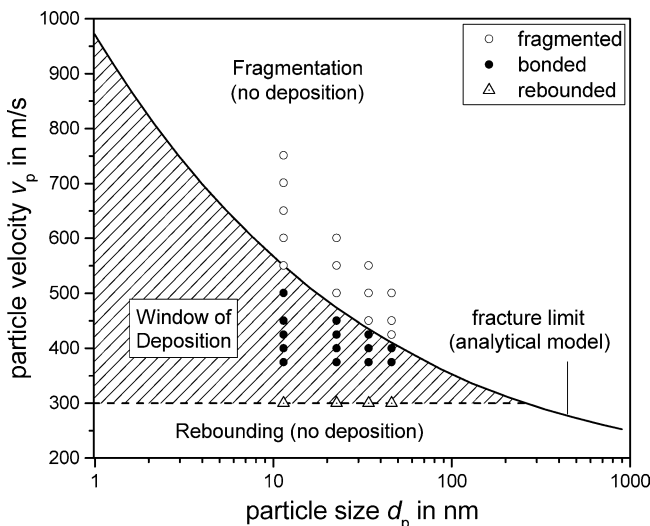


Fig. 10: The window of deposition as function of the average particle diameter d_p and velocity v_p for intrinsically brittle materials; from molecular dynamics simulations in comparison to analytical fracture model (after⁶⁹).

While these simple models are a start, they are not sufficient to describe the AD phenomenon thoroughly. They are either static/low rate or are single particle, although a more recent study by Chun *et al.*⁷⁰ conducted a two-particle numerical analysis yielding a max temperature (600 K) and pressure (5 GPa) comparable to Akedo's single-particle simulations. Most are 2-dimensional, and do not involve the transient effects of fracture and deformation of the previously deposited particles on the surface, or the mechanical interaction of particles between themselves. More satisfying would be a multi-particle, 3-D, time-dependent simulation. The JH-2 is a ceramic constitutive model used within hydrodynamic code for explicit dynamic simulations of high strain rate behavior (typically impacts at the macro-scale)^{64,65}. It uses time-dependent material parameters (elastic at time 0, nonlinear thereafter). A difficulty with the JH2 is that it requires several

material constants, a few of which are familiar (e.g. mass density, shear and bulk moduli, tensile strength), but many others can only be inferred from uncommon flyer plate experiments or ballistic impact tests. Consequently, the full range of constitutive constants necessary for AD simulation are only obtainable for ceramics being considered for armor and other ballistic type applications. Realistic impact modeling of micro-particles during AD is therefore challenging, but is an area of great interest.

Simulations of the particle-laden gas flow are also important for a homogeneous film thickness and quality. Lee *et al.*^{25,26}, as well as Schmidt *et al.*⁵², simulated the effects of the nozzle geometry and spray conditions on the flow characteristics in aerosol spray processes. Non-optimized nozzles generate shockwaves in the gas flow between the nozzle opening and the substrate, leading to an increased expansion and fluctuation of the carrier gas, thereby giving non-uniform coatings. However, an optimization by decreasing the chamber pressure and increasing the diverging angle drastically improved the flow uniformity and particle velocity. Another crucial effect is the formation of a bow shock area right before the substrate. A higher pressure and density within this area increases drag on particles. Smaller particles with lower kinetic energies can be deflected by the stagnation point of the gas flow. Modeling of the complete aerosol deposition process, including aerosol generation, gas flow dynamics with ceramic particle interaction and eventually the deposition of particles has a very large and complex scope. However, progress in this area would greatly improve the general understanding and the ability to predict and control the film deposition.

(4) Material parameter effects

All AD studies have found that adhesion and film quality depend not only on process parameters, but also on particle size, distribution, agglomeration, moisture, etc. of the starting ceramic powders. Ceramic powders with a primary particle size range of about 0.08 – 2 μm and a compact spherical shape are typically used as the deposition particles. The ratio of deposited to non-deposited particles strongly depends on the particle size and on the degree of agglomeration, so de-agglomeration devices and/or filters are sometimes used between aerosol generator and the deposition chamber⁶. Akedo⁷¹ also reported an optimal powder milling time prior to deposition of PZT powder. Subsequent groups report a powder pretreatment regimen involving high-energy milling^{1,23,60}. This suggests that a residual strain in the crystal lattice of particles may be a prerequisite for deposition. Defects and strain correspond to elevated stored free energy and may enhance particle bonding. They can also assist the fracturing of particles on impact. But these hypotheses have not been fully explored yet.

The right choice of raw powder is crucial for the success of AD. Powder characteristics are important at every stage, from generation of the aerosol, to particle acceleration in the nozzle, to impact, packing, and bonding. Average particle size alone is not sufficient information, and is also complicated by agglomeration. Particle porosity, roughness, surface area, and inter-particle friction are also expected to be of consequence. The compressibility

index (*CI*) is dependent on all of these characteristics, and is used in traditional ceramic processing as an indicator for flowability of powders⁷². It may be a figure of merit for starting powders used for AD. Exner *et al.*⁶⁰ recently correlated the *CI* and the specific surface area (S_{BET}) of Al_2O_3 powders, to the resulting quality of films produced by aerosol deposition. For alumina substrates (high hardness), it was found that a high powder specific surface area (5.5 to $8 \text{ m}^2/\text{g}$) is correlated with good film deposition and adhesion. For glass substrates, high-quality, well-adhered, stable AD films were associated with lower S_{BET} (less than $3.5 \text{ m}^2/\text{g}$) and a compressibility index within a tight range of about 44 to 47 % (see Fig. 11). Fig. 12 illustrates the changes that occur during high-energy milling: size reduction and broadening, loose agglomeration, and texturing of surfaces, all of which may play a role in deposition. Work remains to separate and quantify the relative effects of these characteristics, for hard and soft ceramics.

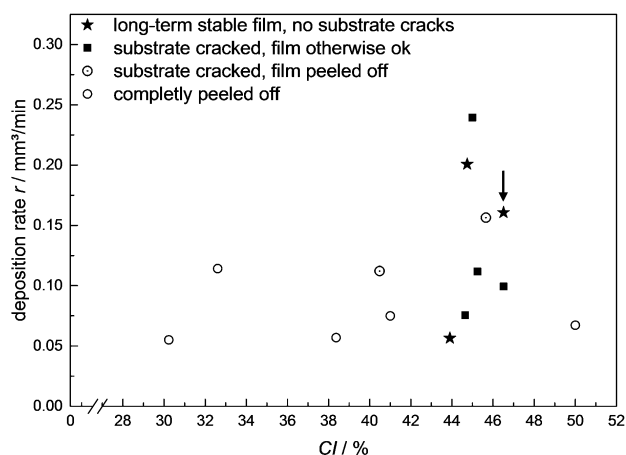


Fig. 11: Empirical study on aerosol deposition rate and film quality on glass substrates plotted against the compressibility index of alumina powders (post grinding) (modified using data of⁶⁰). The symbols denote the quality of the deposited films. The arrow indicates the powder in Fig. 12. Reprinted from⁶⁰ with permission from Elsevier.

(5) Aerosol co-deposition (AcD)

AD has already enabled a variety of ceramic films on many different substrates. Resulting films usually exhibit mechanical and physical properties similar to the bulk. The opportunity to produce composite films via aerosol co-deposition (AcD) adds another degree of freedom to the process⁷³. While AD sprays only a single ceramic powder, AcD utilizes a powder mixture of two or more materials. These mixtures can consist of varying ratios of ceramic^{14,74,75}, metallic^{76–78} or polymeric^{79–81} components, and can include exotic materials like graphene^{82,83}, carbon nanotubes⁸⁴, or chitosan⁸⁵. The term “aerosol co-deposition of ceramics (AcDc)” has been used in the special case when solely ceramic powder mixtures are deposited⁷³.

By forming a composite film, properties can be adjusted, for instance, electrical parameters like conductivity⁸⁶ or permittivity⁸⁷, as well as mechanical characteristics like hardness⁸⁸, porosity⁸⁹, or adhesion to the substrate⁹⁰. AcD films can also be dense and can exhibit uniformly distributed components. Depending on the mixing ratio and relative particle sizes of the aerosolized powders, one can

obtain either a dispersion of one phase in a continuous matrix of the other (Fig. 13a), or two interpenetrating continuous phases (Fig. 13b)⁷³.

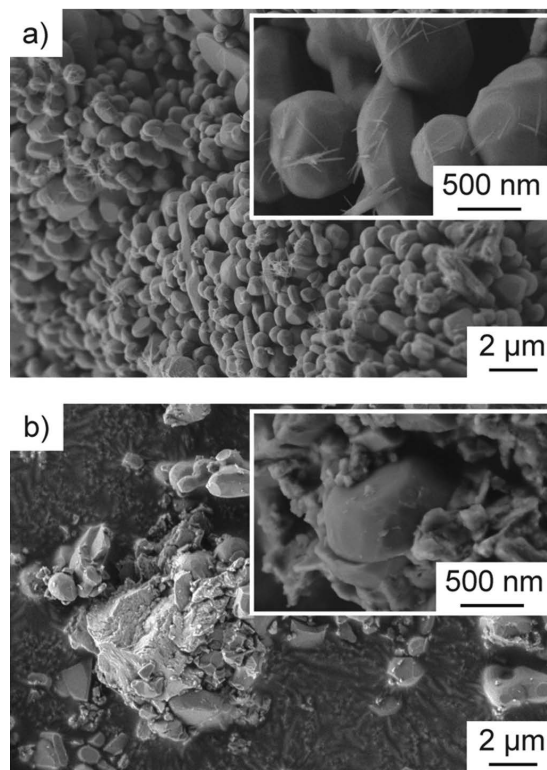


Fig. 12: SEM of a commercial $\alpha\text{-Al}_2\text{O}_3$ powder (indicated by the arrow in Fig. 11); before and after high-energy milling, which was successful in depositing good quality films on glass substrates. Reprinted from⁶⁰ with permission from Elsevier.

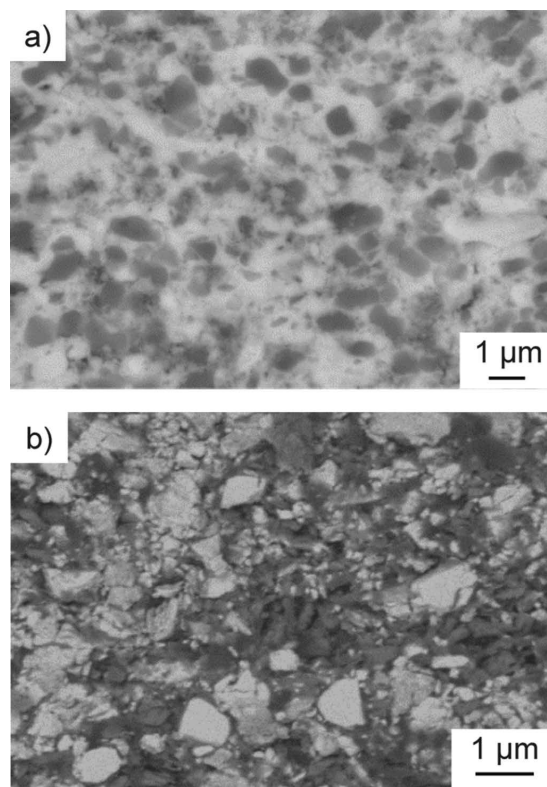


Fig. 13: Cross-sectional SEM image of AcDc composite films a) dark TiO_2 -particles dispersed within a bright continuous Bi_2O_3 -matrix b) random mixture of continuous V_2O_5 (dark) and Bi_2O_3 (bright) particles. Reprinted from⁷³ with permission from John Wiley and Sons.

The RTIC process is still the dominant deposition mechanism in AcD, but differences can occur during impact of powder species with varying properties like hardness, density and particle size. Especially for powders with widely differing hardnesses, only the softer material is likely to undergo deposition by means of RTIC as a matter of fracturing and plastic deformation, while the much harder material tends to get embedded in the softer one without fracturing. However, harder particles can improve the overall densification of the film by a peening and hammering effect⁷³. Due to possibly diverging aerosolization and deposition behaviors, a change of film composition from the starting powder mixture can occur^{91,92}, which should be taken into consideration.

With AcD, some film characteristics can be realized that cannot be achieved with conventional AD. While AD typically leads to dense films, AcD can enable the formation of porosity (in order to increase the film surface area or permeability) by introducing a fugitive phase in the film. This phase can then be removed in a film after-treatment, either by leaching (tricalcium phosphate with hydrochloric acid)⁹³ or by burning out a polymer (polyethylene glycol/PEG⁷⁹, polyvinylidene fluoride/PVDF⁹²). These films with porosities up to 50 % maintain a good strength and adhesion to the substrate²⁰. Polymeric substitutions like polytetrafluoroethylene (PTFE) also proved beneficial for AcD coatings on flexible integrated substrates^{94,95} and PET⁹⁶ by giving plasticity to the films and avoiding erosion of the soft substrates by absorbing high energies during deposition. Additionally, a reduction of residual film stresses can be achieved⁹⁷. By avoiding impact fracturing, the crystallite size of the ceramic starting powder is retained, and distortion of the crystal structure is also avoided^{80,87,94}.

Electrical properties of thick films can easily be tuned using mixtures. The alumina content within the composite film was calculated from permittivity values of films (Fig. 14a)⁹¹. As found from these results, there is a preferred deposition of polyimide, since the content in the film is higher compared to the sprayed powder. The

electrical conductivity of SiC was increased significantly with the addition of TiN above the percolation threshold (Fig. 14b)^{8,77,83,86}. The oxidation resistance can also be increased with composite films^{85,92,98}.

Beyond the changes expected to occur with annealing, such as increased crystallinity, elimination of structural defects⁷⁴, another variation is to *in situ* calcine a composite AcD film at an appropriate temperature so that a single-phase material results. This of course requires a well-controlled stoichiometry and a homogenous distribution of phases within the composite film to enable the formation of the intended compound. Exner *et al.*⁷³ very recently demonstrated that calcination of an AcDc film (shown in Fig. 13a) led to a single phase Bi₄Ti₃O₁₂ film with high and uniform porosity.

IV. Materials and Applications

AD is a process with the potential to manufacture a large variety of ceramics, oxide and non-oxide, for a variety of applications, functional and passivation. This broad range of materials and applications is reflected in the literature. The most carefully investigated materials, Al₂O₃ (Section 4.1), PZT (4.2), BaTiO₃ (4.3), and TiO₂ (4.4) will be discussed individually in this overview, with special respect to possible applications for AD. The subsequent sections are divided into the application fields of surface protection coatings (4.5), biocomponents (4.6), magnetic materials (4.7), sensing applications (4.8), energy applications in fuel cells (4.9) and secondary battery systems (4.10).

(1) Alumina (Al₂O₃)

Alumina is an oxide ceramic with widespread applications owing to its outstanding chemical (inert), mechanical and dielectric properties⁹⁹. Its use as protective, insulating, or wear-resistant coatings might be improved and broadened by applying dense films on temperature-sensitive and flexible substrate materials via AD (see Fig. 15). With around 50 publications, alumina is one of the most frequently examined materials for AD. As mentioned earlier, most fundamental research is conducted on this material.

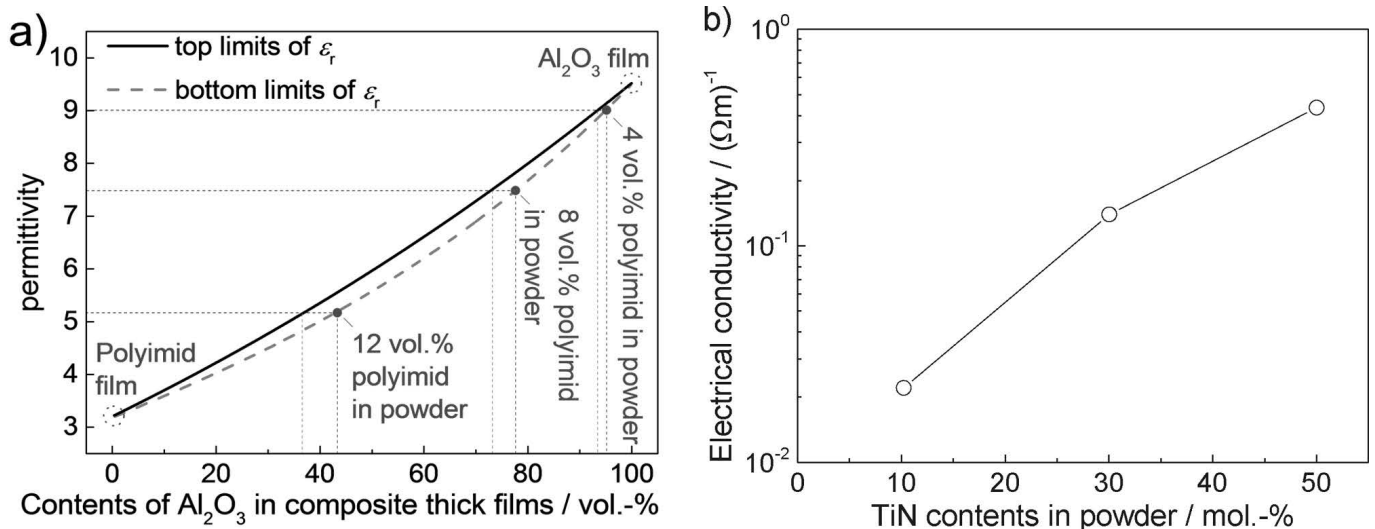


Fig. 14: Influence of composite film contents on a) relative permittivity of an Al₂O₃-polyimide composite film (modified after⁹¹) b) electrical conductivity of a SiC-TiN composite films (modified after⁸).

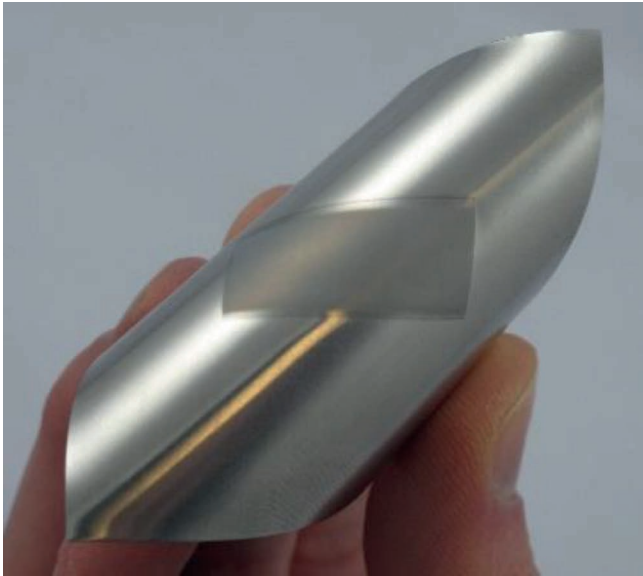


Fig. 15: Alumina coating ($10 \times 20 \text{ mm}^2$, thickness $8 \mu\text{m}$) on a flexible steel foil. Courtesy of Dept. of Functional Materials, University of Bayreuth.

With regard to the mechanical properties of AD alumina, hardnesses between 1100 HV and 1800 HV^{40, 97, 101, 102} (bulk value 2600–2700 HV¹⁰⁰) and a good adhesive strength (64 MPa) to the substrate¹⁰³ have been obtained. Owing to these excellent mechanical properties, anti-scratch and anti-smudge¹⁰⁴, as well as anti-wear coatings can be envisaged by means of AD. Specifically, hard and smooth AD Al_2O_3 surfaces on industrial rollers are being considered instead of Cr-plating¹⁰¹. Good chemical stability and corrosion resistance at a neutral salt spray test was reported¹⁰¹ (details in Section 4.5). A thermally protective AD Al_2O_3 coating on Al substrates for heat radiation applications has also been reported¹⁰⁵.

It should be mentioned that a very common epiphenomenon of hard AD films is the high residual film stress⁸⁰, found to be as high as 2 GPa when nitrogen is used as carrier gas⁴². Using oxygen instead of nitrogen as the carrier gas reduces this residual stress by 50 % and by additional annealing of the films at only 300 °C, the residual stress was eliminated completely⁴².

The electrical properties of alumina AD films have been intensively investigated. Films have been produced with low leakage current up to a bias of 100 V (film thickness $10 \mu\text{m}$)¹⁰⁶ and high electric breakdown fields of $>60 \text{ kV/mm}$ ^{106, 107}. They have a dielectric constant (between 7 and 10) and a low dielectric loss ($\tan \delta$ between 0.005 and 0.05^{22, 80, 95, 108–110}) comparable to bulk material (9.9 and 0.0002 respectively at RF frequencies⁹⁹)^{22, 80, 95, 109, 110}. D.W. Lee *et al.* showed that the dielectric properties can be influenced by the choice of starting powder¹⁰⁹. Small particles ($0.5 \mu\text{m}$) built a film with a grain size of 10 nm, showing frequency-independent electric properties ($\tan \delta$ of 0.05 and relative permittivity of 9.4); whereas larger and agglomerated Al_2O_3 particles built a film with larger grain size showing higher dielectric constant and loss with stronger frequency dependence. Al_2O_3 dielectric layers are discussed for metal core circuit boards for LEDs¹⁰⁶ and for integrated substrates.

Alumina films are also suggested for band pass filters (RF modules).

Concerning the optical properties of AD alumina, it is possible to produce highly transparent films of up to 80 % transmittance in the wavelength between 350 nm and 900 nm at a film thickness of $0.6 \mu\text{m}$ ³². The transmittance decreases with increasing film thickness and also with increasing particle velocity. Transmittance decreases due to Mie scattering below 800 nm as the wavelength approaches the size of the crushed particles¹⁰⁷.

As mentioned in the previous section, properties can be varied by co-depositing Al_2O_3 /polymer composite films. The residual stress can be reduced by adding polytetrafluoroethylene (PTFE)⁹⁷ or polyimide (PI)⁸⁰. Of course such composites enhance the plasticity of the deposited films due to the intrinsic plasticity of the polymer^{80, 95}. Kwon *et al.* investigated the difference between using PI, a thermosetting polymer, and polymethylmethacrylate (PMMA), a thermoplastic with lower hardness and shear modulus, in a 70/30 vol% Al_2O_3 /polymer mixture⁸⁸. In both cases, the surface morphology was described as similar to the single phase Al_2O_3 films, but hardness was significantly reduced from that of Al_2O_3 films (1200 HV) as expected. However, there were significant differences between the two polymer admixtures (PMMA vs PI) as seen in deposition rate (low vs high), crystallite size (35 nm vs 47 nm), and hardness (202 HV vs 25 HV) respectively. The somewhat surprising results are explained by a difference in impact behavior; distortion of PMMA vs fragmentation of PI particles. Ultimately, there was a lower amount of PMMA actually remaining in the composite film, which was responsible for the higher hardness of the composite, despite the lower hardness of PMMA. The proposed difference in the deposition mechanism, attributed to a difference in mechanical properties of the two polymers, is depicted in Fig. 16⁸⁸.

Al_2O_3 -polymer composites have also been used to tune the dielectric properties of AD films. By adding PI or PTFE, the dielectric constant was adjusted down to 4.5 and the dielectric loss was reduced by a factor of 2 to 0.01^{108, 111}. The low dielectric constant and loss are attractive for embedding passive components via 3D integration (system in package).^{80, 108}

(2) PZT ($\text{Pb}(\text{Zr}, \text{Ti})\text{O}_3$)

The piezoelectric materials of greatest interest are ferroelectric ceramics based on Pb-containing perovskites, for example $\text{Pb}(\text{Zr}, \text{Ti})\text{O}_3$ (PZT). They offer a high piezoelectric constant, and diverse chemical modifications allow one to tailor the properties¹¹². The application of PZT thick films in microelectromechanical systems (MEMS), e.g. as micro-actuators¹¹³ or for energy harvesting¹¹⁴, is a major research topic. More than 60 publications emphasize the interest in fabricating PZT films by AD.

Early investigations in 1999 by Akedo and Lebedev showed that the piezoelectric properties of AD films depend on post-deposition annealing⁵. With a remanent polarization $P_r < 5 \mu\text{C/cm}^2$ and a coercive field $E_c < 5 \text{ kV/cm}$ in the as-deposited state, it was increased up to $35 \mu\text{C/cm}^2$ and 47 kV/cm by annealing at 800 °C (Fig. 17). This improvement was attributed to crystal growth after deposi-

tion that occurred during annealing⁵. Further studies indicated that the remanent polarization could be increased to $40 \mu\text{C}/\text{cm}^2$ ¹¹⁵, and the dielectric constant to 2000¹¹⁶.

Based on Akedo's work, many studies also recognized the importance of post-deposition annealing^{5,78,81,113,115–133} and reported a relationship between grain size and electrical properties of PZT films (comparable to the properties of BaTiO_3 films shown in Section 4.3). At a grain size below $0.1 \mu\text{m}$, no 90° domain walls were observed, resulting in decreased electromechanical properties¹³⁴. Nakada *et al.* also reported on the domain wall motion inside AD films using PbTiO_3 powder¹²⁸. They assume that the deposition mechanism causes a uniform strain in the film plane resulting in crystal lattice distortion and defects in the crystal grains. This may suppress the domain wall motion leading to a smaller dielectric response. Through annealing the dielectric properties improve, which indicates Debye relaxation due to domain wall motion and the recovery from crystal lattice distortions and defects in the crystal grains.

Annealing can be accomplished either in an electric furnace or by means of laser irradiation^{117,130}, but temperatures of at least 600°C have been needed for adequate piezoelectric properties. In order to lower this annealing temperature, the influence of film irradiation with a fast

atom beam (FAB) generating a plasma between nozzle and substrate or using a plasma inside the aerosol transportation tube was investigated¹³⁵. The remanent polarization was two times higher, the dielectric permittivity was improved by 25–45% using both FAB and plasma for the as-deposited layers and layers annealed only at 400°C . The authors suggest that the enhanced ferroelectric properties are caused by a reduction of defects and contamination inside the film. O_2 -FAB mainly reduces the number of oxygen vacancies on the surface of primary particles and deposited layers, which is indicated by a change of the color of the as-deposited layers from black to yellow. Such an improvement was not observed with Ar-FAB. With both FAB and plasma irradiation, the post-processing temperature could be reduced to below 500°C , which was sufficient to obtain enhanced ferroelectric and piezoelectric properties.

Besides an adequate pre-processing of the starting powder^{71,120}, as already described in Section 3.4, the variation of the carrier gas and its mass flow is another way to influence the piezoelectric properties. Helium carrier gas-deposited samples showed slightly better piezoelectric properties than N_2 -deposited ones. For both carrier gases, the spontaneous and the remanent polarization decreased while the coercive field increased.

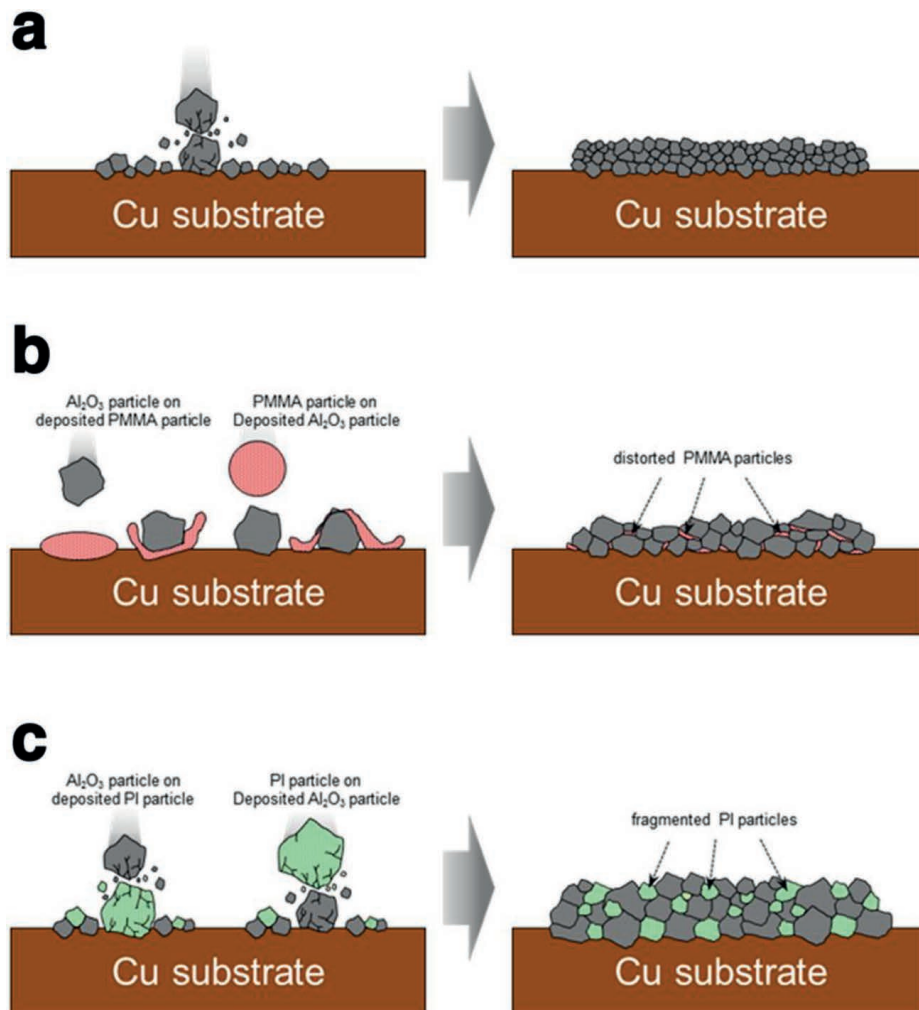


Fig. 16: The influence of polymer admixtures on the aerosol deposition of Al_2O_3 . (a) Typical AD Al_2O_3 films formed by impact consolidation. (b) PMMA particles distorted by Al_2O_3 particles. (c) PI particles fragmented by Al_2O_3 particles (from⁸⁸).

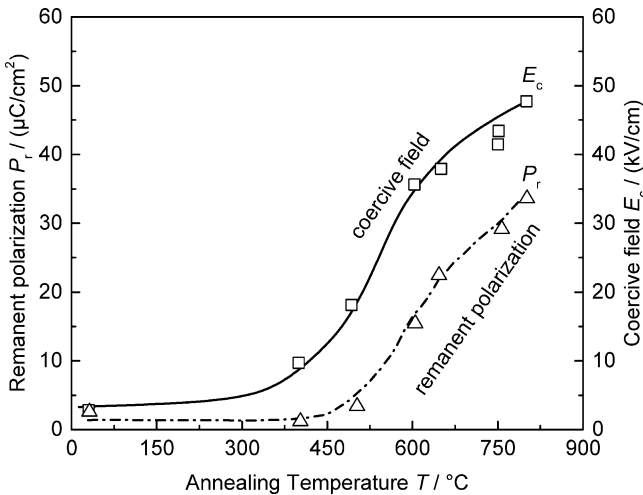


Fig. 17: Evolution of remanent polarization P_r and coercive field E_c with annealing (after ⁵).

Akedo fabricated PZT-AD films of high density (over 95 % relative density) with good transparency ³². Transparent films with an optical transmittance (T) up to 80 % (from 500 nm to 800 nm wavelength) have been reported ^{35, 71, 78, 118, 124, 136, 137}. There appears to be a strong dependence of T on the carrier gas used for deposition ¹³¹: With He gas, $T = 25\%$. Whereas with N_2 , O_2 , or air, $T > 60\%$ (all transmittance values between 500 nm and 800 nm wavelength measured on 2- μm -thick films). Highly transparent films of PZT ^{35, 118} and lanthanum-modified PZT (PLZT) ^{138–141} demonstrated electro-optical activity (refractive index change with applied electrical field).

A few perovskite solid solutions have been prepared by means of AD, including relaxor ferroelectrics, $\text{Pb}(\text{Ni}, \text{Nb})\text{O}_3\text{-PZT}$ ^{116, 125, 142} and $\text{Pb}(\text{Zn}, \text{Nb})\text{O}_3\text{-PZT}$ ^{74, 126, 133, 143}. Another aim of PZT composite films is the reduction of the residual stress inside the deposited films. As already described, an additional annealing of the as-deposited film is necessary in order to obtain good piezoelectric properties. Depending on the substrate used for deposition, a thermal expansion mismatch of the PZT film and the substrate material may cause the film to crack or delaminate from the substrate. By depositing a mixture of PZT and polyvinylidene fluoride (PVDF) the residual stress can be reduced ^{81, 132}. In the annealing step after deposition, the PVDF phase was burned and uniformly dispersed sub-micrometer pores capable of relaxing the residual stress were generated. This lowers the relative permittivity of the film with increasing PVDF content but the piezoelectric d_{33} coefficient was preserved (250 pC/N adding 3 % PVDF; 56 pC/N adding 10 % PVDF). It is also possible to use an excess-PbO powder to reduce the residual stress inside the deposited layers ¹³³. The residual compressive stress of the films containing 2 % excess-PbO before and after post-annealing at 900 °C was measured using high-resolution XRD and it was found to decrease from 190 to 160 MPa after the annealing process. This effect is assumed to be related to PbO evaporation building elastic pores and thus influencing the residual stress.

PZT-gold composite films were produced in order to influence the optical properties and produce colorful transparent nano-composite films. Mixtures from 0.0015 to

0.045 wt% gold affected the transmittance of the films at designated wavelengths ¹²². Improved surface plasmon resonance (SPR) properties were achieved by adding less than 1 wt% gold. The SPR wavelength position can be controlled by adjusting the permittivity of the PZT matrix by annealing ⁷⁸.

AD PZT and related films have potential for use in MEMS devices, such as in energy harvesting (generators) ^{18, 114, 144}, micro-actuators ^{145–147}, optical micro scanners ^{113, 119, 148, 149} or metal-based optical resonant scanners ¹⁵⁰. Freestanding membranes for the use as micropumps or micromixers ¹²¹ have also been reported. Proposed electro-optic applications include modulators ^{35, 138, 141} like a Mach-Zehnder Interferometer, on-chip optical interconnections ¹³⁹ and an ultra-small electro-optical field probe on top of an optical fiber edge ¹³⁷.

(3) Barium titanate (BaTiO_3)

Barium titanate is the prototypic ferroelectric ceramic with simple perovskite structure. Owing to the high permittivity (up to values of 10 000), it is the most widely used dielectric in multilayer ceramic capacitors (although not in its pure form) ⁹⁹. More than 30 publications about AD BaTiO_3 demonstrate that it is a material of interest. AD-processed BaTiO_3 can be dense with high purity ¹⁵¹, and several studies have proved its suitability for use as thick film ¹⁵² and embedded capacitors ^{153, 154}. Others demonstrated that it can be deposited on LTCC substrates ¹⁵⁵ and on flexible metal substrates for use in flexible electronics ¹⁵⁶. Further potential applications are in microelectronic packaging ¹⁵⁷ and electronic devices via micropatterning ¹⁵⁸.

As known for many years, the permittivity of BaTiO_3 depends on the grain size of the ceramics. It shows a maximum in the range of about 1 μm and strongly decreases with decreasing grain size as shown in Fig. 18 ^{134, 159, 160}.

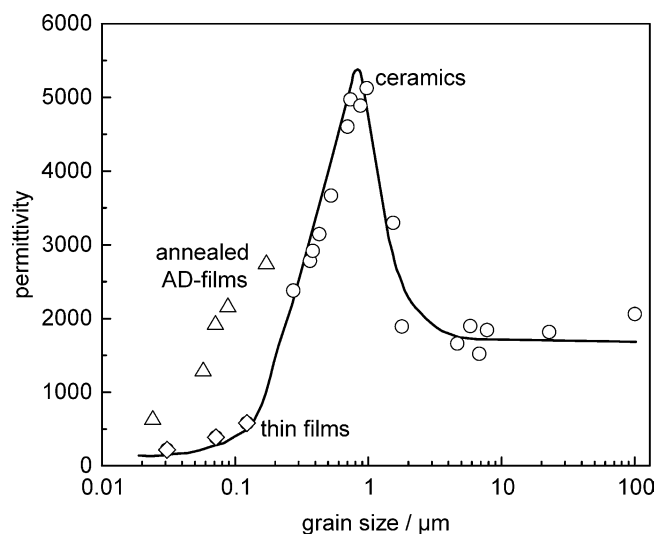


Fig. 18: Grain size dependence of the relative permittivity of BaTiO_3 , after ^{134, 159, 160}.

Grain size and residual stress also influence the permittivity of AD BaTiO_3 . AD films prepared by Hoshina *et al.* ¹⁵⁹ showed very small crystallite sizes in the range of

20 nm after deposition. Dielectric measurements on annealed films showed an increase of the relative permittivity with increasing grain size from 680 (24 nm) up to 2800 (170 nm)¹⁵⁹ (Fig. 18). Other papers describe the influence of post-deposition annealing on the relative permittivity of AD films^{41,103,159,161}. Compared to values of the permittivity from Arlt *et al.*¹⁶⁰, the AD films seem to have a higher permittivity than conventional thin films with comparable grain size. This has not been fully explained, and should be considered for future investigations.

AD BaTiO₃/PTFE composites have been prepared with low PTFE content (0.1 wt%)⁸⁷. This resulted in an increase of the grain size inside the deposited film, but the relative permittivity of composite films was very low.

Many investigations regarding the dielectric properties revealed problems of high leakage currents through the deposited films^{41,152–154,156,162–165}. Oh *et al.* found the leakage current rose strongly for film thicknesses below 1 μm^{162,165}. They attributed this to a change in the leakage current mechanism. Microscopic defects like porosity and not fully crushed particles inside the film are presumed to be the origin for this negative effect. These defects may result from agglomerates in the aerosol that got fractured while impacting on the substrate but did not have enough energy to form a dense ceramic layer. Oh *et al.* also showed that the non-uniform electric-field concentration at the rough interfaces between the BaTiO₃ films and the metal substrates influence the leakage current at high electric fields^{162,165}.

(4) Titanium Dioxide (TiO₂)

Titanium dioxide, also called titania (TiO₂), is a non-toxic, inexpensive ceramic material with a wide range of applications. TiO₂, primarily used in one of two major crystalline polymorphs (rutile or anatase), features good chemical and thermal stability, a good transparency in the range of visible light¹⁶⁶ together with a high refractive index of 2.5 to 2.7⁹⁹. It provides a high permittivity of 80 at room temperature¹⁶⁷ and intrinsic n-type semiconducting properties with a large band gap of over 3 eV¹⁶⁷. Its photoelectrochemical¹⁶⁸ and photocatalytic conversion capabilities¹⁶⁹ are highly application-relevant. Porous titania films show a great potential for the use in dye-sensitized solar cells or in devices to purify waste water, due to its antibacterial and photo-degradation abilities.

Aerosol deposition of TiO₂ films has been described in more than 30 publications. Physical properties like electrical conductivity, microhardness and wetting behavior have been reported. Park *et al.* examined the wettability of AD titania films and the influence of different post-treatment procedures^{170–172}. As-deposited thick films show hydrophobic behavior with a water contact angle of about 30°, which is also caused by the rough honeycomb structured film surface. A post-treatment by means of CF₄ plasma etching could decrease the contact angle with increasing etching time to about 5° after 10 min¹⁷⁰, as a result of an incorporation of fluorine in the film surface. Very thin AD films with thicknesses between 60 and 200 nm were treated with UV light (wavelength 365 nm) for up to 5 h¹⁷¹, also resulting in a decrease in the contact angle to almost 0. Here, AD films exhibit an advantage over con-

ventional dip-coated films, which retain much higher contact angles. By a suitable heat treatment of AD TiO₂ thin films (150 nm thickness), superhydrophilicity (contact angle nearly 0°) can eventually be achieved without any further surface modification (Fig. 19)¹⁷².

This can be explained by combined effects of a change in surface microstructure, roughness and crystal structure. With annealing up to 500 °C, the surface tends to form a meso-porous morphology, also visible from a slightly roughening from $R_a = 3.5$ nm to $R_a = 4.9$ nm. Additionally, a phase change takes place and up to 30 % of anatase/rutile are converted to the highly hydrophilic brookite phase. Superhydrophilic films can be used to enable anti-fogging and self-cleaning behavior for windows and mirrors. Fan *et al.* studied the starting powder influence on the micro hardness and morphology of titania films⁷. They observed denser films when they used smaller particles with only 20 nm in size instead of 200 nm. Films produced with 200 nm particles also showed a low micro hardness of 235 HV, much smaller than typical sintered bulk samples (Knoop hardness 713–1121 kg/mm²¹⁰⁰, corresponding to 675 HV and above), and therefore only a weak bonding between the nanoparticles was suggested.

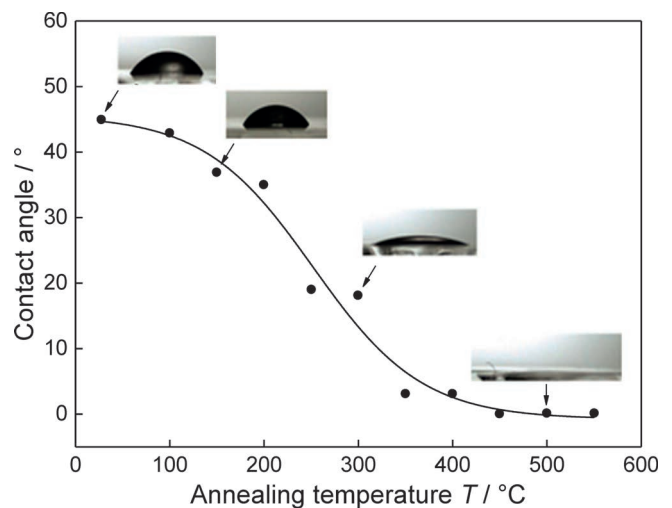


Fig. 19: Relationship between the water contact angle and annealing temperature. Adapted with permission from¹⁷². Copyright (2014) American Chemical Society.

AD titania films exhibit typical semiconducting behavior. Sahner *et al.* observed a p- to n-type change with increasing temperature and decreasing oxygen partial pressure¹⁷³, in accordance with literature. Within the measured temperature range of 750 to 970 °C, the semiconductor was close to its intrinsic conductivity minimum and therefore only a shallow oxygen dependency was detected. Local annealing by means of laser irradiation¹⁷⁴ was proven to improve the electrical conductivity by over two orders of magnitude. Local temperatures between 800 °C and 1400 °C induced the formation of oxygen vacancies, resulting in a decrease in resistance and a change to a gray color¹⁷⁵, whereas higher temperatures destroyed the films.

Possible applications of titania films are mainly based on its photocatalytic activity under UV irradiation. For that

purpose, porous film structures are of high importance, in contrast to other AD films where dense films are preferred. The overall surface area of films increases with higher values of porosity, adding additional adsorption sites and therefore enhancing the photocatalytic conversion capabilities. Kim *et al.* described the general suitability of TiO₂ coatings produced by AD for waste water treatment¹⁷⁶. Yang *et al.* firstly proved the successful decomposition of organic pollutants (phenol) in aqueous solutions by AD TiO₂ films under UV irradiation⁸⁹. The photocatalytic conversion performance was significantly improved by inducing porosity within the film, achieved by an aerosol co-deposition of TiO₂ and polymeric polyethylene glycol (PEG) followed by subsequent removal of PEG by annealing. Annealing temperatures of 450 to 500 °C resulted in highest photocatalytic activities owing to the largest porosity, combined with best adhesion to the substrate. Instead of PEG, also β-tricalcium phosphate (TCP) could be used to generate porosity⁹³. Amounts of 10 to 45 wt% TCP were added to the TiO₂ powder and sprayed to composite films. Subsequently, TCP was leached out by HCl, leaving a porous film behind. Higher amounts of TCP lead to more porosity and to stronger photocatalytic activities owing to improved adsorption effects. Park *et al.* highlighted the antibacterial properties of AD TiO₂ films^{43,47}, with a nearly complete removal (“photokilling”) of *E. coli* germs from the specimen after only 1 hour of UV radiation. Also a complete decolorization of methylene blue was observed in less than 2 h under UV exposure. Solar light could be used as well (instead of UV), showing a slower conversion rate, but clearly demonstrating the capabilities. TiO₂ films were suggested as cost-effective photocatalysts in applications for purification of contaminated air or water, pathogen inactivation and self-cleaning ceramic tiles.

A second application field for titania AD films are dye-sensitized solar cells (DSSC). These cells are based on a semiconducting material located between a photo-sensitized anode and a dye in contact with an electrolyte. Grätzel and O’Regan¹⁶⁸ invented the modern type of this solar cell, therefore it is also referred to as the Grätzel cell. DSSC are considered a low-cost way to convert solar to electric energy, since inexpensive materials and production processes can be applied. As with photocatalytic applications, a porous film is highly favorable. This porosity is used to infiltrate the necessary light-absorbing dye. The dark-purple-colored Ruthenium-based dye Ruthenium 535-bisTBA is most common to investigate the photoelectrochemical effect in AD titania films^{89,177}. Films are typically prepared on indium or fluorine-doped tin-oxide (ITO/FTO)-coated glass substrates as electrodes.

Different ways to induce porosity in titania films were investigated. Fan *et al.* showed that the performance of a DSSC can be enhanced by increasing the film porosity using aerosol co-deposition AcD⁷⁹. The porosity is again controlled by different amounts of polymeric PEG, which were embedded in the composite film as volatile component. Annealing at 450 °C completely removed PEG and led to 41 % porosity. Devices with these porous films ex-

hibited short circuit current densities up to 145 A/m² and a conversion efficiency of 7.1 %, while non-porous ones only achieved 90 A/m² and 5.1 %, respectively. Porous films without any binder were produced by Cho *et al.*¹⁷⁷ by means of aerosol deposition of titania powder mixtures consisting of small and large-diameter particles (25 nm and 700 nm). Very small particles prevent the formation of fully dense films owing to a lack of momentum required to enable the RTIC mechanism. Nevertheless, a good connection between smaller and larger particles through necking was observed, which facilitates the transport of electrons. A subsequent heat treatment at 450 °C improves necking and increases the short circuit current densities by raising the number of electron paths. Yang *et al.* achieved film porosities between 43 % and 50 % by spraying a so-called strengthened powder²⁰. This contains 0.5–3 μm-sized porous particles which were prepared from 25 nm particles by mixing with PEG, followed by annealing at 450 °C, hydrolysis with TiCl₄, and final sintering at 500 °C. The AD films featured a bimodal pore size distribution with two peaks at 15 and 50 nm, while 25 nm particles generated a unimodal distribution with an average pore size of 17 nm³³. This bimodal pore size distribution improves the dye infiltration together with the ion diffusion coefficient, leading to higher photovoltages.

A different attempt to enhance the efficiency in DSSC devices is to introduce a dense titania blocking layer between electrode and porous film (Fig. 20).

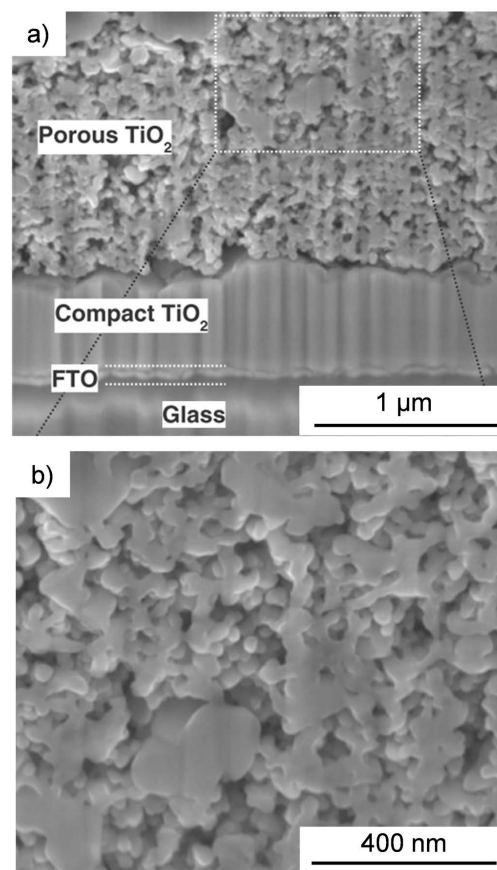


Fig. 20: Cross-sectional SEM image of a dye-sensitized solar cell prepared by focused ion beam. a) cell with porous AD TiO₂ for dye infiltration and compact AD TiO₂ film as blocking layer b) porous AD TiO₂ (high magnification). Reprinted from¹⁷⁷ with permission from Elsevier.

The dense layer suppresses unwanted electron recombination in indirect routes between FTO and electrolyte¹⁷⁷. Heo *et al.* stated that an only 46-nm-sized titania AD film drastically improves the efficiency of the DSSC from 3.3 to 5.6 %, whereas thicker films above 70 nm negatively influence the overall efficiency owing to a lower transmittance and an increased electrical resistance¹⁷⁸. Kim *et al.* intended to decrease the recombination rate by increasing the conductivity of titania by means of the addition of varying amounts of graphene⁸³. 0.3 wt.% graphene increased the efficiency from 3.1 to 5.0 %, also caused by favoring the formation of photogenerated electron-hole pairs. More graphene reduces the efficiency owing to higher absorption of light, therefore reducing the generation of electron-hole-pairs and photoexcited electrons.

Additional applications for AD titania films include corrosion-resistant layers on metals like magnesium¹⁷⁹ or as photoelectrodes for the environmentally friendly hydrogen production based on photoelectrochemical solar water splitting¹⁸⁰.

(5) Surface protection coatings

For passivation of metallic surfaces in low-temperature applications, many low cost techniques exist such as spray painting, anodizing, etc. Typically, substrates (like metals) suffer from oxidation at high temperatures. As shown for a Cu substrate, a 1- μm -thick dense coating of Al_2O_3 can prevent the coated area from oxidation damage (testing temperature 400 °C) (see Fig. 21). With high hardness, good chemical and temperature stability, passivating ceramics like AlN, TiN, Al_2O_3 , TiO_2 , and Y_2O_3 , etc. are successfully used to prevent underlying materials from degradation by wear, corrosion or temperature influence. Since dense and μm -thick films can be fabricated with AD at high deposition rates, it has an advantage over other coating techniques especially in this field of application.

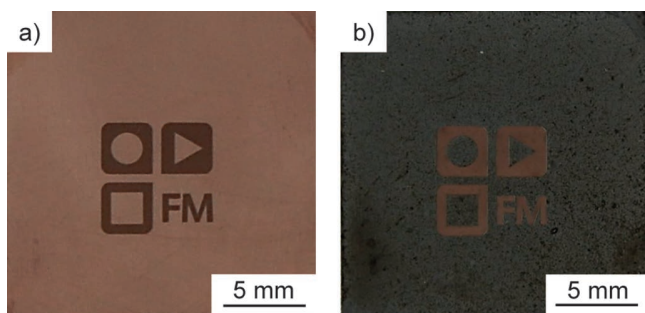


Fig. 21: Demonstration of corrosion protection effect of Al_2O_3 films prepared by AD-mask-deposition on Cu substrate (a) as-deposited and (b) after temperature treatment at 400 °C in air. Courtesy of Dept. of Functional Materials, University of Bayreuth.

Oxidation of metallic surfaces is probably the most common reason for materials degradation, and thus a potential application field for AD coatings. As further discussed in Section 4.9, numerous studies deal with oxidation problems of metallic interconnects in SOFC^{98, 181–185}. The high temperature may lead to Cr-diffusion and formation of low-conductive interlayers. This is reduced by using AD diffusion barrier coatings of stable and highly conductive materials. Plasma etching is a highly corrosive technique and frequently used in semiconductor fabrication.

Coating of influenced parts can be very helpful to diminish contamination of products⁶². Y_2O_3 and other rare earth oxides show an enhanced stability against plasma erosion¹⁸⁶. Deposition behavior of different rare earth oxides on different metal substrates was investigated⁶¹. Compared to conventionally employed alumina from plasma spraying, Jung *et al.* showed a significantly smaller erosion rate of rare earth oxide AD films by a $\text{CF}_4 + \text{Ar}$ plasma along with an enhanced electric breakdown strength¹⁸⁶.

Other examples of applications of AD films for surface protection are reported in the literature. Piechowiak *et al.*¹⁵ achieved AD coatings of Ti_3SiC_2 with thicknesses over 15 μm . This MAX-phase material shows excellent thermal shock behavior up to high temperatures as well as good chemical stability and mechanical properties. Attempts to improve abrasion resistance of films have been made using AcD with powder composites where the major component is blended with a very hard material like e.g. diamond powder^{17, 104}. As one step toward this goal, Charles *et al.*¹⁷ investigated deposition behavior of mixtures of soft ZnS and diamond powder. They found good film formation for low amounts of diamond powder whereas contents > 50 % lead to abrasion. Mechanical tests concerning the mechanical strength of these composite films have not been shown¹⁷.

Seto *et al.*¹⁰¹ achieved the deposition of alumina on an aluminum roller, commonly used in industrial machines and processes. They showed impressively that AD of ceramic materials can be applied to more complex substrate structures and can cause a real improvement in terms of wear resistance. 5- μm -thick coatings of Al_2O_3 on test substrates showed superior wear resistance and chemical stability (see Fig. 22 and Fig. 23) compared to bare aluminum substrate and also to Cr-plated aluminum alloy substrates. This is expressed through a higher resistance against abrasion in a ball-on-disc wear test and salt spray testing with selectively damaged samples. Film adhesion, as well as hardness (in this case between 1100 HV and 1590 HV (10.8–15.6 GPa), play a key role for applications like this.

Further detailed studies about electrochemical corrosion properties of YSZ and TiO_2 coatings for different metal alloy substrates are conducted by Ryu *et al.*^{179, 187, 188}. Using acidic, basic and neutral solutions, they tested the chemical stability of substrate materials and films, asserting for each scenario an improved stability performance when the substrate was coated¹⁸⁷.

In principle, AD can be used for most applications involving exposure to harsh environmental conditions and highly corrosive processes. With its high deposition rate and the dense structure of its coatings, AD satisfies a need in current process technology for such applications.

(6) Biocomponents – hydroxyapatite

Hydroxyapatite (HA), $\text{Ca}_{10}(\text{PO}_4)_6(\text{OH})_2$, is the major mineral component of human bone. Synthetic HA, used as a surface coating on metallic implants, exhibits excellent biocompatibility, bioactivity and osteoconductivity resulting in a stimulation of bone growth between the interface of the implant and the natural bone tissue. To promote the osteogenesis, a rapid and stable fixation of the implant on the surrounding bone can be achieved^{189, 190}.

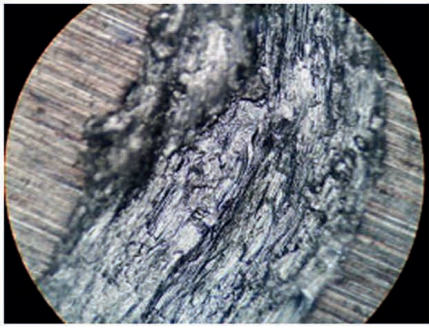
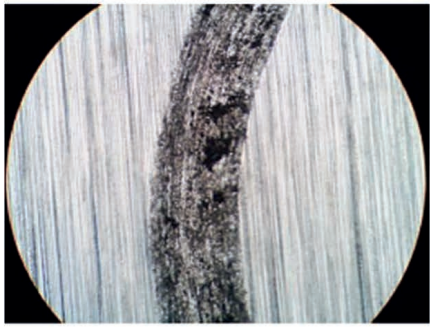
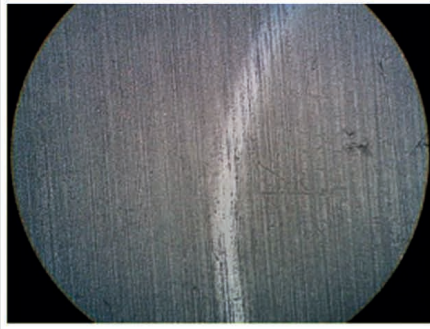
Aluminum alloy	Cr plating film	Al ₂ O ₃ film
		
Depth of wear test slot: 73.07 μm	Depth of wear test slot: 10.45 μm	Depth of wear test slot: 1.88 μm

Fig. 22: Result of wear test on samples of aluminum alloy, uncoated, with Cr plating and AD film of Al₂O₃ ¹⁰¹.

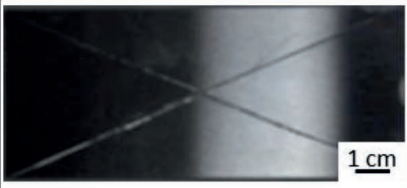

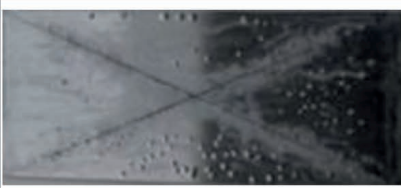



	0 cycles	5 cycles	15 cycles
Cr plating film			
Al ₂ O ₃ film			

Fig. 23: Neutral salt spray test on damaged Al₂O₃ and Cr plating films ¹⁰¹.

The currently prevailing coating method of HA for dental and orthopedic implants is plasma spraying. It exhibits several significant disadvantages. The high process temperatures lead to cracks in the films resulting in poor film quality and rapid degradation of the HA coating ¹⁸⁹. By employing the AD technique, the thermal stress on the coating can be circumvented, leading to economic, almost crack-free and dense HA films and presents new possibilities for the production of improved HA coatings.

Hahn *et al.* used the AD method to produce HA on titanium substrates and investigated the influence of crystallinity on the biocompatibility and osteogenic response of HA coatings ¹⁹¹. Commercially available HA powder was pretreated and deposited on the Ti substrates with a gas flow rate of 5 l/min. The coating indicated no cracks, pores or delamination and exhibited a density of 98.5 % of the theoretical density. The tensile adhesion strength between the coating and the titanium substrate was 30.5 MPa, being twice as high as demanded in the ISO 13779 – 2 for coatings of HA (15 MPa). XRD measurements revealed a grain size of 16 nm and amorphous regions for the as-deposited coating. Since the biocompatibility is affected by grain size, a heat treatment was conducted in order to adjust the grain sizes and to decrease the amorphous phase. Heating the film at 400 °C for 1 h increased the average grain size to 29 nm and eliminated the amorphous domains, thus significantly increasing the al-

kaline phosphatase (ALP) activity. Further heat treatment at 500 °C for 1 h led to grains of 100 nm size but reduced the ALP activity drastically (Fig. 24a).

The bone-calcium phosphate-coated implant bonding process can be improved by mixing less soluble HA with the more soluble β -tricalcium phosphate (β -TCP). The partial dissolution of the coating and formation of apatite on the coating surface leads to fast bonding of the implant to the bone. By applying the AD method (or more exactly AcD), the optimum ratio of pre-mixed HA/ β -TCP can be co-deposited and the biological performance of calcium phosphate coating can be enhanced ¹⁸⁹. It is reported that the biphasic coating of 30 % HA and 70 % β -TCP leads to the highest cellular response on titanium substrates. Films of a thickness of 2 μ m were both free of cracks and free of pores. The ALP activity of the investigated specimen is shown in Fig. 24b).

Si-doped HA ($\text{Ca}_{10}(\text{PO}_4)_{6-x}(\text{SiO}_4)_x(\text{OH})_{2-x}$) is reported to exhibit an increased bioactivity that leads to a higher cellular response than pure HA coatings ¹⁹². Hahn *et al.* employed the AD to fabricate dense Si-HA films on titanium metal exhibiting a high tension strength of 28 MPa. The AD films had a thickness of 5 μ m and the cell proliferation as well as the ALP activity was highest for 1.4 wt% Si-doped HA.

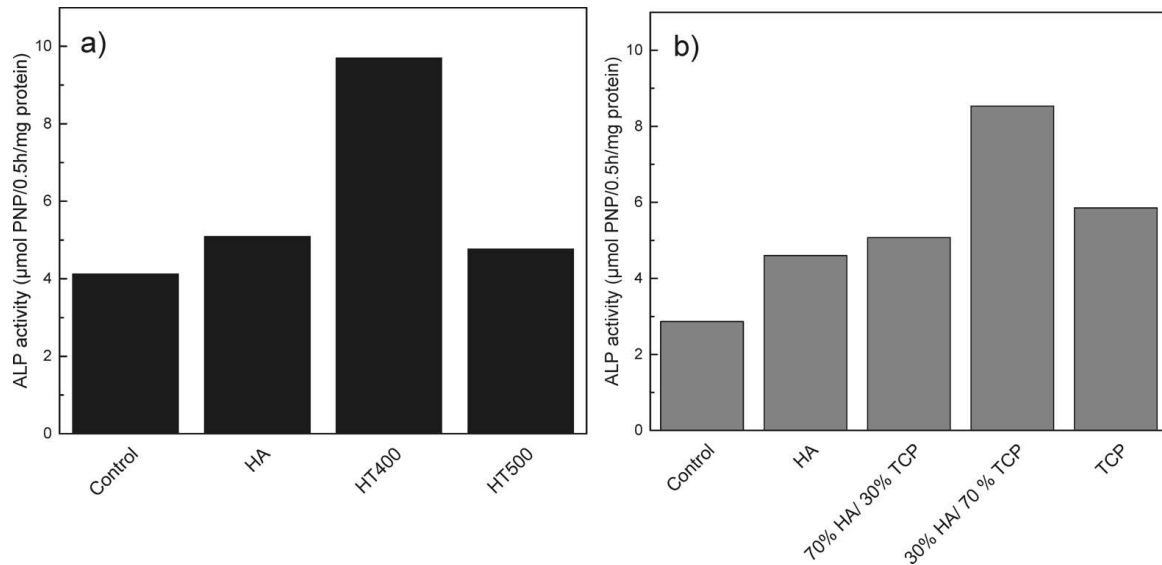


Fig. 24: ALP activity of MC3T3-E1 cells on control, HA, Heat treated HA at 400 °C (HT400) and 500 °C (HT500) (a) and the corresponding ALP activity of biphasic coatings of HA and TCP (b). Reprinted from ^{96, 191} with permission from John Wiley and Sons.

Fluorine doping of HA (FHA) was investigated as well. Being less soluble than pure HA, it exhibits a better long-term stability in a biological environment. The as-deposited fluorine doped HA (FHA) films had a high adhesion strength of 38 MPa on pure titanium and exhibited a homogenous film thickness of 5 μm. Owing to the improved dissolution resistance and good biocompatibility, the FHA coating with a composition of $\text{Ca}_{10}(\text{PO}_4)_6(\text{OH})\text{F}$ had both the highest ALP activity and the best cellular response ¹⁹³.

HA on biodegradable polymers is used as scaffold for bone tissue regeneration. Coated with HA, mainly poly-L-lactic acid (PLLA) is used due to its good osteoconductivity and biocompatibility. Kitajima *et al.* deposited HA on PLLA films with a rate of 25 μm/min followed by a heat treatment at 200 °C for 20 minutes to prevent the films from peeling off. Dense and pore-free HA films were successfully formed on PLLA substrates ¹⁹⁴. Other promising biodegradable materials are alloys of magnesium owing to their good biocompatibility and excellent biological performance, but their corrosion resistance towards body fluids is poor. By coating AZ31 Mg alloy with hydroxyapatite-chitosan composite using the AcD method, dense films without pores or cracks were produced and the corrosion resistance of AZ31 Mg was substantially enhanced ^{85, 194}.

Besides synthetic hydroxyapatite, xenogeneic (i.e. bone-derived) HA (XHA) can be deposited with AD method. Being of bovine origin, it is of almost unlimited availability at low cost and an alternative for artificial HA. Kim *et al.* used specially prepared xenogeneic HA to fabricate 1–2 μm thick and homogeneous films on $\text{Ti}_6\text{Al}_4\text{V}$ substrates, widely used for biomedical implants. XHA is also used when coating zirconia substrates. ZrO_2 inherently exhibits low bioactivity owing to its bioinertness, but has many advantages as a structural or dental implant because of its strength, toughness and wear resistance. Zirconia substrates were AD-coated with XHA and densely compacted HA films with a thickness of 1–2 μm, strongly bonded to the surface, were obtained. No delamination,

pores or microcracks were detected and the as-deposited films exhibited a tensile adhesion strength of 31 MPa. When immersed in simulated body fluids, the dissolution behavior of the AD-XHA coating was stable compared to standard plasma-sprayed HA coatings ^{16, 195}.

(7) Magnetic materials

AD can also be employed to prepare magnetic ceramics. Hereafter we describe two most commonly investigated materials, namely Sm-Fe-N, a rare-earth-based permanent magnet with a high coercive field and soft magnetic Ni-Zn-Cu ferrite film magnets with a low-coercive field, used as an electromagnetic wave absorber.

(a) Sm-Fe-N

When downsizing electromagnetic devices and motors, rare earth magnets play a decisive role. Even though there are various methods to fabricate thin magnetic films, their magnetic properties deteriorate owing to defects introduced in the surface area. Hence other deposition methods, like pulsed laser deposition (PLD) or sputtering are emerging methods to fabricate these thin magnetic films ¹⁹⁶. However, their deposition rates (1 μm/min) are too low to produce thin permanent magnets on large scale ¹⁹⁷.

Again, the AD method offers advantages of very dense films and high deposition rates ¹⁹⁷. Both Maki *et al.* ¹⁹⁸ and Sugimoto *et al.* ¹⁹⁶ investigated the influence of AD on the microstructure and the magnetic properties of Sm-Fe-N films. AD films with thicknesses up to 190 μm and a deposition speed of 16 μm/min were reported, exhibiting film densities of 5.43 to 6.24 g/cm³, (71–81 % of the theoretical density of $\text{Sm}_2\text{Fe}_{17}\text{N}_3$) ¹⁹⁷.

The magnetic properties were measured parallel and perpendicular to the AD films with a thickness of 77 μm deposited on SiO_2 substrates ¹⁹⁸. Compared to bulk powders, the remanence B_R of the AD films decreased from 0.62 T to 0.42 T, being only 68 % of the initial value. The saturation magnetization, J_s , of the films was determined at a magnetization of 2 T to be 0.75 T, which is 12.5 % low-

er than that of the host powder ($J_{s,host} = 0.8$ T)¹⁹⁹. These differences can be attributed to the lower density of the AD films or to oxidization effects. Concerning the measurement direction there was no distinctive difference observed between the measurement parallel and perpendicular to the film¹⁹⁶.

However, the coercive field H_{cJ} increased from 920 kA/m for the bulk material to 1340 kA/m perpendicular and 1420 kA/m parallel to the film respectively, which is an improvement by over 50%. It should be noted that these values are obtained by AD without any further heat treatment, in contrast to other methods mentioned above, like PLD or sputtering. The demagnetization curves of Sm-Fe-N bulk powder as well as AD films are shown in Fig. 25.

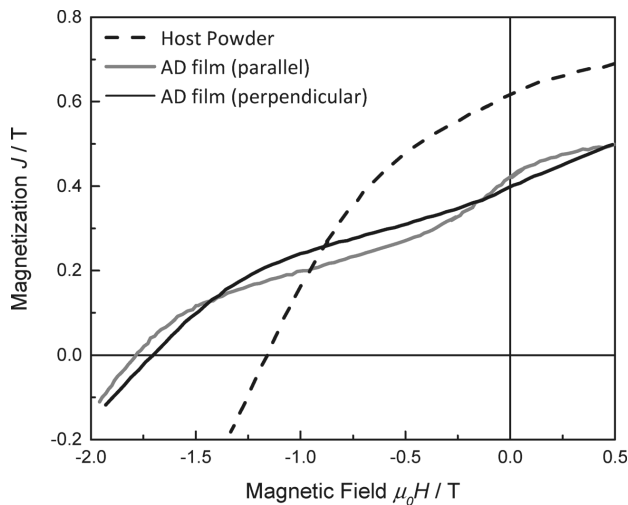


Fig. 25: Demagnetization curves of Sm-Fe-N films produced by AD compared to raw powder. Reprinted from¹⁹⁷ with permission from John Wiley and Sons.

SEM images were used to elucidate the microstructure of the AD films. Maki *et al.*¹⁹⁷ report average grain sizes of 1.94 μm for the raw powder, whereas the AD films exhibit an average grain size of 0.32 μm , which is very close to the single-domain grain size (0.3 μm) of $\text{Sm}_2\text{Fe}_{17}\text{N}_x$. Pinning of domain walls by grain boundaries, and lack of domain wall movement explains the high coercive fields¹⁹⁷.

Having applied an external magnetic field during the aerosol deposition, Sugimoto *et al.*²⁰⁰ reported improved magnetic properties of AD Sm-Fe-N films. When two Nd-Fe-B permanent magnets were placed facing each other parallel to the film plane, an external magnetic field up to 0.19 T was applied. There are also reports of employing the magnetic field perpendicular to the substrate, but no significant improvement in the magnetic properties of the AD films was observed²⁰⁰. Fig. 26 shows the demagnetization curves of aerosol deposited Sm-Fe-N with or without an external magnetic field of 0.19 T perpendicular to the AD layer.

While the coercivity H_{cJ} rises by only 5% from 1420 kA/m to 1480 kA/m, the remanence B_R augments distinctively from 0.42 T to 0.54 T, which is an increase of 29% compared to AD films deposited without an external magnetic field²⁰¹.

There have also been investigations on the influence of the deposition angle of the nozzle during the aerosol deposition. Although no improvements on the magnetic properties of Sm-Fe-N were reported, the surface roughness of

AD films decreased, when the deposition angle of the nozzle was increased by 45°⁶³.

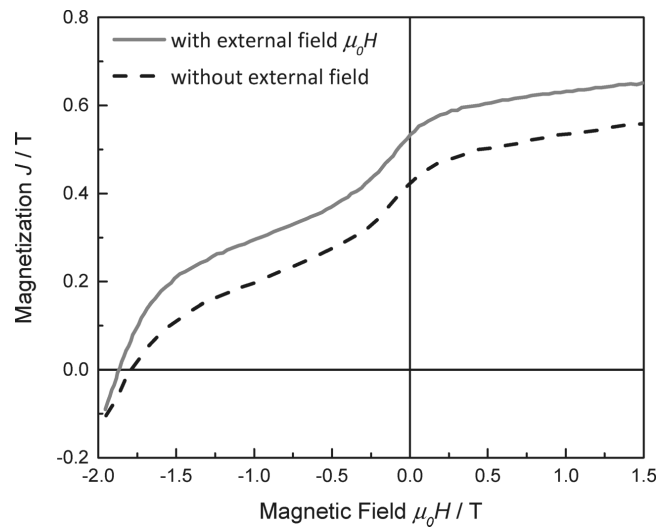


Fig. 26: Demagnetization curves of aerosol deposited Sm-Fe-N with or without an external magnetic field. Reprinted from²⁰¹ with permission from the Japan Institute of Metals and Materials.

(b) Ceramic ferrites

Soft magnetic ferrites such as $(\text{Ni,Zn,Cu})\text{Fe}_2\text{O}_4$ are used as high-frequency inductor cores and power supplies, where high magnetic permeability and remanence, and low coercive field, conductivity and magnetic loss are desirable. Ferrites are also used to suppress electromagnetic interferences (EMI), where both high real and imaginary permeabilities (μ_r' and μ_r'') are desirable. The increase of microwave radiation owing to the use of wireless communication tools, like cellular phones (0.9–2.6 GHz) or wireless LAN applications (2.45 GHz) demands suitable materials for miniaturized EM absorbers. Lebedev *et al.* employed AD to fabricate Ni-Zn-Cu ferrite films at a deposition rate of 2 $\mu\text{m}/\text{min}$, which is considerably higher than that of the commonly used techniques like CVD or PLD exhibiting a deposition rate of only 0.067 $\mu\text{m}/\text{min}$ ²⁰². Films of $(\text{Ni}_{0.4}\text{Zn}_{0.4}\text{Cu}_{0.2}\text{O})_{0.52}(\text{Fe}_2\text{O}_3)_{0.48}$ with a thickness of 6 μm were obtained. Owing to the small grain size of 20 nm and high internal strain of the as-deposited films, a temperature post-treatment was conducted at 800 °C for 5 minutes in air in order to relieve the stress and increase the grain size. With this post-treatment, the saturation magnetization of the annealed samples could be increased from 0.147 T to 0.3 T compared to the as-deposited films. However, the coercive field remained high ($H_c = 40$ kA/m) in contrast to the bulk material with $H_c = 4.7$ kA/m.

This behavior was circumvented by Kagotani *et al.* using different ferrite powder compositions²⁰³. While the deposition conditions remained the same as in²⁰², the magnetic properties of $\text{Ni}_{0.25}\text{Zn}_{0.65}\text{Cu}_{0.12}\text{Fe}_{0.98}\text{O}_4$ AD films were nearly equal to that of sintered ferrite samples after a heat treatment of about 1000 °C as can be seen in Fig. 27. Annealing of the films is again considered to decrease the distortion induced by the deposition process and therefore also decrease the anisotropy energy resulting in a reduced coercive field. While J_s and H_c are almost equal to the sintered specimen, the permeability μ_r doubled from 100 to 200 at a frequency of 10 MHz.

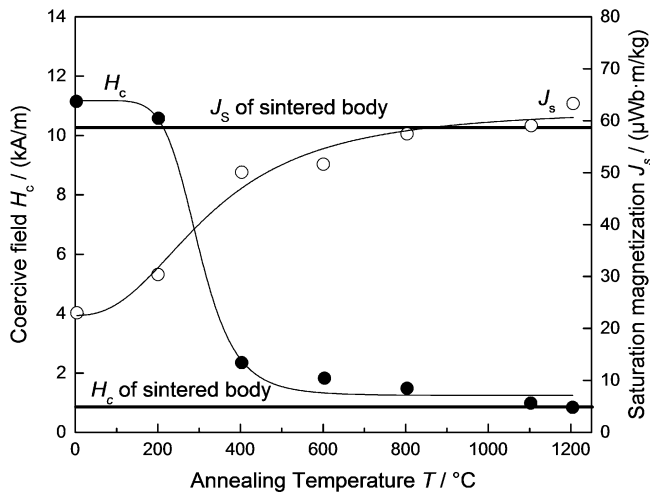


Fig. 27: Aerosol deposited nickel zinc ferrites: Dependence of saturation magnetization and coercive field on annealing temperature (after ²⁰³).

To avoid heat treatments, composite films using Fe and Ni-Zn-Cu ferrite powders were processed by means of AcD ^{204, 205}. Both ferrite and iron powders were mixed together and then deposited. While the coercive field did not change much, the saturation magnetization increased considerably with increasing Fe content ²⁰⁴. Furthermore, as-deposited films with high Fe content show a relatively high permeability comparable to the heat-treated Ni-Zn-Cu ferrite AD films. For a better process control in terms of Fe content in the AD films, Ni-Zn-Cu and Fe powder were co-deposited using two aerosol-chambers and double nozzles by Sugimoto *et al.* ⁷⁶. In this way, it was also possible to control the fabrication of stacked AD films in which the Fe content could be controlled. Multi-layer films were obtained with the ferrite layer exhibiting a thickness of 1 μm and the Fe layer 15 μm , respectively. Kim *et al.* succeeded in depositing Ni-Zn-Cu films on flexible PET sheets by mixing the ferrite raw-powder with PTFE powder. In this way uniform AD films with high thickness of 80 μm were obtained ⁹⁰.

(8) Materials for sensing applications

An increasing number of sensors is required in almost all application fields, like automation engineering, quality management, exhaust gas, and environmental measurement engineering ^{206, 207, 208}. This trend is increasing the demand for smaller and cheaper devices with enhanced accuracy. Aerosol deposition offers great potential to improve existing sensor devices, as well as to enable new, previously impossible or unthinkable designs ⁶. The general suitability of AD films for sensing applications has already been proven for gas sensors and pyroelectric sensors.

Sahner *et al.* used dense films of heavily iron-doped strontium titanate ($\text{SrTi}_{0.7}\text{Fe}_{0.3}\text{O}_{3-\delta}$, STF) as oxygen and propane sensors ¹⁷³. The electrical resistance of the semi-conducting STF ceramics served as the sensor signal. All measured samples exhibited the typical increase in resistance with decreasing oxygen partial pressure (p_{O_2}) and maintained their temperature-independent resistance in the range from 700 to 800 °C, which is in good agreement with published bulk data. Furthermore, the same sensor is able to quantify propane concentration in the range

of 200 to 2500 ppm when operated at the low temperature of 400 °C. The sensor signal was heavily affected by the film thickness, leading to a much higher resistance change and therefore sensitivity for lower film thicknesses around 3 μm . The authors emphasized the greatly simplified film preparation with the AD technique compared to conventional screen printing followed by sintering. With elimination of the sintering process, the formerly required SrAl_2O_4 diffusion barrier layer, which prevented the reaction with the substrate at high firing temperatures, is no longer required. In addition, STF AD films feature increased adhesion and strength. Bektas *et al.* conducted similar experiments on dense, semi-conducting tantalum-doped barium ferrate ($\text{BaFe}_{0.7}\text{Ta}_{0.3}\text{O}_{3-\delta}$, BFT) AD films ²⁰⁹, achieving an even wider temperature range with a temperature-independent response to p_{O_2} from 700 to 900 °C. While the resistance was nearly unaffected by usual exhaust gas components (like NO, NO₂, CO, CO₂, H₂O, C₃H₈) at 800 °C, a particular selective response to the NO concentration in the range from 1.5 to 2000 ppm becomes dominant at temperatures between 350 and 400 °C. Consequently, an application in air quality monitoring at 400 °C and under constant oxygen concentrations was suggested.

In contrast to the dense AD sensor films in ¹⁷³ and ²⁰⁹, Hsiao *et al.* investigated gas-sensitive films of zinc oxide (ZnO) with a porous structure produced by AD ²¹⁰. Porosity was intended to improve the gas-sensing characteristics by increasing the surface-to-volume ratio of the film. The porous film morphology is probably a result of the low carrier gas flow of 3 l/min, which led to reduced particle velocities and therefore inhibited the typical RTIC mechanism. After deposition, films were annealed by means of laser radiation to modify the film surface. Within the operating temperature range from 110 to 180 °C, carbon monoxide (CO) concentrations between 100 and 1000 ppm were measured. The system showed the highest sensitivity at shortest response time to CO at a temperature of 180 °C.

Aerosol deposition was also successfully applied for different negative temperature coefficient (NTC) thermistor materials. The resistance R of NTC materials rapidly decreases with increasing temperature, following the equation $R = A \exp(B/T)$. A is a constant, T the temperature in Kelvin and B the thermistor constant, acting as a measure for the temperature sensitivity of the material. NTC materials ²¹¹ exhibit a suitable behavior for temperature sensors or IR detectors like microbolometers or pyroelectric detectors. Ryu *et al.* investigated the aerosol deposition of NiMn_2O_4 and the NTC properties of resulting films ^{212, 213}. The resistance, R , of the films showed the typical exponential power-law behavior, with a thermistor constant B above 3900 K, being significantly higher than those of screen-printed films. Annealing up to 700 °C lead to a decrease in both, the total resistance R and the thermistor constant B . With the addition of Co and Fe as dopants ²¹⁴, the constant B could be enhanced up to over 5600 K. Ryu *et al.* concluded, that AD films of NiMn_2O_4 might be applicable in temperature-sensing and related applications. Hsiao ²¹⁵ proposed a sensor layout using AD ZnO films on $\text{Si}_3\text{N}_4/\text{Si}$ substrates with Au/Cr electrodes.

A single AD ZnO film was already able to detect radiation from an IR laser with modulated frequencies, but only at a single frequency band. A multi-frequency band pyroelectric sensor was successfully achieved by combining two ZnO films on the same bottom electrode: A 20- μm -thick AD film and a 1 μm RF magnetron sputtered layer. The thinner layer with a small thermal capacity is able to detect higher frequencies, while the noticeably thicker AD film measures smaller frequencies owing to its large thermal capacity. This suggested layout could therefore cover the sensing frequency band from 4 to 40 kHz with fast response.

Aerosol-deposited PZT films were investigated for application in magneto-electric devices^{143,216} by combining ferromagnetic/magnetostrictive and ferroelectric/piezoelectric phases. With the application of an external magnetic field, the mechanical deformation in the magnetostrictive phase was transferred to the piezoelectric phase through elastic coupling, resulting in a piezo-induced voltage. Furthermore, AD PZT films have been reported as sensing components in a tactile sensor device or as piezoelectric resonators in acoustic-wave mass sensors⁸¹.

(9) Fuel cell materials and applications

Solid oxide fuel cells (SOFC) are widely studied, since they are expected to become a competitive technology for future stationary and distributed power generation. The operating temperature is generally in the range between 800 and 1000 °C, which offers the advantage of reforming; thus the fuel cell is not limited to hydrogen, but can utilize a variety of (fossil) fuels²¹⁷. However, high-temperature processes are subject to material degradation, ageing and thermal expansion-contraction mismatch of components such as metallic interconnects. Therefore, there is a desire to lower operation temperatures to the intermediate (IT-SOFC) temperature regime (500–800 °C)²¹⁷. This in turn leads to the need for ceramic electrolytes with enhanced ionic (protonic or oxygen ionic) conductivity at lower temperatures in order to reduce ohmic losses. This could also be achieved with thinner electrolyte films in the SOFC, as long as the films can be kept dense, gas-tight and stable, which are the basic requirements for operation.

Most coating processes lack the ability to produce such films for SOFCs or cannot be scaled up to large areas, but the AD method offers promise for both dense electrolyte and also porous electrodes. Another advantage of AD is the low process temperature. For conventional fabrication of SOFCs, high temperatures above 1000 °C are needed to co-sinter the individual components, anode, electrolyte, and cathode, to a stable and gas-tight package²¹⁸. AD can be used to fabricate dense films at room temperature, although a modest annealing step is usually necessary to achieve acceptable electrical properties.

Only one paper was found concerning proton-conducting electrolyte films fabricated by means of AD²¹⁹. Most studies are about oxygen ion conductors such as yttrium- and scandium-stabilized zirconia (YSZ and ScSZ, respectively)^{28,220,221}, lanthanum strontium gallate magnesite (La,Sr)(Ga,Mg)O₃ (LSGM)^{21,222} and gadolinium- and samarium-doped ceria (GDC and SDC, respectively)^{19,223}. Hatano *et al.*²⁸ aerosol-deposited ScSZ on a

porous ceramic substrate and made dense 8 μm -thick films. Gas tightness was proved in a N₂ leak test. Choi *et al.*²²¹ deposited dense, 7.5 μm -thick YSZ films on a porous NiO-YSZ substrate. After annealing up to 1000 °C in air, the YSZ film showed no gas leakage, and the maximum power density (MPD) of the cell with AD-YSZ electrolyte and LSCF cathode was improved. Beyond the temperature of 1000 °C, annealing in air was found to increase the porosity resulting in leakage of the electrolyte film, whereas annealing at 1200 °C in reducing gas did not affect the density.

Besides degradation owing to pore formation, another serious ageing mechanism is the formation of low-conductivity interlayers between components as a result of diffusion²²². Annealing temperatures of 1200 °C and higher, which can be necessary for electrolyte fabrication, can cause severe cell degradation as a result of Ni diffusion from anode into the LSGMC electrolyte and formation of electronically conductive LaNiO₃. Again, AD at room temperature can avoid this problem. Since the aerosol-deposited crystallite size is usually less than 100 nm, annealing at a modest temperature helps to increase crystallite size and reduce electrolyte resistance. In addition, by building an AD buffer-layer, Choi *et al.*²⁷ improved degradation stability of the electrolyte-cathode interface.

Several studies are dedicated to counteracting degradation of the metallic (e.g. steel) interconnects caused by oxidation at higher temperatures^{28,181,183–185}, which causes an increase in resistance attributed to the formation and growth of a low conductivity Cr-rich interlayer. Choi *et al.*^{181,185} compared conventional steel interconnects with different AD-coated samples in respect of the rise of the area-specific resistance (ASR) while testing the long-term stability of interconnects (Fig. 28). As can be seen, all samples show an increase of ASR with oxidation time, but the degradation of the e.g. MnCo₂O₄-coated sample was delayed with six times lower ASR after ten times the aging time (1000 h). Even better results were obtained with AD protection films of (La_{0.8}Sr_{0.2})MnO₃ and LaNiO₃.

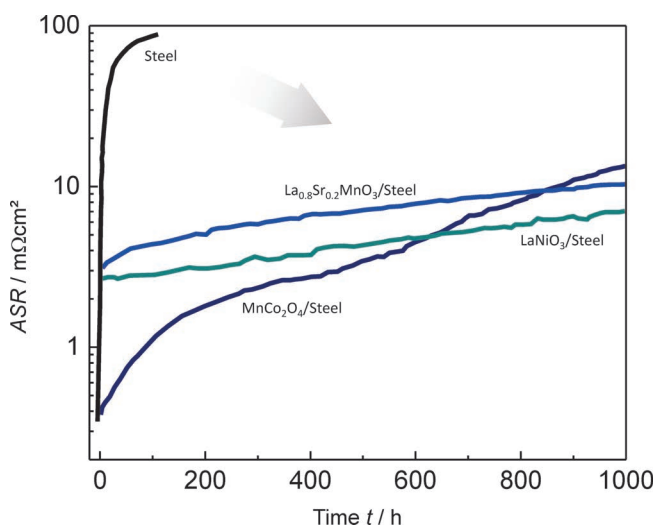


Fig. 28: Area-specific resistance of bare stainless steel (SS) and different AD-coated steel versus oxidation time at 800 °C in air (after^{181,185}).

The electrode components of an SOFC need to be porous to provide three phase boundary surfaces. Highly porous films of large area usually have stability problems, and need to be sintered at elevated temperatures ($>1000\text{ }^{\circ}\text{C}$) which, in turn, causes grain growth⁹². Choi *et al.* realized AD films for several cathode materials like $(\text{La,Sr})\text{MnO}_3$ (LSM)¹⁸³, $(\text{La,Sr})(\text{Co,Fe})\text{O}_3$ (LSCF)^{183,220,222,224} and composites like LSM-YSZ⁹² and LSCF-GDC^{21,27}. They adjusted the porosity by co-deposition (AcD) of a powder mixture of $(\text{La,Sr})(\text{Co,Fe})\text{O}_{3-\delta}$ (LSCF) perovskite oxide with polyvinylidene fluoride (PVDF)²²⁴. Porosity increased and adhesion strength to the electrolyte substrate decreased with increasing amount of PVDF²²⁴. For maximum power generation, an optimum between porosity for gas permeability and adhesion for ion conduction has to be found. With a PVDF content of 5 wt%, the power curve for the cell gave a maximum power density (MPD) of 0.79 W/cm^2 at $650\text{ }^{\circ}\text{C}$. Even higher MPD values were subsequently obtained for a different cell setup with both dense electrolyte and highly porous cathode fabricated by AD, as shown in Fig. 29a²²². A maximum power generation can be found for an optimal porosity (polymer loading) and optimal annealing temperature (see Fig. 29b).

The PVDF content also has an effect on crystal size of the film²²⁴. Presumably due to the compliant polymer preventing fracture of the ceramic particles while impact, the crystal size increases, as can be seen from XRD results.

An overview of AD-processed SOFC film materials is given in Table 2 with some comment on properties. Owing to the low-temperature processing, an even broader spectrum of materials and combinations may be realized for improved cell performance. For example, BiMeVO_X AD films have recently been deposited, and conductivity measured¹. Future research should focus on the long-term stability of AD-processed SOFC components.

(10) AD in battery applications

Energy storage using batteries is increasing in portable communication devices and electric vehicles, for example. For high-energy applications like electric vehicles, secondary batteries still suffer from low specific capacity and

energy compared to conventional combustion systems, making them less competitive²²⁵. In comparison to lead-acid and Ni metal hydride, lithium ion batteries (LIBs) have certain advantages in terms of power and energy density^{225,226}, but have safety issues. A solution is all-solid-state batteries (ASSBs). Besides high capacity, the cycle stability and capacity retention over long life-time needs to be ensured. Dense and thin electrolyte layers in the low- μm range can guarantee safe operation by minimizing ohmic losses. As in SOFCs, good adhesion and electrical contact between components is required for battery cells. As one of the first, Popovici *et al.* showed a fully AD all-solid-state battery consisting of $\text{Li}_4\text{Ti}_5\text{O}_{12}$ (LTO) anode, $\text{Li}_{1.3}\text{Al}_{0.3}\text{Ti}_{1.7}(\text{PO}_4)_3$ (LATP) electrolyte and LiCoO_2 (LCO) cathode²²⁷. Cells were tested, but the performance was not sufficient.

In order to increase the mass-specific capacity, novel materials are being studied²²⁸. Silicon, for example, is a promising anode material showing high lithium storage capacity based on the formation of Li-Si alloy (e.g. $\text{Li}_{22}\text{Si}_5$ with a theoretical specific capacity of 4200 mAh/g ²²⁸). This capacity is around ten times higher than that of conventionally used graphite (LiC_6 with theoretical capacity of 370 mAh/g). But along with this reaction comes a strong volume change of approximately 400%, leading to partial destruction of the anode material and low cycle stability. One group uses the so-called *gasdeposition* for Si and composite materials of Si and various additives^{12,229–237}. Punctiform films are formed with a round nozzle by a shot-wise injection of a prescribed amount of powder into the carrier gas. Cyclo-voltammetry and cyclic charge/discharge characterizations were conducted on these samples. Most studies deal with powders of coated Si (e.g. Cu²³⁶, Ru²³⁵, Ni-P²³³) as well as co-deposition of e.g. $\text{La}_2\text{Si/Si}$ ¹² and $\text{Mg}_2\text{Ge/Si}$ ²³⁴. At least for small coating areas, cycling stability and retention were improved over AD films of pristine Si (Fig. 30). Of the shown materials, in particular the Ni-coated Si showed high stability with a specific capacity higher than 500 mAh/g over the whole cycling range.

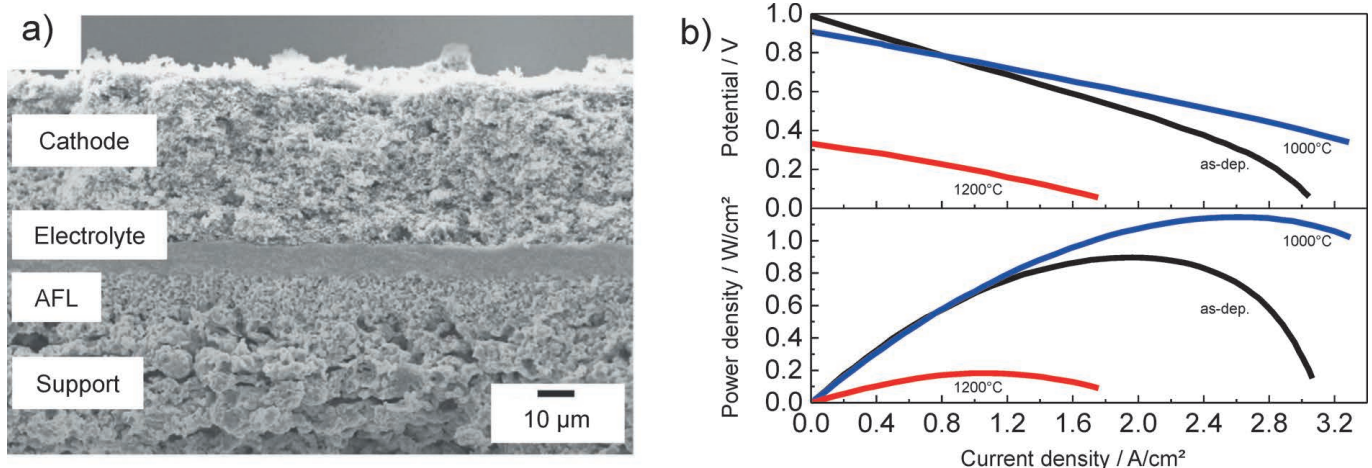


Fig. 29: (a) SEM micrograph of a fracture surface of a cell (electrolyte and cathode by AD) tested at $750\text{ }^{\circ}\text{C}$ (Reprinted from²²² with permission from Elsevier) and (b) I-U and I-P characteristics of cells with different annealing temperatures (operation temperature $750\text{ }^{\circ}\text{C}$) (after²²²).

Table 2: Overview on materials deposited by means of AD for the use as components in SOFC application.

	Material	Ref.	Comment
Oxidation resist./buffer layers (BL)	(La,Sr)MnO ₃ (LSM)	183	Interconnect (IC) oxidation resist., 10 μm, $ASR_{800\text{ }^{\circ}\text{C},100\text{h}}: 20.6\text{ m}\Omega\cdot\text{cm}^2$
		184	IC oxidation resist., 10 μm, $ASR_{800\text{ }^{\circ}\text{C},100\text{h}}: 10.4\text{ m}\Omega\cdot\text{cm}^2$
	YSZ-LSM	98	IC oxidation resist., 2–6 μm, various powder mixtures
	(La,Sr)(Co,Fe)O _{3-δ} (LSCF)	183	IC oxidation resist., 10 μm, $ASR_{800\text{ }^{\circ}\text{C},100\text{h}}: 11.7\text{ m}\Omega\cdot\text{cm}^2$
	MnCo ₂ O ₄	185	IC oxidation resist., 3 μm, $ASR_{800\text{ }^{\circ}\text{C},100\text{h}}: 13.4\text{ m}\Omega\cdot\text{cm}^2$
	LaNiO ₃	181	IC oxidation resist., 5 μm, $ASR_{800\text{ }^{\circ}\text{C},100\text{h}}: 7.34\text{ m}\Omega\cdot\text{cm}^2$
	(Gd,Ce)O _{2-δ} (GDC)-Gd ₂ O ₃	27	Diffusion barrier, YSZ GDC-Gd ₂ O ₃ LSCF-GDC (E BL C), $MPD_{750\text{ }^{\circ}\text{C}}: 1.74\text{ W}/\text{cm}^2$
Interconnect (IC)	(La,Sr)CrO ₃ (LSC)	28	20 μm, cylindrical cell
Cathode (C)	LSM-YSZ	92	35 μm, Ni-YSZ YSZ LSM-YSZ-PVDF (A E AD-C), $MPD_{600\text{ }^{\circ}\text{C}}: 0.14\text{ W}/\text{cm}^2$
	LSCF	222	Ni-GDC LSGMC LSCF (A AD-E AD-C), $MPD_{750\text{ }^{\circ}\text{C}}: 0.9\text{ W}/\text{cm}^2$; diff. annealing temp.
		224	Diff. PVDF-mixture; Ni-GDC LSGMC LSCF (A AD-E AD-C), $MPD_{750\text{ }^{\circ}\text{C}}: 1.11\text{ W}/\text{cm}^2$
		221	Ni-YSZ YSZ LSCF (A AD-E AD-C)
		220	(La,Sr)TiO ₃ diff. barrier, Fe-Cr LST Ni-GDC YSZ LSCF (Support BL A AD-E AD-C), $MPD_{750\text{ }^{\circ}\text{C}}: 0.71\text{ W}/\text{cm}^2$
	LSCF-GDC	21	25 μm, Ni-GDC LSGMC LSCF-GDC (A AD-E AD-C)
Electrolyte (E)	Sc-stabilized ZrO ₂ (ScSZ)	28	8 μm, gas leakage test
	Sm _{0.2} Ce _{0.8} O _{2-δ} (SDC)	223	1.5 μm, Ni SDC LSCF (A AD-E C), $MPD_{700\text{ }^{\circ}\text{C}}: 0.34\text{ W}/\text{cm}^2$
	(La,Sr)(Ga,Mg,Co)O _{3-d} (LSGMC)	222	Ni-GDC LSGMC LSCF (A AD-E AD-C), $MPD_{750\text{ }^{\circ}\text{C}}: 0.9\text{ W}/\text{cm}^2$; diff. annealing temp.
		21	7 μm, Ni-GDC LSGMC LSCF-GDC (A AD-E AD-C), $MPD_{650\text{ }^{\circ}\text{C}}: 0.39\text{ W}/\text{cm}^2$
	YSZ	221	7.5 μm, Ni-YSZ YSZ LSCF (A AD-YSZ AD-LSCF), diff. annealing temp./atm., gas-tightness-test
		220	(La,Sr)TiO ₃ diff. barrier, full cell setup: Fe-Cr LST Ni-GDC YSZ LSCF (Support BL A AD-E AD-C), $MPD_{750\text{ }^{\circ}\text{C}}: 0.71\text{ W}/\text{cm}^2$
	Gd-doped CeO ₂ (GDC)	19	AD and oxygen ion conductivity
Y-doped BaZrO ₃ (BZY)	219	BSZY20, Protonic ceramic fuel cell, diff. powder synthesis, $MPD_{700\text{ }^{\circ}\text{C}}: 0.18\text{ W}/\text{cm}^2$	

Good adhesion of films to the substrate materials over long cycling, a decisive advantage of AD, was also observed for these Si films. Again, these experiments were conducted on small area samples with thicknesses of 1–4 μm. Attempts at larger areas have not been reported as far as the authors know.

Ahn *et al.* described the aerosol deposition of graphite and of iron oxide, the latter being another potential anode material with high theoretical capacity for lithium ions²³⁸. Several investigations show cyclability up to 1000 discharges^{12,229,233,235}. Many AD battery cells show spe-

cific discharge capacities far below the theoretical value of the material. Inada *et al.* interpret this behavior as an effect of film strain and degraded crystallinity resulting from the AD mechanism²³⁹. By depositing agglomerated Li₄Ti₅O₁₂ (LTO) powder as anodes, they formed porous films with a crystallinity comparable to the raw powder and free of internal stress. Using a liquid electrolyte setup, the discharge capacity of the films was found to be as good as 91 % of the theoretical specific capacity (ca. 175 mAh/g) of LTO (0.5C-rate) with good capacity retention over 100 cycles.

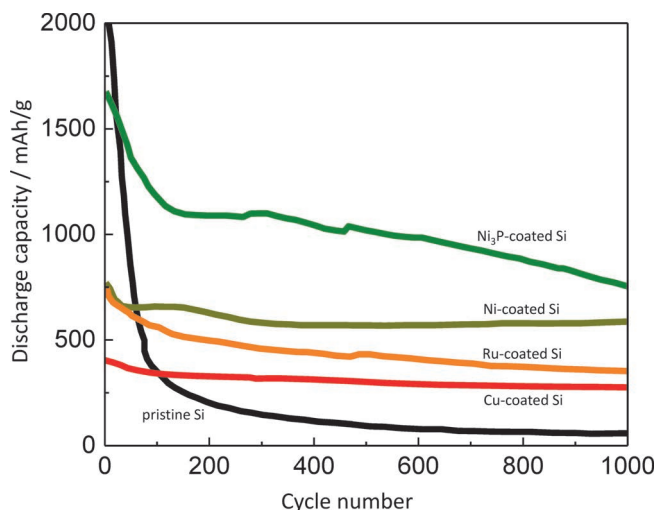


Fig. 30: Dependence of discharge capacity on cycling number for film anodes produced by gas deposition (see Section 2) of pristine Si and Si particles with different coatings of Ni₃P, Ni, Ru and Cu, after ^{229, 235, 236}.

Several groups are also dealing with processing of cathode materials such as LiFePO₄ (LFP)²⁴⁰⁻²⁴², LiNi_xCo_yMn_zO₂ (NMC)^{243, 244} and LiMn₂O₄¹¹.

There are also studies on AD of Li-ion conducting electrolyte materials like the NASICON-type glass-ceramics Li_{1.3}Al_{0.3}Ti_{1.7}(PO₄)₃ (LATP)²⁴⁵ and Li_{1.5}Al_{0.5}Ge_{1.5}(PO₄)₃ (LAGP)²⁴⁶, as well as on Li₇La₃Zr₂O₁₂ (LLZO)²⁴⁷. Khan *et al.*²⁴⁶ deposited LAGP films of more than 10 μm on platinized silicon substrates. The films showed low conductivity in the range of 8.5·10⁻⁹ S/cm in the as-deposited state. However, with annealing at temperatures of 600 and 750 °C, the conductivity could be increased to values of 10⁻⁵ S/cm and 10⁻⁴ S/cm, respectively. However, this temperature step may be detrimental, since it can cause cell degradation from thermal expansion or diffusion.

Table 3 summarizes the literature on battery anode, cathode, and electrolyte materials processed by AD.

As shown already in previous sections, materials properties like ion conductivity are strongly influenced by the crystallinity of the material. Especially for solid electrolyte applications, a dense film morphology is indispensable. This often comes with process-related small crystallite sizes and lattice distortions, which are assumed to result in unwanted low conductivities owing to increased overall resistances of the material. To a good part, recovery of the electrical properties can be achieved by thermal treatment at temperatures markedly below the particular sintering temperature. On the other hand, the technically relevant parameter for electrolyte films is the area-specific resistance, which is also dependent on the film thickness. Since AD films in the low μm-range can be produced densely, this might be a superior advantage of AD.

V. Conclusions and Outlook

In this overview, we have reviewed and summarized the ongoing development in the field of aerosol deposition

since the publication of the first overview paper by Akedo in 2008. There is growing interest in this field, as evidenced by the increasing number of research groups and their scientific publications. Presently, a large variety of ceramic materials, devices and applications are being contemplated.

Fundamental research has mostly been conducted on Al₂O₃. Simulations of particle impact during AD indicate that high energy and strain rates lead to fracturing of particles, corroborating overwhelming experimental evidence of reduced grain size. This is thought to be a relevant step for anchor layer formation and film growth. Continuous bombardment of the growing film with (large) particles, the so-called hammering effect, is thought to be the important mechanism for further build-up and consolidation of the film. While the general picture of impact consolidation is now agreed upon, questions about the detail, like the particle-particle interaction and possible chemical reactions taking part during film formation remain unanswered. One recent investigation provides evidence for a chemical bond between film particles (Al₂O₃) and the substrate (Cu). Such detailed investigations should be extended to cover other materials. A better understanding of the aerosol deposition mechanism(s) and relevant powder characteristics will aid the production of higher quality films and higher deposition efficiencies. More work is needed.

The first commercial AD product is an Y₂O₃ coating for improved plasma resistance applications²⁸. For wear-resistant or passivation coatings, AD is very close to meeting the material demands of high density, good adhesion, and scratch resistance. The films usually do not need thermal post-treatment since full functionality is achieved in the as-deposited state. An increasing number of companies is applying for patents²⁵⁰⁻²⁵³ in the field of solid electrolyte batteries, as well as optical and MEMS devices. In 2010, Akedo stated that already more than 40 patents were submitted each year by Japanese companies²⁵⁴.

Electronic ceramics like PZT and BaTiO₃ have been aerosol-deposited, but properties of sprayed films – especially if dominated by grain boundary effects – are often different from bulk ceramics. This is due to the reduced particle size and crystallinity, and increased residual stress in the film. Annealing treatments must often be used to improve properties to acceptable levels, but at least these annealing temperatures are typically far lower than normal sintering temperatures. This gives AD a distinct advantage.

Regarding SOFCs applications, annealing could take place during initial usage at the operation temperature of several hundred degrees Celsius. For battery AD solid electrolytes, partial recovery from the lowered ionic conductivity has also been observed. The area-specific resistance (ASR) may be effectively controlled with AD layer thickness.

Table 3: Overview on investigated materials for battery cell applications conducted with AD

	Material	Ref.	Comment
Anode	Li ₄ Ti ₅ O ₁₂ (LTO)	227	Full cell setup by AD
		239	91 % of discharge cap. of theoretical cap. (at 0.5C rate), good cap. retention
	Si	237	Carrier gas influence, spot-like gas deposition
	Si (Cu-coated)	236	Spot-like gas deposition; 570 mAh/g at 1000 cycles
	FeSi/Si	230	Influence of mechanical grinding
	Si (Ru-coated)	235	Punctiform gas deposition; 570 mAh/g at 1000 cycles
	Si (Ni-, Ni-Sn-, Ni-P-coated)	229	Punctiform gas deposition; 790 mAh/g at 1000 cycles (Ni-P)
	Si (Ni-P-coated)	233	Point-like gas deposition; 780 mAh/g at 1000 cycles
	Si (Ni and Cu-coated)	231	Punctiform gas deposition
	TiO ₂ /Si	232	Point-like gas deposition; 710 mAh/g at 900 cycles
	Mg ₂ Ge	248, 249	Punctiform gas deposition
	Mg ₂ Ge/Si	234	Punctiform gas deposition
	LaSi ₂ /Si	12	Punctiform gas deposition; 500 mAh/g after 300 cycles
	Graphite	240	Thickness: 250 nm; Full cell test
Fe ₂ O ₃	238	Film Thickness: 300 nm	
Cathode	LiCoO ₂ (LCO)	227	Full cell setup by AD
	LiNi _{1/3} Co _{1/3} Mn _{1/3} O ₂ (NMC)	243	Discharge cap. 152 mAh/g at 20 cycles
	LiNi _{0.4} Co _{0.3} Mn _{0.3} O ₂	244	
	LiMn ₂ O ₄	11	79% of initial discharge cap. after 500 cycles
	LiFePO ₄ (C-coated)	240	Thickness 1 μm; Full cell test
242		Thickness 0.75 μm	
241		SSB: AD-LFP/LLZO/Li metal	
Electrolyte	Li _{1.3} Al _{0.3} Ti _{1.7} (PO ₄) ₃ (LATP)	227	Full cell setup by AD
		245	σ_{bulk} : 3.62·10 ⁻³ S/cm; σ_{total} : 1.12·10 ⁻⁶ S/cm
	Li _{1.5} Al _{0.5} Ge _{1.5} (PO ₄) ₃ (LAGP)	246	Thickness of 10 μm; Effect of annealing on conductivity, $\sigma_{\text{as-dep}}$: 8.49·10 ⁻⁹ S/cm, $\sigma_{750^\circ\text{C}}$: 1.16·10 ⁻⁴ S/cm
	Li ₇ La ₃ Zr ₂ O ₁₂	247	Film thickness LLZO: 20 μm; SSB: AD-LFP/AD-LLZO/Li metal

Although touted as a means to thicken ceramic films with high density, AD can also be used to produce adherent and stable films with controlled porosity. This opens up new applications in the fields of membranes, sensors, catalytic supports, etc. This is beginning to receive attention, with novel approaches for engineering porosity using mixtures of materials in co-depositions (AcD and AcDc). Other tailorable features include gradient, multilayering, and patterning.

Additional materials and applications for AD will undoubtedly emerge, likely in the very near future. Expectations are for energy-related materials, like thermoelectrics^{255,256}, and superconductors^{257–259}, optical coatings, and thermal barrier coatings. Materials like metallic glasses, which are studied intensively at the mo-

ment¹⁰, are also promising candidates for commercial application. Several AD attributes such as coating flexibility on metal or polymer foils, patterning of surfaces, and multilayer or material and porosity gradient films, all give potential for application in many fields.

Engineering challenges which remain for commercial adoption of AD as a competitive manufacturing process include: scale-up to larger coating areas using larger or multi-nozzle designs²⁸, reel-to-reel processing of large areas²⁹ and deposition onto complex (non-planar) geometries. One major disadvantage for AD is the very low deposition efficiency, often less than 1%²⁶⁰. A deeper investigation of process efficiency and materials recycling or recirculation in the process is necessary to limit costs. Just a few publications deal with this^{260,261}, despite its

importance with respect to commercialization of this process.

On the other hand, for low-volume production or rapid prototyping requiring flexibility, AD offers an advantage over conventional coating processes. AD may also enable a significant decrease in environmental load (toxic chemicals), as well as power consumption and manufacturing time²⁶². For example, patterning of films is possible with masks directly during coating, eliminating the need for toxic etching chemicals. Power consumption can be drastically lowered, since AD films require lower temperature heat treatment, or in some cases no treatment at all. Short cycle times and small investment costs for the equipment make AD an economical coating process.

Acknowledgement

The authors are grateful to Dr. Kathy Sahner, who initiated research in the AD field at the Department of Functional Materials. We acknowledge the German Research Foundation (DFG) and the National Science Foundation (NSF) for funding within the framework of the Materials World Network (grant MO 1060/16-1 and 1108466), the DFG Mercator fellowship (grant MO 1060/20), and the Bavarian Research Foundation (BFS) for direct support (grant AZ-1055-12).

References

- Exner, J., Fuierer, P., Moos, R.: Aerosol deposition of (Cu,Ti) substituted bismuth vanadate films, *Thin Solid Films*, **573**, 185–190, (2014), doi: 10.1016/j.tsf.2014.11.037.
- Kashu, S., Fuchita, E., Manabe, T., Hayashi, C.: Deposition of ultra fine particles using a gas jet, *Jpn. J. Appl. Phys.*, **23**, L910, (1984), doi: 10.1143/JJAP.23.L910.
- Akedo, J., Ichiki, M., Kikuchi, K., Maeda, R.: Jet molding system for realization of three-dimensional micro-structures, *Sens. Actuat., A-Phys.*, **69**, 106–112, (1998), doi: 10.1016/S0924-4247(98)00059-4.
- Akedo, J., Masaaki, I., Maeda, R.: New functional ceramic deposition method for MEMS, *Ferroelectrics*, **224**, 331–337, (1999), doi: 10.1080/00150199908210584.
- Akedo, J., Lebedev, M.: Microstructure and electrical properties of lead zirconate titanate (Pb(Zr₅₂/Ti₄₈)O₃) thick films deposited by aerosol deposition method, *Jpn. J. Appl. Phys.*, **38**, 5397–5401, (1999), doi: 10.1143/JJAP.38.5397.
- Akedo, J.: Room temperature impact consolidation (RTIC) of fine ceramic powder by aerosol deposition method and applications to microdevices, *J. Therm. Spray Technol.*, **17**, 181–198, (2008), doi: 10.1007/s11666-008-9163-7.
- Fan, S.-Q., Yang, G.-J., Li, C.-J., Liu, G.-J., Li, C.-X., Zhang, L.-Z.: Characterization of microstructure of nano-TiO₂ coating deposited by vacuum cold spraying, *J. Therm. Spray Technol.*, **15**, 513–517, (2006), doi: 10.1361/105996306X146901.
- Liu, Y., Wang, Y.-Y., Yang, G.-J., Feng, J.-J., Kusumoto, K.: Effect of nano-sized TiN additions on the electrical properties of vacuum cold sprayed SiC coatings, *J. Therm. Spray Technol.*, **19**, 1238–1243, (2010), doi: 10.1007/s11666-010-9544-6.
- Cao, F., Park, H., Bae, G., Heo, J., Lee, C.: Microstructure evolution of titanium nitride film during vacuum kinetic spraying, *J. Am. Ceram. Soc.*, **96**, 40–43, (2013), doi: 10.1111/jace.12101.
- Kwon, J., Park, H., Lee, I., Lee, C.: Effect of gas flow rate on deposition behavior of Fe-based amorphous alloys in vacuum kinetic spray process, *Surf. Coat. Technol.*, **259**, 585–593, (2014), doi: 10.1016/j.surfcoat.2014.10.026.
- Takai, S., Sakaguchi, H., Tanaka, K., Nagao, Y., Esaka, T.: Cathode performance of LiMn₂O₄ thick films prepared by gas-deposition for lithium rechargeable battery, *Electrochemistry*, **76**, 293–296, (2008), doi: 10.5796/electrochemistry.76.293.
- Sakaguchi, H., Iida, T., Itoh, M., Shibamura, N., Hirono, T.: Anode properties of LaSi₂/Si composite thick-film electrodes for lithium secondary batteries, *IOP Conf. Ser.: Mater. Sci. Eng.*, **1**, 012030, (2009), doi: 10.1088/1757-8981/1/1/012030.
- Schubert, M., Hanft, D., Moos, R.: Dense ceramic coatings manufactured with the Aerosol-Deposition-Method (ADM) at the department of functional materials; 2014. http://www.funktionsmaterialien.de/docs/Highlight_ADM_ENG.pdf (accessed on 12 February, 2015).
- Akedo, J.: Aerosol deposition of ceramic thick films at room Temperature: densification mechanism of ceramic layers, *J. Am. Ceram. Soc.*, **89**, 1834–1839, (2006), doi: 10.1111/j.1551-2916.2006.01030.x.
- Piechowiak, M.A., Henon, J., Durand-Panteix, O., Etchegoyen, G., Coudert, V., Marchet, P., Rossignol, F.: Growth of dense Ti₃SiC₂ MAX phase films elaborated at room temperature by aerosol deposition method, *J. Eur. Ceram. Soc.*, **34**, 1063–1072, (2014), doi: 10.1016/j.jeurceramsoc.2013.11.019.
- Seo, D.S., Lee, J.K., Hwang, K.H., Hahn, B.-D., Yoon, S.Y.: Influence of starting powders on hydroxyapatite coatings fabricated by room temperature spraying method, *J. Nanosci. Nanotechnol.*, **15**, 6032–6038, (2015), doi: 10.1166/jnn.2015.10437.
- Charles, E.R., Johnson, S.D., Kub, F.J.: ZnS/Diamond composite coatings for infrared transmission applications formed by the aerosol deposition method, *Proc. SPIE*, **8708**, (2013), doi: 10.1117/12.2029717.
- Lin, S.-C., Wu, W.-J.: Fabrication of PZT MEMS energy harvester based on silicon and stainless-steel substrates utilizing an aerosol deposition method, *J. Micromech. Microeng.*, **23**, 125028, (2013), doi: 10.1088/0960-1317/23/12/125028.
- Bae, H., Choi, J., Choi, G.M.: Electrical conductivity of Gd-doped ceria film fabricated by aerosol deposition method, *Solid State Ionics*, **236**, 16–21, (2013), doi: 10.1016/j.ssi.2013.01.022.
- Yang, G.-J., Liao, K.-X., Li, C.-J., Fan, S.-Q., Li, C.-X., Li, S.: Formation of pore structure and its influence on the mass transport property of vacuum cold sprayed TiO₂ coatings using strengthened nanostructured powder, *J. Therm. Spray Technol.*, **21**, 505–513, (2012), doi: 10.1007/s11666-012-9741-6.
- Choi, J.-J., Cho, K.-S., Choi, J.-H., Ryu, J., Hahn, B.-D., Yoon, W.-H., Kim, J.-W., Ahn, C.-W., Yun, J., Park, D.-S.: Low temperature preparation and characterization of LSGMC based IT-SOFC cell by aerosol deposition, *J. Eur. Ceram. Soc.*, **32**, 115–121, (2012), doi: 10.1016/j.jeurceramsoc.2011.07.036.
- Nam, S.-M., Mori, N., Kakemoto, H., Wada, S., Akedo, J., Tsurumi, T.: Alumina thick films as integral substrates using aerosol deposition method, *Jpn. J. Appl. Phys.*, **43**, 5414–5418, (2004), doi: 10.1143/JJAP.43.5414.
- Mihara, K., Hoshina, T., Takeda, H., Tsurumi, T.: Controlling factors of film-thickness in improved aerosol deposition method, *J. Ceram. Soc. Jpn.*, **117**, 868–872, (2009), doi: 10.2109/jcersj.2.117.868.
- Hinds, W.C.: Aerosol technology: Properties, behavior, and measurement of airborne particles. 2nd edition. Wiley, New York, (1999).
- Lee, M., Park, J., Kim, D., Yoon, S., Kim, H., Kim, D., James, S., Chandra, S., Coyle, T., Ryu, J., Yoon, W. H., Park, D. S.: Optimization of supersonic nozzle flow for titanium dioxide thin-film coating by aerosol deposition, *J. Aerosol Sci.*, **42**, 771–780, (2011), doi: 10.1016/j.jaerosci.2011.07.006.

- 26 Park, J.-J., Lee, M.-W., Yoon, S.S., Kim, H.-Y., James, S.C., Heister, S.D., Chandra, S., Yoon, W.-H., Park, D.-S., Ryu, J.: Supersonic nozzle flow simulations for particle coating Applications: effects of shockwaves, nozzle geometry, ambient pressure, and substrate location upon flow characteristics, *J. Therm. Spray Technol.*, **20**, 514–522, (2011), doi: 10.1007/s11666-010-9542-8.
- 27 Choi, J.-J., Park, D.-S., Seong, B.-G., Bae, H.-Y.: Low-temperature preparation of dense (Gd,Ce)O_{2-δ}-Gd₂O₃ composite buffer layer by aerosol deposition for YSZ electrolyte-based SOFC, *Int. J. Hydrogen Energ.*, **37**, 9809–9815, (2012), doi: 10.1016/j.ijhydene.2012.03.148.
- 28 Hatono, H., Ito, T., Matsumura, A.: Technological Development of Aerosol Deposition at TOTO Ltd. In: 4th Tsukuba International Coatings Symposium, Frontiers of Coatings Technology: Innovative Processes and Applications, 2010, 15–16.
- 29 Arndt, T.: Method and arrangement for producing superconducting layers on substrates. U.S. Patent Application 2013/0123112, (2011).
- 30 Henon, J., Piechowiak, M.A., Durand-Panteix, O., Etchegoyen, G., Masson, O., Dublanche-Tixier, C., Marchet, P., Lucas, B., Rossignol, F.: Dense and highly textured coatings obtained by aerosol deposition method from Ti₃SiC₂ powder: comparison to a dense material sintered by spark plasma sintering, *J. Eur. Ceram. Soc.*, **35**, 1179–1189, (2015), doi: 10.1016/j.jeurceramsoc.2014.10.012.
- 31 Dong-Won L., Song-Min N.: Factors affecting surface roughness of Al₂O₃ films deposited on cu substrates by an aerosol deposition method, *J. Ceram. Process. Res.*, **11**, 100–106, (2010).
- 32 Akedo, J.: Aerosol deposition method for fabrication of nano crystal ceramic layer, *Mater. Sci. Forum*, **449–452**, 43–48, (2004), doi: 10.4028/www.scientific.net/MSF.449-452.43.
- 33 Fan, S.-Q., Li, C.-J., Yang, G.-J., Zhang, L.-Z., Gao, J.-C., Xi, Y.-X.: Fabrication of nano-TiO₂ coating for dye-sensitized solar cell by vacuum cold spraying at room temperature, *J. Therm. Spray Technol.*, **16**, 893–897, (2007), doi: 10.1007/s11666-007-9090-z.
- 34 Nguyen, T.N., Denneler, S., Ahlstedt, M., Schuh, C., Moos, R.: Fabrication and characterization of optical Ceramic layers using the aerosol deposition method. In: CIMTEC 13th International Ceramics Congress, 2014.
- 35 Nakada, M., Tsuda, H., Ohashi, K., Akedo, J.: Aerosol deposition on transparent electro-optic films for optical modulators, *IEICE Transactions on Electronics*, **90**, 36–40, (2007), doi: 10.1093/ietele/e90-c.1.36.
- 36 Apetz, R., Bruggen, Michel P.B.: Transparent Alumina: A light-scattering model, *J. Am. Ceram. Soc.*, **86**, 480–486, (2003), doi: 10.1111/j.1151-2916.2003.tb03325.x.
- 37 Krell, A., Blank, P., Ma, H., Hutzler, T., Bruggen, Michel P.B., Apetz, R.: Transparent sintered corundum with high hardness and strength, *J. Am. Ceram. Soc.*, **86**, 12–18, (2003), doi: 10.1111/j.1151-2916.2003.tb03270.x.
- 38 Lee, D.-W., Kim, H.-J., Kim, Y.-H., Yun, Y.-H., Nam, S.-M.: Growth process of α-Al₂O₃ ceramic films on metal substrates fabricated at room temperature by aerosol deposition, *J. Am. Ceram. Soc.*, **94**, 3131–3138, (2011), doi: 10.1111/j.1551-2916.2011.04493.x.
- 39 Lebedev, M., Akedo, J.: Patterning properties of PZT thick films made by aerosol deposition, *Ferroelectrics*, **270**, 117–122, (2002), doi: 10.1080/00150190211232.
- 40 Lee, D.-W., Kim, H.-J., Kim, Y.-N., Jeon, M.-S., Nam, S.-M.: Substrate hardness dependency on properties of Al₂O₃ thick films grown by aerosol deposition, *Surf. Coat. Technol.*, **209**, 160–168, (2012), doi: 10.1016/j.surfcoat.2012.08.012.
- 41 Yao, Z., Wang, C., Li, Y., Kim, H.-K., Kim, N.-Y.: Effects of starting powder and thermal treatment on the aerosol deposited BaTiO₃ thin films toward less leakage currents, *Nanoscale Res. Lett.*, **9**, 435, (2014), doi: 10.1186/1556-276X-9-435.
- 42 Schubert, M., Exner, J., Moos, R.: Influence of carrier gas composition on the stress of Al₂O₃ coatings prepared by the aerosol deposition method, *Materials*, **7**, 5633–5642, (2014), doi: 10.3390/ma7085633.
- 43 Park, J.-J., Lee, J.-G., Kim, D.-Y., Hong, J.-H., Kim, J.-J., Hong, S., Yoon, S.S.: Antibacterial and water purification activities of self-assembled honeycomb structure of aerosol deposited titania film, *Environ. Sci. Technol.*, **46**, 12510–12518, (2012), doi: 10.1021/es3037252.
- 44 Fuchita, E., Tokizaki, E., Ozawa, E., Sakka, Y.: Appearance of high-temperature phase in zirconia films made by aerosol gas deposition method, *J. Ceram. Soc. Jpn.*, **119**, 271–276, (2011), doi: 10.2109/jcersj2.119.271.
- 45 Iwata, A., Akedo, J.: Hexagonal to cubic crystal structure transformation during aerosol deposition of aluminum nitride, *J. Cryst. Growth*, **275**, e1269, (2005), doi: 10.1016/j.jcrysgro.2004.11.082.
- 46 Iwata, A., Akedo, J., Lebedev, M.: Cubic aluminum nitride transformed under reduced pressure using aerosol deposition method, *J. Am. Ceram. Soc.*, **88**, 1067–1069, (2005), doi: 10.1111/j.1551-2916.2005.00215.x.
- 47 Ryu, J., Park, D.-S., Hahn, B.-D., Choi, J.-J., Yoon, W.-H., Kim, K.-Y., Yun, H.-S.: Photocatalytic TiO₂ thin films by aerosol-deposition: from micron-sized particles to nano-grained thin film at room temperature, *Appl. Catal., B*, **83**, 1–7, (2008), doi: 10.1016/j.apcatb.2008.01.020.
- 48 Papyrin, A.: Cold spray technology, *Adv. Mater. Process.*, **159**, 49–51, (2001).
- 49 Assadi, H., Gärtner, F., Stoltenhoff, T., Kreye, H.: Bonding mechanism in cold gas spraying, *Acta Mater.*, **51**, 4379–4394, (2003), doi: 10.1016/S1359-6454(03)00274-X.
- 50 van Steenkiste, T.H., Smith, J.R., Teets, R.E.: Aluminum coatings via kinetic spray with relatively large powder particles, *Surf. Coat. Technol.*, **154**, 237–252, (2002), doi: 10.1016/S0257-8972(02)00018-X.
- 51 Li, W.-Y., Li, C.-J., Wang, H.-T., Li, C.-X., Bang, H.-S.: Measurement and numerical simulation of particle velocity in cold spraying, *J. Therm. Spray Technol.*, **15**, 559–562, (2006), doi: 10.1361/105996306X146956.
- 52 Schmidt, T., Assadi, H., Gärtner, F., Richter, H., Stoltenhoff, T., Kreye, H., Klassen, T.: From particle acceleration to impact and bonding in cold spraying, *J. Therm. Spray Technol.*, **18**, 794–808, (2009), doi: 10.1007/s11666-009-9357-7.
- 53 Grujicic, M., Zhao, C., DeRosset, W., Helffrich, D.: Adiabatic shear instability based mechanism for particles/substrate bonding in the cold-gas dynamic-spray process, *Mater. Design*, **25**, 681–688, (2004), doi: 10.1016/j.matdes.2004.03.008.
- 54 Schmidt, T., Gärtner, F., Assadi, H., Kreye, H.: Development of a generalized parameter window for cold spray deposition, *Acta Mater.*, **54**, 729–742, (2006), doi: 10.1016/j.actamat.2005.10.005.
- 55 Li, C.-J., Li, W.-Y., Liao, H.: Examination of the critical velocity for deposition of particles in cold spraying, *J. Therm. Spray Technol.*, **15**, 212–222, (2006), doi: 10.1361/105996306X108093.
- 56 Kliemann, J.-O., Gutzmann, H., Gärtner, F., Hübner, H., Borchers, C., Klassen, T.: Formation of cold-sprayed ceramic titanium dioxide layers on metal surfaces, *J. Therm. Spray Technol.*, **20**, 292–298, (2011), doi: 10.1007/s11666-010-9563-3.
- 57 Sarobol, P., Hall, A.C., Urrea, D.A., Chandross, M.E., Carroll, J.D., Boyce, B.L., Mook, W.M., Kotula, P.G., McKenzie, B.B., Bufford, D.C.: Deformation behavior of sub-micron and micron sized alumina particles in compression, Albuquerque, New Mexico, (2014).

- 58 Yoshida, M., Ogiso, H., Nakano, S., Akedo, J.: Compression test system for a single submicrometer particle, *Rev. Sci. Instrum.*, **76**, 093905, (2005), doi: 10.1063/1.2038187.
- 59 Naoe, K., Nishiki, M., Sato, K.: Microstructure and electron energy-loss spectroscopy analysis of interface between Cu substrate and Al₂O₃ film formed by aerosol deposition method, *J. Therm. Spray Technol.*, **23**, 1333–1338, (2014), doi: 10.1007/s11666-014-0172-4.
- 60 Exner, J., Hahn, M., Schubert, M., Hanft, D., Fuierer, P., Moos, R.: Powder requirements for aerosol deposition of alumina films, *Adv. Powder Technol.*, **26**, 1143–1151, (2015), doi: 10.1016/j.appt.2015.05.016.
- 61 Kim, J., Lee, J.I., Park, D.S., Park, E.S.: Enhancement of interface anchoring and densification of Y₂O₃ coating by metal substrate manipulation in aerosol deposition process, *J. Appl. Phys.*, **117**, 014903, (2015), doi: 10.1063/1.4905241.
- 62 Kim, C.-W., Choi, J.-H., Kim, H.-J., Lee, D.-W., Hyun, C.-Y., Nam, S.-M.: Effects of interlayer roughness on deposition rate and morphology of aerosol-deposited Al₂O₃ thick films, *Ceram. Int.*, **38**, 5621–5627, (2012), doi: 10.1016/j.ceramint.2012.04.003.
- 63 Maki, T., Sugimoto, S., Kagotani, T., Inomata, K., Akedo, J., Ishikawa, T., Ohmori, K.: Influence of deposition angle on the magnetic properties of Sm-Fe-N films fabricated by aerosol deposition method, *J. Alloys Compd.*, **408–412**, 1409–1412, (2006), doi: 10.1016/j.jallcom.2005.04.040.
- 64 Johnson, G.R., Holmquist, T.J.: An improved computational constitutive model for brittle materials, *AIP Conf. Proc.*, **309**, 981–984, (1994), doi: 10.1063/1.46199.
- 65 Holmquist, T.J., Templeton, D.W., Bishnoi, K.D.: Constitutive modeling of aluminum nitride for large strain, high-strain rate, and high-pressure applications, *Int. J. Impact Eng.*, **25**, 211–231, (2001), doi: 10.1016/S0734-743X(00)00046-4.
- 66 Ogawa, H.: Molecular dynamics simulation on the single particle impacts in the aerosol deposition process, *Mater. Trans.*, **46**, 1235–1239, (2005), doi: 10.2320/matertrans.46.1235.
- 67 Ogawa, H.: Atomistic simulation of the aerosol deposition method with zirconia nanoparticles, *Mater. Trans.*, **47**, 1945–1948, (2006), doi: 10.2320/matertrans.47.1945.
- 68 Ogawa, H.: Molecular dynamics simulation on the modification of crystallographic orientation in fragmented particles in the aerosol-deposition process, *Mater. Trans.*, **48**, 2067–2071, (2007), doi: 10.2320/matertrans.MA200712.
- 69 Daneshian, B., Assadi, H.: Impact behavior of intrinsically brittle Nanoparticles: A molecular dynamics perspective, *J. Therm. Spray Technol.*, **23**, 541–550, (2013), doi: 10.1007/s11666-013-0019-4.
- 70 Chun, D.-M., Ahn, S.-H.: Deposition mechanism of dry sprayed ceramic particles at room temperature using a nanoparticle deposition system, *Acta Mater.*, **59**, 2693–2703, (2011), doi: 10.1016/j.actamat.2011.01.007.
- 71 Akedo, J., Lebedev, M.: Powder preparation in aerosol deposition method for lead zirconate titanate thick films, *Jpn. J. Appl. Phys.*, **41**, 6980–6984, (2002), doi: 10.1143/JJAP.41.6980.
- 72 Carr, R.E.: Evaluating flow properties of solids, *Chem. Eng.*, **72**, 163–168, (1965).
- 73 Exner, J., Fuierer, P., Moos, R.: Aerosol codeposition of Ceramics: mixtures of Bi₂O₃-TiO₂ and Bi₂O₃-V₂O₅, *J. Am. Ceram. Soc.*, **98**, 717–723, (2014), doi: 10.1111/jace.13364.
- 74 Choi, J.-J., Jang, J.H., Park, D.S., Hahn, B.-D., Yoon, W.H., Park, C.: Electrical properties of lead zinc niobate - lead zirconate titanate thick films formed by aerosol deposition process, *Solid State Phenom.*, **124–126**, 169–172, (2007), doi: 10.4028/www.scientific.net/SSP.124-126.169.
- 75 Yuuki, K., Sato, Y., Yoshikado, S.: Fabrication of nanoporous titanium dioxide films using aerosol deposition, *Key Eng. Mater.*, **582**, 141–144, (2013), doi: 10.4028/www.scientific.net/KEM.582.141.
- 76 Sugimoto, S., Chan, V., Noguchi, M., Tezuka, N., Inomata, K., Akedo, J.: Preparation of Fe/Ni-Zn-Cu ferrite stacked films by aerosol deposition method, *J. Magn. Magn. Mater.*, **310**, 2549–2551, (2007), doi: 10.1016/j.jmmm.2006.11.146.
- 77 Seto, N., Hirose, S., Tsuda, H., Akedo, J.: Formation of tough foundation layer for electrical plating on insulator using aerosol deposition method of Cu-Al₂O₃ Mixed Powder, In: J. Akedo, T.-Y. Tseng, X.M. Chen, H.-T. Lin (eds.). In: Advances in multifunctional materials and systems II: John Wiley & Sons, Inc, Hoboken, NJ, USA, (2014, p. 17–22, ISBN 9781118771402), doi: 10.1002/9781118771402.ch2.
- 78 Park, J.-H., Akedo, J., Nakada, M.: Surface plasmon resonance in novel nanocomposite Gold/Lead zirconate titanate films prepared by aerosol deposition method, *Jpn. J. Appl. Phys.*, **45**, 7512–7515, (2006), doi: 10.1143/JJAP.45.7512.
- 79 Fan, S.-Q., Li, C.-J., Li, C.-X., Liu, G.-J., Yang, G.-J., Zhang, L.-Z.: Preliminary study of performance of dye-sensitized solar cell of nano-TiO₂ coating deposited by vacuum cold spraying, *Mater. Trans.*, **47**, 1703–1709, (2006), doi: 10.2320/matertrans.47.1703.
- 80 Kim, H., Yoon, Y.J., Kim, J., Nam, S.: Application of Al₂O₃-based polyimide composite thick films to integrated substrates using aerosol deposition method, *Mater. Sci. Eng., B*, **161**, 104–108, (2009), doi: 10.1016/j.mseb.2008.12.041.
- 81 Choi, J.-J., Hahn, B.-D., Ryu, J., Yoon, W.-H., Lee, B.-K., Park, D.-S.: Preparation and characterization of piezoelectric ceramic-polymer composite thick films by aerosol deposition for sensor application, *Sens. Actuators, A*, **153**, 89–95, (2009), doi: 10.1016/j.sna.2009.04.025.
- 82 Liu, Y., Dang, Z., Wang, Y., Huang, J., Li, H.: Hydroxyapatite/graphene-nanosheet composite coatings deposited by vacuum cold spraying for biomedical applications: inherited nanostructures and enhanced properties, *Carbon*, **67**, 250–259, (2014), doi: 10.1016/j.carbon.2013.09.088.
- 83 Kim, D.-Y., Joshi, B.N., Park, J.-J., Lee, J.-G., Cha, Y.-H., Seong, T.-Y., Noh, S. in, Ahn, H.-J., Yoon, S.S.: Graphene-titania films by supersonic kinetic spraying for enhanced performance of dye-sensitized solar cells, *Ceram. Int.*, (2014), doi: 10.1016/j.ceramint.2014.03.131.
- 84 Kim, Y.-H., Osada, M., Kim, H.-K., Nam, S.-M.: Percolative BaTiO₃/Carbon-nanotube composite films employing aerosol deposition, *Jpn. J. Appl. Phys.*, **51**, 09LC07, (2012), doi: 10.1143/JJAP.51.09LC07.
- 85 Hahn, B.-D., Park, D.-S., Choi, J.-J., Ryu, J., Yoon, W.-H., Choi, J.-H., Kim, H.-E., Kim, S.-G.: Aerosol deposition of hydroxyapatite-chitosan composite coatings on biodegradable magnesium alloy, *Surf. Coat. Technol.*, **205**, 3112–3118, (2011), doi: 10.1016/j.surfcoat.2010.11.029.
- 86 Wang, Y.-Y., Liu, Y., Li, C.-J., Yang, G.-J., Feng, J.-J., Kusumoto, K.: Investigation on the electrical properties of vacuum cold sprayed SiC-MoSi₂ coatings at elevated temperatures, *J. Therm. Spray Technol.*, **20**, 892–897, (2011), doi: 10.1007/s11666-011-9635-z.
- 87 Kim, Y.-H., Kim, H.-J., Koh, J.-H., Ha, J.-G., Yun, Y.-H., Nam, S.-M.: Fabrication of BaTiO₃-PTFE composite film for embedded capacitor employing aerosol deposition, *Ceram. Int.*, **37**, 1859–1864, (2011), doi: 10.1016/j.ceramint.2011.02.014.
- 88 Kwon, O.-Y., Na, H.-J., Kim, H.-J., Lee, D.-W., Nam, S.-M.: Effects of mechanical properties of polymer on ceramic-polymer composite thick films fabricated by aerosol deposition, *Nanoscale Res. Lett.*, **7**, 261, (2012), doi: 10.1186/1556-276X-7-261.
- 89 Yang, G.-J., Li, C.-J., Fan, S.-Q., Wang, Y.-Y., Li, C.-X.: Influence of annealing on photocatalytic performance and adhesion of vacuum cold-sprayed nanostructured TiO₂

- coating, *J. Therm. Spray Techn.*, **16**, 873–880, (2007), doi: 10.1007/s11666-007-9109-5.
- 90 Kim, H.-J., Kwon, O.-Y., Jang, C.-I., Kim, T.K., Oh, J.R., Yoon, Y.J., Kim, J.-H., Nam, S.-M., Koh, J.-H.: Room-temperature growth of ni-zn-cu ferrite/PTFE composite thick films on PET via aerosol deposition, *Electron. Mater. Lett.*, **9**, 805–807, (2013), doi: 10.1007/s13391-013-6016-4.
- 91 Kim, H.-J., Nam, S.-M.: High loading of nanostructured ceramics in polymer composite thick films by aerosol deposition, *Nanoscale Res. Lett.*, **7**, 92, (2012), doi: 10.1186/1556-276X-7-92.
- 92 Choi, J.-J., Oh, S.-H., Noh, H.-S., Kim, H.-R., Son, J.-W., Park, D.-S., Choi, J.-H., Ryu, J., Hahn, B.-D., Yoon, W.-H.; et al.: Low temperature fabrication of nano-structured porous LSM-YSZ composite cathode film by aerosol deposition, *J. Alloys Compd.*, **509**, 2627–2630, (2011), doi: 10.1016/j.jallcom.2010.11.169.
- 93 Ryu, J., Hahn, B.-D., Choi, J.-J., Yoon, W.-H., Lee, B.-K., Choi, J.H., Park, D.-S.: Porous photocatalytic TiO₂ thin films by aerosol deposition, *J. Am. Ceram. Soc.*, **93**, 55–58, (2010), doi: 10.1111/j.1551-2916.2009.03391.x.
- 94 Hyung-Jun, K., Yoon-Hyun, K., Song-Min, N., Young, J.Y., Jong-Hee, K.: Calculation of Al₂O₃ contents in Al₂O₃-PTFE composite thick films fabricated by using the aerosol deposition, *J. Korean Phys. Soc.*, **57**, 1086, (2010), doi: 10.3938/jkps.57.1086.
- 95 Cho, S.H., Yoon, Y.J., Kim, H.T., Kim, J., Kim, H.-J., Nam, S.M., Baik, H.K., Kim, J.-H.: Growth of Al₂O₃-PTFE composite film at room temperature by aerosol deposition method, *Ceram. Int.*, **38**, 131–134, (2012), doi: 10.1016/j.ceramint.2011.04.066.
- 96 Kim, H.-J., Nam, S.-M., Koh, J.-H.: Fe-Si-Cr/PTFE Magnetic Composite Thick Films on Polyethylene Terephthalate Sheets for Near Field Communications by Aerosol Deposition, *J. Nanosci. Nanotechnol.*, **14**, 7915–7918, (2014), doi: 10.1166/jnn.2014.9417.
- 97 Kim, H.J., Kim, Y.H., Lee, J.W., Nam, S.M., Yoon, Y.J., Kim, J.H.: Residual stress relief in Al₂O₃-Poly-Tetra-Fluoroethylene hybrid thick films for integrated substrates using aerosol deposition, *J. Nanoelectron. Optoe.*, **7**, 287–291, (2012), doi: 10.1166/jno.2012.1305.
- 98 Choi, J.-J., Ryu, J., Hahn, B.-D., Yoon, W.-H., Lee, B.-K., Choi, J.-H., Park, D.-S.: Oxidation behavior of ferritic steel alloy coated with LSM-YSZ composite ceramics by aerosol deposition, *J. Alloys Compd.*, **492**, 488–495, (2010), doi: 10.1016/j.jallcom.2009.11.146.
- 99 Carter, C.B., Norton, M.G.: Ceramic materials: Science and engineering. Springer, New York, London, (2007).
- 100 Shackelford, J.F., Alexander, W.: CRC materials science and engineering handbook. 3rd edition. CRC Press, Boca Raton, FL, (2001).
- 101 Seto, N., Endo, K., Sakamoto, N., Hirose, S., Akedo, J.: Hard α -Al₂O₃ film coating on industrial roller using aerosol deposition method, *J. Therm. Spray Techn.*, **23**, 1373–1381, (2014), doi: 10.1007/s11666-014-0135-9.
- 102 Lebedev, M., Akedo, J., Ito, T.: Substrate heating effects on hardness of an α -Al₂O₃ thick film formed by aerosol deposition method, *J. Cryst. Growth*, **275**, e1301, (2005), doi: 10.1016/j.jcrysgro.2004.11.109.
- 103 Hatono, H., Ito, T., Iwata, K., Akedo, J.: Multilayer construction with various ceramic films for electronic devices fabricated by aerosol deposition, *Int. J. Appl. Ceram. Tec.*, **3**, 419–427, (2006), doi: 10.1111/j.1744-7402.2006.02109.x.
- 104 Lee, W.-H., Kim, H.-J., Lee, D.-W., Jeong, M.-G., Lim, D.-S., Nam, S.-M.: Al₂O₃-nanodiamond composite coatings with high durability and hydrophobicity prepared by aerosol deposition, *Surf. Coat. Tech.*, **206**, 4679–4684, (2012), doi: 10.1016/j.surfcoat.2012.05.052.
- 105 Sakamaki, R., Hoshina, T., Kakemoto, H., Yasuda, K., Takeda, H., Akedo, J., Tsurumi, T.: Heat-cycle endurance and in-plane thermal expansion of Al₂O₃/Al substrates formed by aerosol deposition method, *J. Ceram. Soc. Jpn.*, **116**, 1299–1303, (2008), doi: 10.2109/jcersj2.116.1299.
- 106 Cho, H.M., Kim, H.J.: Metal-core printed circuit board with alumina layer by aerosol deposition process, *IEEE Electron Device Lett.*, **29**, 991–993, (2008), doi: 10.1109/LED.2008.2001633.
- 107 Sato, Y., Uemichi, Y., Nishikawa, K., Yoshikado, S.: Fabrication of Al₂O₃ films using aerosol deposition method and their characterization, *IOP Conf. Ser.: Mater. Sci. Eng.*, **18**, 092056, (2011), doi: 10.1088/1757-899X/18/9/092056.
- 108 Nam, S.-M.: Aerosol deposition for electronic device application. In: 4th Tsukuba International Coatings Symposium, Frontiers of Coatings Technology: Innovative Processes and Applications, 2010, 9–10.
- 109 Lee, D.-W., Kim, H.-J., Nam, S.-M.: Effects of starting powder on the growth of Al₂O₃ films on cu substrates using the aerosol deposition method, *J. Korean Phys. Soc.*, **57**, 1115–1121, (2010), doi: 10.3938/jkps.57.1115.
- 110 Momotani, M., Mori, N., Nam, S.M., Kakemoto, H., Wada, S., Tsurumi, T., Akedo, J.: Fabrication of microstrip band pass filters in GHz region by aerosol deposition process, *Key Eng. Mater.*, **301**, 117–120, (2006), doi: 10.4028/www.scientific.net/KEM.301.117.
- 111 Lee, J.-W., Koh, J.-H.: Microwave band-pass filter with aerosol-deposited Al₂O₃-polytetrafluoroethylene composite thick films, *J. Nanosci. Nanotechnol.*, **15**, 2300–2304, (2015), doi: 10.1166/jnn.2015.10254.
- 112 Heywang, W., Lubitz, K., Wersing, W.: Piezoelectricity: Evolution and future of a technology. Springer, Berlin, (2008).
- 113 Akedo, J.: Microstructure of ceramic thick film formed by aerosol deposition and its applications to microactuator, *Integr. Ferroelectr.*, **80**, 55–65, (2006), doi: 10.1080/10584580600656221.
- 114 Liao, W.-H., Yeh, S.P., Wang, L.T., Wang, Y.J., Lin, S.C., Shih, Y.S., Wu, W.J.: Recent progress on micro-piezoelectric energy harvesters fabricated with aerosol deposition method and the interfacing circuits. In: SPIE Smart structures and materials + nondestructive evaluation and health monitoring: SPIE, San Diego, California, 2014, 90570M.
- 115 Akedo, J., Lebedev, M.: Effects of annealing and poling conditions on piezoelectric properties of Pb(Zr_{0.52}Ti_{0.48})O₃ thick films formed by aerosol deposition method, *J. Cryst. Growth*, **235**, 415–420, (2002), doi: 10.1016/S0022-0248(01)01925-X.
- 116 Kawakami, Y., Aisawa, S., Akedo, J.: Annealing effect on 0.5Pb(Ni_{1/3}Nb_{2/3})O₃-0.5Pb(Zr_{0.3}Ti_{0.7})O₃ thick film deposited by aerosol deposition method, *Jpn. J. Appl. Phys.*, **44**, 6934–6937, (2005), doi: 10.1143/JJAP.44.6934.
- 117 Baba, S., Akedo, J.: Damage-free and short annealing of Pb(Zr,Ti)O₃ thick films directly deposited on stainless steel sheet by aerosol deposition with CO₂ laser radiation, *J. Am. Ceram. Soc.*, **88**, 1407–1410, (2005), doi: 10.1111/j.1551-2916.2005.00269.x.
- 118 Nakada, M., Ohashi, K., Akedo, J.: Electro-optic properties of Pb(Zr_{1-x}Ti_x)O₃ (X = 0, 0.3, 0.6) films prepared by aerosol deposition, *Jpn. J. Appl. Phys.*, **44**, L1088, (2005), doi: 10.1143/JJAP.44.L1088.
- 119 Lebedev, M., Akedo, J.: What thickness of the piezoelectric layer with high breakdown voltage is required for the Microactuator?, *Jpn. J. Appl. Phys.*, **41**, 3344–3347, (2002), doi: 10.1143/JJAP.41.3344.
- 120 Miyoshi, T.: Preparation of full-dense Pb(Zr,Ti)O₃ ceramics by aerosol deposition, *J. Am. Ceram. Soc.*, **91**, 2098–2104, (2008), doi: 10.1111/j.1551-2916.2008.02422.x.

- 121 Lebedev, M., Akedo, J., Akiyama, Y.: Actuation properties of lead zirconate titanate thick films structured on si membrane by the aerosol deposition method, *Jpn. J. Appl. Phys.*, **39**, 5600–5603, (2000), doi: 10.1143/JJAP.39.5600.
- 122 Park, J.-H., Akedo, J.: Development of novel nanocomposite films by aerosol deposition. In: 4th Tsukuba International Coatings Symposium, Frontiers of Coatings Technology: Innovative Processes and Applications, 2010, 19–20.
- 123 Hahn, B.-D., Park, D.-S., Choi, J.-J., Yoon, W.-H., Ryu, J., Kim, D.-Y.: Effects of Zr/Ti ratio and post-annealing temperature on the electrical properties of lead zirconate titanate (PZT) thick films fabricated by aerosol deposition, *J. Mater. Res.*, **23**, 226–235, (2008), doi: 10.1557/JMR.2008.0021.
- 124 Miyoshi, T., Funakubo, H.: Effect of grain size on mechanical properties of full-dense Pb(Zr,Ti)O₃ ceramics, *Jpn. J. Appl. Phys.*, **49**, 09MD13, (2010), doi: 10.1143/JJAP.49.09MD13.
- 125 Kawakami, Y., Yoshikawa, H., Komagata, K., Akedo, J.: Powder preparation for 0.5 Pb(Ni_{1/3}Nb_{2/3})O₃-0.15 PbZrO₃-0.35PbTiO₃ thick films by the aerosol deposition method, *J. Cryst. Growth*, **275**, e1295, (2005), doi: 10.1016/j.jcrysgro.2004.11.103.
- 126 Jong-Jin Choi, Hahn, B.-D., Woon-Ha Yoon, Dong-Soo Park, Jungho Ryu: Highly dense and crack free 50- μ m-Thick PZN-PZT films by aerosol deposition method, 460–463, doi: 10.1109/ISAF.2007.4393298.
- 127 Miyoshi, T.: Evaluation of Pb(Zr,Ti)O₃ ceramics prepared by aerosol deposition, *Jpn. J. Appl. Phys.*, **46**, 7018–7023, (2007), doi: 10.1143/JJAP.46.7018.
- 128 Nakada, M., Ohashi, K., Akedo, J.: Dielectric characteristics of ferroelectric films prepared by aerosol deposition in THz range, *Jpn. J. Appl. Phys.*, **44**, 6918–6922, (2005), doi: 10.1143/JJAP.44.6918.
- 129 Baba, S., Akedo, J., Tsukamoto, M., Abe, N.: Effect of carrier gas species on ferroelectric properties of PZT/Stainless-steel fabricated by CO₂ laser-assisted aerosol deposition, *J. Am. Ceram. Soc.*, **89**, 1736–1738, (2006), doi: 10.1111/j.1551-2916.2006.00943.x.
- 130 Baba, S., Tsuda, H., Akedo, J.: Thickness dependence of electrical properties of PZT films deposited on metal substrates by laser-assisted aerosol deposition, *IEEE Trans. Ultrason., Ferroelect., Freq. Contr.*, **55**, 1009–1016, (2008), doi: 10.1109/TUFFC.2008.747.
- 131 Akedo, J., Lebedev, M.: Influence of carrier gas conditions on electrical and optical properties of Pb(Zr, Ti)O₃ thin films prepared by aerosol deposition method, *Jpn. J. Appl. Phys.*, **40**, 5528–5532, (2001), doi: 10.1143/JJAP.40.5528.
- 132 Han, G., Ryu, J., Yoon, W.-H., Choi, J.-J., Hahn, B.-D., Park, D.-S.: Effect of film thickness on the piezoelectric properties of lead zirconate titanate thick films fabricated by aerosol deposition, *J. Am. Ceram. Soc.*, **94**, 1509–1513, (2011), doi: 10.1111/j.1551-2916.2010.04276.x.
- 133 Choi, J.-J., Jang, J.-H., Hahn, B.-D., Park, D.-S., Yoon, W.-H., Ryu, J., Park, C.: Preparation of highly dense PZN-PZT thick films by the aerosol deposition method using excess-pbO powder, *J. Am. Ceram. Soc.*, **90**, 3389–3394, (2007), doi: 10.1111/j.1551-2916.2007.01901.x.
- 134 Damjanovic, D.: Ferroelectric, dielectric and piezoelectric properties of ferroelectric thin films and ceramics, *Rep. Prog. Phys.*, **61**, 1267–1324, (1998), doi: 10.1088/0034-4885/61/9/002.
- 135 Akedo, J., Lebedev, M., Baba, S.: Aerosol deposition method for preparation of lead zirconate titanate thick layer at low temperature – Improvement of electrical properties by irradiation of fast atom beam and Plasma –, *Jpn. J. Appl. Phys.*, **42**, 5931–5935, (2003), doi: 10.1143/JJAP.42.5931.
- 136 Tsuda, H., Nakada, M., Akedo, J., Ohashi, K.: Optical properties of Pb(Zr,Ti)O₃ films prepared by aerosol deposition, *IEEE Trans. Ultrason., Ferroelect., Freq. Contr.*, **55**, 975–979, (2008), doi: 10.1109/TUFFC.2008.742.
- 137 Iwanami, M., Nakada, M., Tsuda, H., Ohashi, K., Akedo, J.: Ultra small electro-optic field probe fabricated by aerosol deposition, *IEICE Electron. Express*, **4**, 26–32, (2007), doi: 10.1587/elex.4.26.
- 138 Nakada, M., Shimizu, T., Miyazaki, H., Tsuda, H., Akedo, J., Ohashi, K.: Lanthanum-modified lead zirconate titanate electro-optic modulators fabricated using aerosol deposition for LSI interconnects, *Jpn. J. Appl. Phys.*, **48**, 09KA06, (2009), doi: 10.1143/JJAP.48.09KA06.
- 139 Ohashi, K., Nishi, K., Shimizu, T., Nakada, M., Fujikata, J., Ushida, J., Torii, S., Nose, K., Mizuno, M., Yukawa, H.; *et al.*: On-chip optical interconnect, A silicon chip able to optically-perform desired signal interconnections has been bonded to a large-scale integrated silicon chip to provide cost-effective reduction of required interconnection power, *Proc. IEEE*, **97**, 1186–1198, (2009), doi: 10.1109/JPROC.2009.2020331.
- 140 Nakada, M., Ohashi, K., Lebedev, M., Akedo, J.: Electro-optical properties of (Pb, La)(Zr, Ti)O₃ films prepared by aerosol deposition method, *Jpn. J. Appl. Phys.*, **42**, 5960–5962, (2003), doi: 10.1143/JJAP.42.5960.
- 141 Shimizu, T., Nakada, M., Tsuda, H., Miyazaki, H., Akedo, J., Ohashi, K.: Gigahertz-rate optical modulation on mach-zehnder PLZT electro-optic modulators formed on silicon substrates by aerosol deposition, *IEICE Electron. Express*, **6**, 1669–1675, (2009), doi: 10.1587/elex.6.1669.
- 142 Ryu, J., Choi, J.-J., Hahn, B.-D., Yoon, W.-H., Lee, B.-K., Choi, J.H., Park, D.-S.: Pb(Zr,Ti)O₃-Pb(Mn_{1/3}Nb_{2/3})O₃ piezoelectric thick films by aerosol deposition, *Mater. Sci. Eng., B*, **170**, 67–70, (2010), doi: 10.1016/j.mseb.2010.02.028.
- 143 Oh, N.-K., Han, G., Yoon, W.-H., Choi, J.-J., Hahn, B.-D., Kim, J.-W., Ahn, C.-W., Choi, J.H., Park, D.-S., Kim, J.-J.; *et al.*: 2–2 structured magnetoelectric composites by aerosol deposition, *J. Am. Ceram. Soc.*, **95**, 855–858, (2012), doi: 10.1111/j.1551-2916.2011.05050.x.
- 144 Lee, B.S., Lin, S.C., Wu, W.J., Wang, X.Y., Chang, P.-Z., Lee, C.K.: Piezoelectric MEMS generators fabricated with an aerosol deposition PZT thin film, *J. Micromech. Microeng.*, **19**, 065014, (2009), doi: 10.1088/0960-1317/19/6/065014.
- 145 Miyoshi, T.: Preparation of multilayer piezoelectric device by aerosol deposition using a novel detachment method, *J. Ceram. Soc. Jpn.*, **117**, 899–903, (2009), doi: 10.2109/jcersj2.117.899.
- 146 Park, J.-H., Akedo, J., Lebedev, M., Sato, H.: Optical scanning devices based on PZT thick films formed by aerosol deposition method, Brisbane, Australia, January 03, 2006, *Proc SPIE 6037*, (2006), doi: 10.1117/12.638489
- 147 Asai, N., Matsuda, R., Watanabe, M., Takayama, H., Yamada, S., Mase, A., Shikida, M., Sato, K., Lebedev, M., Akedo, J.: A novel high resolution optical scanner actuated by aerosol deposited PZT films, Kyoto, Japan, January 19–23, 2003, *Proc. IEEE*, (2003), doi: 10.1109/MEMSYS.2003.1189732.
- 148 Akedo, J., Lebedev, M.: Aerosol deposition for fabrication of high speed optical micro-scanner, *Advances in Dielectric Materials and Electronic Devices*, **174**, 99–106, (2006), doi: 10.1002/9781118408162.ch11.
- 149 Park, J.-H., Akedo, J., Lebedev, M., Sato, H., Chiao, J.-C., Dzurak, A.S., Jagadish, C., Thiel, D.V.: Optical scanning devices based on PZT thick films formed by aerosol deposition method. In: Proc. SPIE 6037, Device and Process Technologies for Microelectronics, MEMS, and Photonics IV, Brisbane, Australia, 2006, 60371S.
- 150 Park, J.-H., Akedo, J.: Fabrication and scanning-angle temperature dependence of metal-based, optical resonant scanners with PZT actuation, *IEEE Trans. Ultrason., Ferroelect., Freq. Contr.*, **55**, 942–945, (2008), doi: 10.1109/TUFFC.2008.736.
- 151 Kim, H.-K., Lee, S.-H., Kim, S.I., Woo Lee, C., Rag Yoon, J., Lee, S.-G., Lee, Y.-H.: Dielectric strength of voidless BaTiO₃

- films with nano-scale grains fabricated by aerosol deposition, *J. Appl. Phys.*, **115**, 014101, (2014), doi: 10.1063/1.4851675.
- 152 Oh, J.-M., Nam, S.-M.: Thickness limit of BaTiO₃ thin film capacitors grown on SUS substrates using aerosol deposition method, *Thin Solid Films*, **518**, 6531–6536, (2010), doi: 10.1016/j.tsf.2010.03.159.
- 153 Oh, J.-M., Nam, S.-M.: Possibility of BaTiO₃ thin films prepared on Cu substrates for embedded decoupling capacitors by an aerosol deposition method, *J. Ceram. Process. Res.*, **10**, 674–678, (2009).
- 154 Imanaka, Y., Akedo, J.: Embedded capacitor technology using aerosol deposition, *Int. J. Appl. Ceram. Tec.*, **7**, E23–E32, (2010), doi: 10.1111/j.1744-7402.2009.02359.x.
- 155 Imanaka, Y., Hayashi, N., Takenouchi, M., Akedo, J.: Aerosol deposition for post-LTCC, *J. Eur. Ceram. Soc.*, **27**, 2789–2795, (2007), doi: 10.1016/j.jeurceramsoc.2006.11.055.
- 156 Imanaka, Y., Amada, H., Kumasaka, E.: Dielectric and insulating properties of embedded capacitor for flexible electronics prepared by aerosol-type nanoparticle deposition, *Jpn. J. Appl. Phys.*, **52**, 05DA02, (2013), doi: 10.7567/JJAP.52.05DA02.
- 157 Imanaka, Y.: Aerosol deposition technology for microelectronic packaging. In: 4th Tsukuba International Coatings Symposium, Frontiers of Coatings Technology: Innovative Processes and Applications, 2010, 13–14.
- 158 Wang, C., Sung, H.K., Kim, N.Y.: Aerosol deposition-based micropatterning of barium titanate via sulphur hexafluoride inductively coupled plasma etching, *Vacuum*, **114**, 49–53, (2015), doi: 10.1016/j.vacuum.2014.12.028.
- 159 Hoshina, T., Furuta, T., Kigoshi, Y., Hatta, S., Horiuchi, N., Takeda, H., Tsurumi, T.: Size effect of nanograined BaTiO₃ ceramics fabricated by aerosol deposition method, *Jpn. J. Appl. Phys.*, **49**, 09MC02, (2010), doi: 10.1143/JJAP.49.09MC02.
- 160 Arlt, G., Hennings, D., With, G. de: Dielectric properties of fine-grained barium titanate ceramics, *J. Appl. Phys.*, **58**, 1619–1625, (1985), doi: 10.1063/1.336051.
- 161 Furuta, T., Hatta, S., Kigoshi, Y., Hoshina, T., Takeda, H., Tsurumi, T.: Dielectric properties of nanograined BaTiO₃ ceramics fabricated by aerosol deposition method, *Key Eng. Mater.*, **485**, 183–186, (2011), doi: 10.4028/www.scientific.net/KEM.485.183.
- 162 Oh, J.-M., Kim, H.-J., Nam, S.-M.: Characterization of leakage current mechanisms for Aerosol-deposited BaTiO₃ thin films at room temperature, *J. Korean Phys. Soc.*, **57**, 1096, (2010), doi: 10.3938/jkps.57.1096.
- 163 Kim, H.-K., Oh, J.-M., Kim, S.I., Kim, H.-J., Lee, C., Nam, S.-M.: Relation between electrical properties of aerosol-deposited BaTiO₃ thin films and their mechanical hardness measured by nano-indentation, *Nanoscale Res. Lett.*, **7**, 264, (2012), doi: 10.1186/1556-276X-7-264.
- 164 Oh, J., Kim, N., Choi, S., Nam, S.: Thickness dependence of dielectric properties in BaTiO₃ films fabricated by aerosol deposition method, *Mater. Sci. Eng., B*, **161**, 80–84, (2009), doi: 10.1016/j.mseb.2009.01.028.
- 165 Jong-Min, O., Song-Min, N.: Causes arising high leakage currents in thin BaTiO₃ films prepared by aerosol deposition method, *J. Korean Phys. Soc.*, **56**, 448, (2010), doi: 10.3938/jkps.56.448.
- 166 Hitosugi, T., Yamada, N., Nakao, S., Hirose, Y., Hasegawa, T.: Properties of TiO₂-based transparent conducting oxides, *Phys. Status Solidi A*, **207**, 1529–1537, (2010), doi: 10.1002/pssa.200983774.
- 167 Madelung, O., Rössler, U., Schulz, M.: Semiconductors. Springer, Berlin, (2006).
- 168 O'Regan, B., Grätzel, M.: A low-cost, high-efficiency solar cell based on dye-sensitized colloidal TiO₂ films, *Nature*, **353**, 737–740, (1991), doi: 10.1038/353737a0.
- 169 Beydoun, D., Amal, R., Low, G.K.-C., McEvoy, S.: Novel Photocatalyst: titania-coated Magnetite. activity and photodissolution, *J. Phys. Chem. B*, **104**, 4387–4396, (2000), doi: 10.1021/jp992088c.
- 170 Kim, D.-Y., Park, J.-J., Lee, J.-G., Lee, M.-W., Kim, H.-Y., Oh, J.-H., Seong, T.-Y., Kim, D., James, S.C., van Hest, M.F.A.M.; et al.: Tuning hydrophobicity with honeycomb surface structure and hydrophilicity with CF₄ plasma etching for aerosol-deposited titania films, *J. Am. Ceram. Soc.*, **95**, 3955–3961, (2012), doi: 10.1111/jace.12021.
- 171 Park, J.-J., Kim, D.-Y., Lee, J.-G., Kim, D., Oh, J.-H., Seong, T.-Y., van Hest, M.F., Yoon, S.S.: Superhydrophilic transparent titania films by supersonic aerosol deposition, *J. Am. Ceram. Soc.*, **96**, 1596–1601, (2013), doi: 10.1111/jace.12164.
- 172 Park, J.-J., Kim, D.-Y., Latthe, S.S., Lee, J.-G., Swihart, M.T., Yoon, S.S.: Thermally induced superhydrophilicity in TiO₂ films prepared by supersonic aerosol deposition, *ACS Appl. Mater. Interfaces*, **5**, 6155–6160, (2013), doi: 10.1021/am401083y.
- 173 Sahner, K., Kaspar, M., Moos, R.: Assessment of the novel aerosol deposition method for room temperature preparation of metal oxide gas sensor films, *Sens. Actuators, B*, **139**, 394–399, (2009), doi: 10.1016/j.snb.2009.03.011.
- 174 Tsukamoto, M., Abe, N., Soga, Y., Yoshida, M., Nakano, H., Fujita, M., Akedo, J.: Control of electrical resistance of TiO₂ films by short-pulse laser irradiation, *Appl. Phys. A: Mater. Sci. Process.*, **93**, 193–196, (2008), doi: 10.1007/s00339-008-4713-x.
- 175 Shinonaga, T.: Control of electrical resistance and temperature of titanium dioxide film by local heating with CW fiber laser, *J. Laser Micro/Nanoeng.*, **9**, 204–208, (2014), doi: 10.2961/jlmn.2014.03.0004.
- 176 Kim, J.O., Choi, W.Y., Choi, B.K., Jeong, J.T.: Fabrication of photocatalytic TiO₂ thin film using innovative aerosol deposition method, *Mater. Sci. Forum*, **510–511**, 1–4, (2006), doi: 10.4028/www.scientific.net/MSF.510-511.1.
- 177 Cho, S.H., Yoon, Y.J.: Multi-layer TiO₂ films prepared by aerosol deposition method for dye-sensitized solar cells, *Thin Solid Films*, **547**, 91–94, (2013), doi: 10.1016/j.tsf.2013.04.107.
- 178 Heo, J., Sudhagar, P., Park, H., Cho, W., Kang, Y.S., Lee, C.: Room temperature synthesis of highly compact TiO₂ coatings by vacuum kinetic spraying to serve as a blocking layer in polymer electrolyte-based dye-sensitized solar cells, *J. Therm. Spray Techn.*, **24**, 328–337, (2015), doi: 10.1007/s11666-014-0204-0.
- 179 Ryu, H.S., Park, D.-S., Hong, S.-H.: Improved corrosion protection of AZ31 magnesium alloy through plasma electrolytic oxidation and aerosol deposition duplex treatment, *Surf. Coat. Techn.*, **219**, 82–87, (2013), doi: 10.1016/j.surfcoat.2013.01.008.
- 180 Park, J.-J., Kim, D.-Y., Lee, J.-G., Cha, Y.-H., Swihart, M.T., Yoon, S.: Supersonic aerosol-deposited TiO₂ photoelectrodes for photoelectrochemical solar water splitting, *RSC Adv.*, **4**, 8661–8670, (2014), doi: 10.1039/C3RA47998F.
- 181 Choi, J.-J., Ryu, J., Hahn, B.-D., Yoon, W.-H., Lee, B.-K., Choi, J.-H., Park, D.-S.: Ni-containing conducting ceramic as an oxidation protective coating on metallic interconnects by aerosol deposition, *J. Am. Ceram. Soc.*, (2010), doi: 10.1111/j.1551-2916.2010.03646.x.
- 182 Huang, J.-J., Fu, Y.-P., Wang, J.-Y., Cheng, Y.-N., Lee, S., Hsu, J.-C.: Characterization of Fe-Cr alloy metallic interconnects coated with LSMO using the aerosol deposition process, *Mater. Res. Bull.*, **51**, 63–68, (2013), doi: 10.1016/j.materresbull.2013.11.058.
- 183 Choi, J.-J., Lee, J.-H., Park, D.-S., Hahn, B.-D., Yoon, W.-H., Lin, H.-T.: Oxidation resistance coating of LSM and LSCF on SOFC metallic interconnects by the aerosol deposition process, *J. Am. Ceram. Soc.*, **90**, 1926–1929, (2007), doi: 10.1111/j.1551-2916.2007.01641.x.

- 184 Choi, J.-J., Park, D.-S., Hahn, B.-D., Ryu, J., Yoon, W.-H.: Oxidation behavior of ferritic steel alloy coated with highly dense conducting ceramics by aerosol deposition, *J. Am. Ceram. Soc.*, **91**, 2601–2606, (2008), doi: 10.1111/j.1551-2916.2008.02506.x.
- 185 Choi, J.-J., Ryu, J., Hahn, B.-D., Yoon, W.-H., Lee, B.-K., Park, D.-S.: Dense spinel MnCo_2O_4 film coating by aerosol deposition on ferritic steel alloy for protection of chromic evaporation and low-conductivity scale formation, *J. Mater. Sci.*, **44**, 843–848, (2009), doi: 10.1007/s10853-008-3132-x.
- 186 Jung, J.-H., Hahn, B.-D., Yoon, W.-H., Park, D.-S., Choi, J.-J., Ryu, J., Kim, J.-W., Ahn, C.-W., Song, K.-M.: Halogen plasma erosion resistance of rare earth oxide films deposited on plasma sprayed alumina coating by aerosol deposition, *J. Eur. Ceram. Soc.*, **32**, 2451–2457, (2012), doi: 10.1016/j.jeurceramsoc.2012.02.019.
- 187 Ryu, H.S., Lim, T.S., Ryu, J., Hong, S.-H.: Corrosion protection performance of YSZ coating on AA7075 aluminum alloy prepared by aerosol deposition, *J. Electrochem. Soc.*, **160**, C42, (2012), doi: 10.1149/2.038302jes.
- 188 Ryu, H.S., Ryu, J., Park, D.-S., Hong, S.-H.: Electrochemical corrosion properties of nanostructured YSZ coated AZ31 magnesium alloy prepared by aerosol deposition, *J. Electrochem. Soc.*, **158**, C23, (2011), doi: 10.1149/1.3525271.
- 189 Hahn, B.-D., Park, D.-S., Choi, J.-J., Ryu, J., Yoon, W.-H., Lee, B.-K., Kim, H.-E.: Effect of the HA/ β -TCP Ratio on the Biological Performance of Calcium Phosphate Ceramic Coatings Fabricated by a Room-Temperature Powder Spray in Vacuum, *J. Am. Ceram. Soc.*, **92**, 793–799, (2009), doi: 10.1111/j.1551-2916.2009.02949.x.
- 190 Kim, S.W., Seo, D.S., Lee, J.K.: Fabrication of xenogenic bone-derived hydroxyapatite thin film by aerosol deposition method, *Appl. Surf. Sci.*, **255**, 388–390, (2008), doi: 10.1016/j.apsusc.2008.06.084.
- 191 Hahn, B.-D., Park, D.-S., Choi, J.-J., Ryu, J., Yoon, W.-H., Kim, K.-H., Park, C., Kim, H.-E.: Dense nanostructured hydroxyapatite coating on titanium by aerosol deposition, *J. Am. Ceram. Soc.*, **92**, 683–687, (2009), doi: 10.1111/j.1551-2916.2008.02876.x.
- 192 Hahn, B.-D., Lee, J.-M., Park, D.-S., Choi, J.-J., Ryu, J., Yoon, W.-H., Lee, B.-K., Shin, D.-S., Kim, H.-E.: Aerosol deposition of silicon-substituted hydroxyapatite coatings for biomedical applications, *Thin Solid Films*, **518**, 2194–2199, (2010), doi: 10.1016/j.tsf.2009.09.024.
- 193 Hahn, B.-D., Cho, Y.-L., Park, D.-S., Choi, J.-J., Ryu, J., Kim, J.-W., Ahn, C.-W., Park, C., Kim, H.-E., Kim, S.-G.: Effect of fluorine addition on the biological performance of hydroxyapatite coatings on ti by aerosol deposition, *J. Biomater. Appl.*, **27**, 587–594, (2012), doi: 10.1177/0885328211415723.
- 194 Kitajima, A., Tsukamoto, M., Akedo, J.: Hydroxyapatite film coated on poly-L-lactic acid by aerosol deposition method, *J. Ceram. Soc. Jpn.*, **118**, 417–420, (2010), doi: 10.2109/jcersj2.118.417.
- 195 Seo, D.S., Chae, H.C., Lee, J.K.: Fabrication and microstructure of hydroxyapatite coatings on zirconia by room temperature spray process, *J. Nanosci. Nanotechn.*, **15**, 6039–6043, (2015), doi: 10.1166/jnn.2015.10440.
- 196 Sugimoto, S., Maeda, T., Kobayashi, R., Akedo, J., Lebedev, M., Inomata, K.: Magnetic properties of sm-fe-N thick film magnets prepared by the aerosol deposition method, *IEEE Trans. Magn.*, **39**, 2986–2988, (2003), doi: 10.1109/TMAG.2003.816715.
- 197 Maki, T., Sugimoto, S., Kagotani, T., Inomata, K., Akedo, J.: Microstructure and magnetic properties of aerosol-deposited sm-fe-N thick films, *Electr. Eng. Jpn.*, **158**, 8–13, (2007), doi: 10.1002/eej.20214.
- 198 Maki, T., Sugimoto, S., Kagotani, T., Inomata, K., Akedo, J.: Microstructures and magnetic properties of sm-fe-N thick films produced by the aerosol deposition method, *Mater. Trans.*, **45**, 369–372, (2004)2004, doi: 10.2320/mater-trans.45.369.
- 199 Sugimoto, S., Akedo, J., Lebedev, M., Inomata, K.: Magnetic properties and microstructures of the aerosol-deposited permanent magnet films, *J. Magn. Magn. Mater.*, **272–276**, E1881, (2004), doi: 10.1016/j.jmmm.2003.12.607.
- 200 Sugimoto, S., Maki, T., Kagotani, T., Akedo, J., Inomata, K.: Effect of applied field during aerosol deposition on the anisotropy of Sm-Fe-N thick films, *J. Magn. Magn. Mater.*, **290–291**, 1202–1205, (2005), doi: 10.1016/j.jmmm.2004.11.385.
- 201 Maki, T., Sugimoto, S., Kagotani, T., Inomata, K., Akedo, J.: Effect of applied magnetic field on magnetic properties of sm-fe-N films prepared by aerosol deposition method, *Mater. Trans.*, **45**, 2626–2629, (2004), doi: 10.2320/mater-trans.45.2626.
- 202 Lebedev, M., Akedo, J., Iwata, A., Sugimoto, S., Inomata, K.: NiZnCu ferrite thick film with nano scale crystallites formed by the aerosol deposition method, *J. Am. Ceram. Soc.*, **87**, 1621–1624, (2004), doi: 10.1111/j.1551-2916.2004.01621.x.
- 203 Kagotani, T., Kobayashi, R., Sugimoto, S., Inomata, K., Okayama, K., Akedo, J.: Magnetic properties and microwave characteristics of Ni-Zn-Cu ferrite film fabricated by aerosol deposition method, *J. Magn. Magn. Mater.*, **290–291**, 1442–1445, (2005), doi: 10.1016/j.jmmm.2004.11.543.
- 204 Sugimoto, S., Haga, K., Nakata, M., Kagotani, T., Inomata, K., Akedo, J.: Magnetic properties of Fe/(NiZnCu)Fe₂O₄ composite films prepared by aerosol deposition method, *IEEE Trans. Magn.*, **41**, 3460–3462, (2005), doi: 10.1109/TMAG.2005.854880.
- 205 Kato, Y., Sugimoto, S., Akedo, J.: Magnetic properties and electromagnetic wave suppression properties of Fe-Ferrite films prepared by aerosol deposition method, *Jpn. J. Appl. Phys.*, **47**, 2127–2131, (2008), doi: 10.1143/JJAP.47.2127.
- 206 Moos, R., Sahner, K., Fleischer, M., Guth, U., Barsan, N., Weimar, U.: Solid state gas sensor research in germany - a status report, *Sensors*, **9**, 4323–4365, (2009), doi: 10.3390/s90604323.
- 207 Moos, R.: Catalysts as sensors-a promising novel approach in automotive exhaust gas aftertreatment, *Sensors*, **10**, 6773–6787, (2010), doi: 10.3390/s100706773.
- 208 Fraden, J.: Handbook of modern sensors: Physics, designs, and applications, 4th edition. Springer, New York, 2010.
- 209 Bektas, M., Hanft, D., Schönauer-Kamin, D., Stöcker, T., Hagen, G., Moos, R.: Aerosol-deposited BaFe_{0.7}Ta_{0.3}O_{3- δ} for nitrogen monoxide and temperature-independent oxygen sensing, *J. Sens. Sens. Syst.*, **3**, 223–229, (2014), doi: 10.5194/jsss-3-223-2014.
- 210 Hsiao, C.-C., Luo, L.-S.: A rapid process for fabricating gas sensors, *Sensors*, **14**, 12219–12232, (2014), doi: 10.3390/s140712219.
- 211 Feteira, A.: Negative temperature coefficient resistance (NTCR) ceramic Thermistors: an industrial perspective, *J. Am. Ceram. Soc.*, **92**, 967–983, (2009), doi: 10.1111/j.1551-2916.2009.02990.x.
- 212 Ryu, J., Park, D.-S., Schmidt, R.: In-plane impedance spectroscopy in aerosol deposited NiMn₂O₄ negative temperature coefficient thermistor films, *J. Appl. Phys.*, **109**, 113722, (2011), doi: 10.1063/1.3592300.
- 213 Ryu, J., Kim, K.-Y., Choi, J.-J., Hahn, B.-D., Yoon, W.-H., Lee, B.-K., Park, D.-S., Park, C.: Highly dense and nanograined NiMn₂O₄ negative temperature coefficient thermistor thick films fabricated by aerosol-deposition, *J. Am. Ceram. Soc.*, **92**, 3084–3087, (2009), doi: 10.1111/j.1551-2916.2009.03300.x.

- 214 Ryu, J., Han, G., Lee, J.-P., Lim, Y.-S., Park, D.-S., Jeong, D.-Y.: Co and Fe doping effect on negative temperature coefficient characteristics of nano-grained NiMn_2O_4 thick films fabricated by aerosol-deposition, *J. Nanosci. Nanotechnol.*, **13**, 3422–3426, (2013), doi: 10.1166/jnn.2013.7232.
- 215 Hsiao, C.-C., Liu, S.-Y.: Multi-frequency band pyroelectric sensors, *Sensors*, **14**, 22180–22198, (2014), doi: 10.3390/s141222180.
- 216 Kambale, R.C., Patil, D., Ryu, J., Chai, Y.S., Kim, K.H., Yoon, W.-H., Jeong, D.-Y., Park, D.-S., Kim, J.-W., Choi, J.-J.; et al.: Colossal magnetoelectric response of PZT thick films on Ni substrates with a conductive LaNiO_3 electrode, *J. Phys. D: Appl. Phys.*, **46**, 092002, (2013), doi: 10.1088/0022-3727/46/9/092002.
- 217 Jacobson, A.J.: Materials for solid oxide fuel cells †, *Chem. Mater.*, **22**, 660–674, (2010), doi: 10.1021/cm902640j.
- 218 Menzler, N.H., Tietz, F., Uhlenbruck, S., Buchkremer, H.P., Stöver, D.: Materials and manufacturing technologies for solid oxide fuel cells, *J. Mater. Sci.*, **45**, 3109–3135, (2010), doi: 10.1007/s10853-010-4279-9.
- 219 Bae, H., Choi, J., Kim, K.J., Park, D., Choi, G.M.: Low-temperature fabrication of protonic ceramic fuel cells with $\text{BaZr}_{0.8}\text{Y}_{0.2}\text{O}_{3-\delta}$ electrolytes coated by aerosol deposition method, *Int. J. Hydrogen Energ.*, **40**, 2775–2784, (2015), doi: 10.1016/j.ijhydene.2014.12.046.
- 220 Choi, J.-J., Ryu, J., Hahn, B.-D., Ahn, C.-W., Kim, J.-W., Yoon, W.-H., Park, D.-S.: Low temperature preparation and characterization of solid oxide fuel cells on FeCr-based alloy support by aerosol deposition, *Int. J. Hydrogen Energ.*, **39**, 12878–12883, (2014), doi: 10.1016/j.ijhydene.2014.06.070.
- 221 Choi, J.-J., Choi, J.-H., Ryu, J., Hahn, B.-D., Kim, J.-W., Ahn, C.-W., Yoon, W.-H., Park, D.-S.: Microstructural evolution of YSZ electrolyte aerosol-deposited on porous NiO-YSZ , *J. Eur. Ceram. Soc.*, **32**, 3249–3254, (2012), doi: 10.1016/j.jeurceramsoc.2012.04.024.
- 222 Choi, J.-J., Cho, K.-S., Choi, J.-H., Ryu, J., Hahn, B.-D., Kim, J.-W., Ahn, C.-W., Yoon, W.-H., Yun, J., Park, D.-S.: Effects of annealing temperature on solid oxide fuel cells containing $(\text{La,Sr})(\text{Ga,Mg,Co})\text{O}_{3-\delta}$ electrolyte prepared by aerosol deposition, *Mater. Lett.*, **70**, 44–47, (2012), doi: 10.1016/j.matlet.2011.11.103.
- 223 Wang, S.-F., Hsu, Y.-F., Wang, C.-H., Yeh, C.-T.: Solid oxide fuel cells with $\text{Sm}_{0.2}\text{Ce}_{0.8}\text{O}_{2-\delta}$ electrolyte film deposited by novel aerosol deposition method, *J. Power Sources*, **196**, 5064–5069, (2011), doi: 10.1016/j.jpowsour.2011.01.083.
- 224 Choi, J.-J., Choi, J.-H., Ryu, J., Hahn, B.-D., Kim, J.-W., Ahn, C.-W., Yoon, W.-H., Park, D.-S.: Low-temperature fabrication of nano-structured porous $(\text{La,Sr})(\text{Co,Fe})\text{O}_{3-\delta}$ cathodes by aerosol deposition, *J. Alloys Compd.*, **545**, 186–189, (2012), doi: 10.1016/j.jallcom.2012.08.060.
- 225 Hayner, C.M., Zhao, X., Kung, H.H.: Materials for rechargeable lithium-ion batteries, *Annual review of chemical and biomolecular engineering*, **3**, 445–471, (2012), doi: 10.1146/annurev-chembioeng-062011-081024.
- 226 Etacheri, V., Marom, R., Elazari, R., Salitra, G., Aurbach, D.: Challenges in the development of advanced Li-ion batteries: a review, *Energ. Environ. Sci.*, **4**, 3243, (2011), doi: 10.1039/c1ee01598b.
- 227 Popovici, D., Nagai, H., Fujishima, S., Akedo, J.: Introduction of Aerosol Deposition Technique in All-solid-state Li-ion Battery Research. In: 4th Tsukuba International Coatings Symposium, Frontiers of Coatings Technology: Innovative Processes and Applications, 2010, 25–26.
- 228 Goriparti, S., Miele, E., Angelis, F. de, Di Fabrizio, E., Proietti Zaccaria, R., Capiglia, C.: Review on recent progress of nanostructured anode materials for Li-ion batteries, *J. Power Sources*, **257**, 421–443, (2014), doi: 10.1016/j.jpowsour.2013.11.103.
- 229 Usui, H., Shibata, M., Nakai, K., Sakaguchi, H.: Anode properties of thick-film electrodes prepared by gas deposition of Ni-coated Si particles, *J. Power Sources*, **196**, 2143–2148, (2011), doi: 10.1016/j.jpowsour.2010.10.013.
- 230 Usui, H., Nouno, K., Takemoto, Y., Nakada, K., Ishii, A., Sakaguchi, H.: Influence of mechanical grinding on lithium insertion and extraction properties of iron silicide/silicon composites, *J. Power Sources*, **268**, 848–852, (2014), doi: 10.1016/j.jpowsour.2014.06.105.
- 231 Usui, H., Uchida, N., Sakaguchi, H.: Influence of order in stepwise electroless deposition on anode properties of thick-film electrodes consisting of Si particles coated with Ni and Cu, *J. Power Sources*, **196**, 10244–10248, (2011), doi: 10.1016/j.jpowsour.2011.08.018.
- 232 Usui, H., Wasada, K., Shimizu, M., Sakaguchi, H.: TiO_2/Si composites synthesized by sol-gel method and their improved electrode performance as Li-ion battery anodes, *Electrochim. Acta*, **111**, 575–580, (2013), doi: 10.1016/j.electacta.2013.08.015.
- 233 Usui, H., Uchida, N., Sakaguchi, H.: Improved anode performance of Ni-P-coated Si thick-film electrodes for Li-ion battery, *Electrochemistry*, **80**, 737–739, (2012), doi: 10.5796/electrochemistry.80.737.
- 234 Iida, T., Hirono, T., Shibamura, N., Sakaguchi, H.: $\text{Mg}_2\text{Ge}/\text{Si}$ composite electrodes prepared by gas-deposition as anodes for lithium rechargeable battery, *Electrochemistry*, **76**, 644–648, (2008), doi: 10.5796/electrochemistry.76.644.
- 235 Usui, H., Kashiwa, Y., Iida, T., Sakaguchi, H.: Anode properties of Ru-coated Si thick film electrodes prepared by gas-deposition, *J. Power Sources*, **195**, 3649–3654, (2010), doi: 10.1016/j.jpowsour.2009.12.072.
- 236 Usui, H., Nishinami, H., Iida, T., Sakaguchi, H.: Anode properties of Cu-coated Si thick film electrodes prepared by electroless deposition and gas-deposition, *Electrochemistry*, **78**, 329–331, (2010), doi: 10.5796/electrochemistry.78.329.
- 237 Usui, H., Kiri, Y., Sakaguchi, H.: Effect of carrier gas on anode performance of Si thick-film electrodes prepared by gas-deposition method, *Thin Solid Films*, **520**, 7006–7010, (2012), doi: 10.1016/j.tsf.2012.07.093.
- 238 Ahn, C.-W., Choi, J.-J., Ryu, J., Hahn, B.-D., Kim, J.-W., Yoon, W.-H., Choi, J.-H., Park, D.-S.: Microstructure and electrochemical properties of iron oxide film fabricated by aerosol deposition method for lithium ion battery, *J. Power Sources*, **275**, 336–340, (2015), doi: 10.1016/j.jpowsour.2014.11.033.
- 239 Inada, R., Shibukawa, K., Masada, C., Nakanishi, Y., Sakurai, Y.: Characterization of as-deposited $\text{Li}_4\text{Ti}_5\text{O}_{12}$ thin film electrode prepared by aerosol deposition method, *J. Power Sources*, **253**, 181–186, (2014), doi: 10.1016/j.jpowsour.2013.12.084.
- 240 Ahn, C.-W., Choi, J.-J., Ryu, J., Hahn, B.-D., Kim, J.-W., Yoon, W.-H., Choi, J.-H., Park, D.-S.: Microstructure and electrochemical properties of graphite and C-coated LiFePO_4 films fabricated by aerosol deposition method for Li ion battery, *Carbon*, **82**, 135–142, (2015), doi: 10.1016/j.carbon.2014.10.043.
- 241 Ahn, C.-W., Choi, J.-J., Ryu, J., Hahn, B.-D., Kim, J.-W., Yoon, W.-H., Choi, J.-H., Lee, J.-S., Park, D.-S.: Electrochemical properties of $\text{Li}_7\text{La}_3\text{Zr}_2\text{O}_{12}$ -based solid state battery, *J. Power Sources*, **272**, 554–558, (2014), doi: 10.1016/j.jpowsour.2014.08.110.
- 242 Kim, I., Park, J., Nam, T.-H., Kim, K.-W., Ahn, J.-H., Park, D.-S., Ahn, C.-W., Wang, G., Ahn, H.-J.: Electrochemical properties of an as-deposited LiFePO_4 thin film electrode prepared by aerosol deposition, *J. Power Sources*, **244**, 646–651, (2013), doi: 10.1016/j.jpowsour.2012.12.108.
- 243 Iwasaki, S., Hamanaka, T., Yamakawa, T., West, W.C., Yamamoto, K., Motoyama, M., Hirayama, T., Iriyama, Y.: Preparation of thick-film $\text{LiNi}_{1/3}\text{Co}_{1/3}\text{Mn}_{1/3}\text{O}_2$ electrodes

- by aerosol deposition and its application to all-solid-state batteries, *J. Power Sources*, **272**, 1086–1090, (2014), doi: 10.1016/j.jpowsour.2014.09.038.
- ²⁴⁴ Kim, I., Nam, T.-H., Kim, K.-W., Ahn, J.-H., Park, D.-S., Ahn, C.-W., Chun, B., Wang, G., Ahn, H.-J.: Li-Ni_{0.4}Co_{0.3}Mn_{0.3}O₂ thin film electrode by aerosol deposition, *Nanoscale Res. Lett.*, **7**, 64, (2012), doi: 10.1186/1556-276X-7-64.
- ²⁴⁵ Popovici, D., Nagai, H., Fujishima, S., Akedo, J.: Preparation of lithium aluminum titanium phosphate electrolytes thick films by aerosol deposition method, *J. Am. Ceram. Soc.*, **94**, 3847–3850, (2011), doi: 10.1111/j.1551-2916.2011.04551.x.
- ²⁴⁶ Khan, A., Ahn, C.-W., Ryu, J., Yoon, W.-H., Hahn, B.-D., Choi, J.-J., Kim, J.-W., Park, D.-S.: Effect of annealing on properties of lithium aluminum germanium phosphate electrolyte thick films prepared by aerosol deposition, *Met. Mater. Int.*, **20**, 399–404, (2014), doi: 10.1007/s12540-014-1018-9.
- ²⁴⁷ Ahn, C.-W., Choi, J.-J., Ryu, J., Hahn, B.-D., Kim, J.-W., Yoon, W.-H., Choi, J.-H., Park, D.-S.: Microstructure and ionic conductivity in Li₇La₃Zr₂O₁₂ film prepared by aerosol deposition method, *J. Electrochem. Soc.*, **162**, A60, (2014), doi: 10.1149/2.0411501jes.
- ²⁴⁸ Esaka, T., Sakaguchi, H., Miyashita, Y.: High rate performance of Aerosol-deposited Mg₂Ge alloy anode in lithium batteries, *Electrochemistry*, **78**, 611–614, (2010), doi: 10.5796/electrochemistry.78.611.
- ²⁴⁹ Sakaguchi, H., Toda, T., Nagao, Y., Esaka, T.: Anode properties of lithium storage alloy electrodes prepared by gas-deposition, *Electrochem. Solid-State Lett.*, **10**, J146, (2007), doi: 10.1149/1.2772409.
- ²⁵⁰ Nakada, M., Akedo, J.: Optical element, integrated optic device and optical information transmission system. U.S. Patent 7,920,769, (2007).
- ²⁵¹ Akedo, J., Popovici, D., Hideyuki, N.: Solid electrolyte material, all-solid-state battery and method for producing solid electrolyte material. WO Patent Application 2013/108795, (2013).
- ²⁵² Akedo, J., Yoshihiko, I.: Semiconductor device and method of producing the same. U.S. Patent 8,278,217, (2005).
- ²⁵³ Akedo, J., Motohiro, Y.: Method of producing composite material, method of producing piezoelectric actuator, method of producing ink-jet head, and piezoelectric actuator. U.S. Patent 7,771,780, (2006).
- ²⁵⁴ Akedo, J.: Current status of aerosol deposition technology. In: 4th Tsukuba International Coatings Symposium, Frontiers of Coatings Technology: Innovative Processes and Applications, 2010, 5–6.
- ²⁵⁵ Baba, S., Sato, H., Huang, L., Uritani, A., Funahashi, R., Akedo, J.: Formation and characterization of polyethylene terephthalate-based (Bi_{0.15}Sb_{0.85})₂Te₃ thermoelectric modules with CoSb₃ adhesion layer by aerosol deposition, *J. Alloy Compd.*, **589**, 56–60, (2014), doi: 10.1016/j.jallcom.2013.11.180.
- ²⁵⁶ Baba, S., Huang, L., Sato, H., Funahashi, R., Akedo, J.: Room-temperature fast deposition and characterization of nanocrystalline Bi_{0.4}Sb_{1.6}Te₃ thick films by aerosol deposition, *J. Phys.: Conf. Ser.*, **379**, 012011, (2012), doi: 10.1088/1742-6596/379/1/012011.
- ²⁵⁷ Sinha, B.B., Chung, K.C.: Fabrication and properties of MgB₂ coated superconducting tapes, *J. Supercond. Novel Magn.*, **26**, 1507–1511, (2013), doi: 10.1007/s10948-012-1957-7.
- ²⁵⁸ Sinha, B.B., Chung, K.C., Jang, S.H., Park, D.S., Hahn, B.-D.: Fabrication of magnesium diboride thin films by aerosol deposition, *Prog. Supercond.*, **13**, 122–126, (2011).
- ²⁵⁹ Hirose, S., Sakata, H., Nakayama, C., Koshizuka, N., Murakami, M., Akedo, J.: Superconducting MgB₂ thick films by AD process. In: 4th Tsukuba International Coatings Symposium, Frontiers of Coatings Technology: Innovative Processes and Applications, 2010, 17–18.
- ²⁶⁰ Naoe, K., Nishiki, M., Yumoto, A.: Relationship between impact velocity of Al₂O₃ particles and deposition efficiency in aerosol deposition method, *J. Therm. Spray Techn.*, **22**, 1267–1274, (2013), doi: 10.1007/s11666-013-0031-8.
- ²⁶¹ Naoe, K., Sato, K., Nishiki, M.: Effect of process for producing Al₂O₃ particles on deposition efficiency in aerosol deposition method, *J. Ceram. Soc. Jpn.*, **122**, 110–116, (2014), doi: 10.2109/jcersj2.122.110.
- ²⁶² Akedo, J., Nakano, S., Park, J., Baba, S., Ashida, K.: The aerosol deposition method - for production of high performance micro devices with low cost and low energy consumption, *Synthesiology*, **1**, 121–129, (2008).

